Features of strong quark correlations at vanishing and non-vanishing density

Dissertation

zur Erlangung des akademischen Grades
Doktor der Naturwissenschaften (Dr.rer.nat.)

Karl-Franzens Universität Graz

verfasst am Institut für Physik

Andreas Windisch
Betreuer: Prof. Dr. Reinhard Alkofer

August 12, 2014

To my beloved family.

Contents

Chapter 1

Introduction

The Standard Model of particle physics covers three of the four forces driving the fundamental interactions in nature. While it does not treat gravity, it describes the dynamics and interplay of the electromagnetic, the weak and the strong force. The electromagnetic and weak sectors have been unified to form the electroweak sector, whose crucial ingredient, the Higgs-Boson, has been announced [1] only recently. Apart from the electroweak there is the strong sector, which lies in the focus of this thesis.

The strong force acts on scales of the order of fermi ($1\ fm = 1 \times 10^{-15} m$) and binds its fundamental particles to compounds that form the matter we are made of. The quantum field theory describing the strongly interacting sector of the Standard Model of particle physics is Quantum Chromodynamics (QCD)[1]. Its particle content are quarks and gluons, where each flavor of the former is a Dirac spinor field in the fundamental representation, while the latter are vector fields in the adjoint representation of the underlying non-abelian gauge group $SU(N_C)$.

The coupling between quarks and gluons (as well as among the gluons themselves) is not a constant, but varies with the energy scale – one says it 'runs'. The running of the coupling is such that the phenomenon of asymptotic freedom arises, a statement that accounts for the fact that the coupling strength becomes arbitrarily small at large energy scales, that is, at short distances. In this ultraviolet (UV) regime, perturbation theory can be employed, as the coupling is sufficiently small to serve as a parameter suitable for an expansion. At low energies however, the coupling grows strong and a perturbative expansion eventually breaks down. The infrared (IR) regime is thus only accessible through non-perturbative approaches. From a fundamental point of view there is no framework available so far that can be

[1] See [2] for the famous review article by W. Marciano and H. Pagels.

employed to calculate QCD processes without limitations. Lattice calculations [3] are a very successful first principle tool to perform non-perturbative calculations, however, due to the sign problem they are (so far) not capable of probing the dense regime of QCD[2]. Complementary to lattice QCD there are functional methods, which provide an exact[3] non-perturbative framework for QCD formulated in the continuum. In this thesis we employ such techniques. We use Dyson-Schwinger equations (DSEs) [5, 6] to study a central object of QCD – the fully dressed quark-gluon vertex. This vertex is a very important quantity, needed as input for bound-state equations such as Bethe-Salpeter [7] and Faddeev equations [8, 9, 10]. A former study [11] suggests also that, by studying the vertex, one can get insights into two striking features of QCD: the phenomena of confinement, see e.g. [3, 12], and dynamical chiral symmetry breaking [13, 14, 15]. No objects with fractional charge have been detected so far (see e.g. [16, 17, 18, 19]) and also gluons have not been observed [20]. Color charge carrying degrees of freedom are confined to color neutral compounds, which is in agreement with the fact that free quarks are absent from the physical spectrum of QCD. Dynamical chiral symmetry breaking on the other hand is a mechanism that provides a dynamical mass contribution to the quarks. Confinement and dynamical symmetry breaking might be eventually lost in certain regimes of the QCD phase diagram, which is spanned by the μ-T plane, see Figure 1.1 for a sketch.

Even though the sketch might suggest that we have profound knowledge on the actual structure of the phase diagram, we actually know only very little about the real phase structure of QCD. A lot of experimental and theoretical effort is put into studies of the phase diagram. Experiments like the Relativistic Heavy Ion Collider (RHIC), the Large Hadron Collider (LHC) and the Facility for Anti-protons and Ions Research (FAIR) that is currently under construction are accompanied by various theoretical approaches to probe the structure of strongly interacting matter. Relativistic heavy ion collisions, as performed in these impressive experiments, provide insights into the hot and dilute regime of the phase diagram. A laboratory for the intermediately dense and cold regime is the interior of a neutron star. Even though the interior is not directly observable, one can try to learn about the inner structure of the star through observable quantities, such as its mass, radius, temperature and rotation frequency [21, 22].

In this thesis we not only consider aspects of strong quark correlations in the vacuum (that is, at the origin of the phase diagram depicted in Figure

[2]For a modern introduction to lattice QCD see the book of [4] .

[3]However, one has to truncate the system, carefully trying to maintain the parts that are relevant for the physics that is to be described.

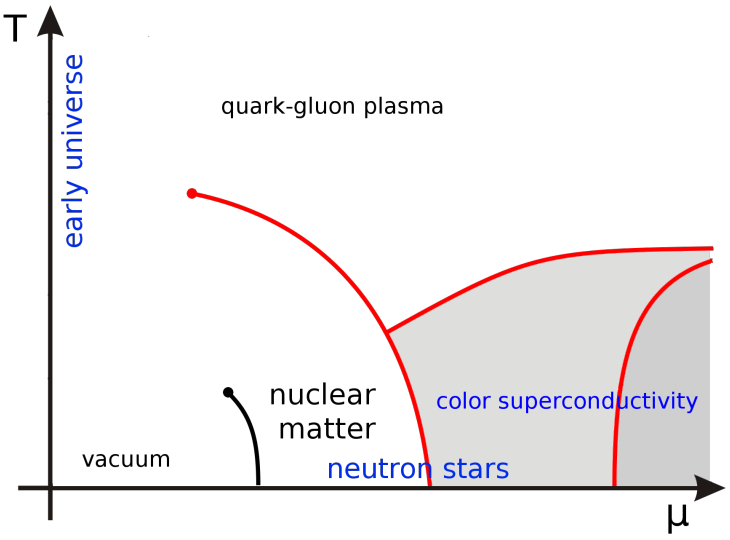

Figure 1.1: A qualitative sketch of the QCD phase diagram that summarizes possible scenarios of states of matter.

1.1), but also in the region that has been labeled as being the regime relevant for neutron star physics. Let me introduce each problem briefly by outlining the structure of this thesis.

In Chapter 2 we introduce basic aspects of QCD. The calculational techniques employed in this work are introduced.

Chapter 3 is dedicated to the calculation of the fully dressed quark-gluon vertex DSE in the Landau gauge, the main topic of this thesis. Due to the considerable complexity of this study, this calculation is also implemented by a fellow PhD student, which introduces a very high level of reliability of our results. At the time of writing this thesis we have established a perfect qualitative agreement of our solutions. We provide a full numerical solution of the eight transverse dressing functions of the vertex, together with the numerical solution of the two dressing functions of the quark propagator DSE we coupled the vertex equation to. The Yang-Mills sector is covered by employing parametrizations [23], as well as DSE results from a separate calculation [24] for the ghost and gluon propagators, and a model for the three-gluon vertex inspired by [25]. Our results are a big improvement of earlier studies, where much more restrictive truncations have been imposed. In a recent study [26], a similar analysis to ours is employed in the context of bound state equations, but without a fully back-coupled vertex[4]. With the

[4]The focus of their study is the role of the vertex in bound state equations, so the vertex solution is needed for complex momenta. A full back-coupling of all tensor structures would

calculation we present here we lay the foundation for future studies on, or based on a fully solved quark-gluon vertex in the Landau gauge. We discuss the importance of the tensor structures of the vertex, which allows for an improved truncation by taking less than 8 tensor structures into account. We also provide a very detailed description of the numerical framework to allow for a relatively easy reproduction of our approach.

Chapter 4 summarizes what we have done to calculate the analytic structure of Green's functions. The ultimate goal is to evaluate the analytic structure of the quark propagator DSE numerically. Even though there are techniques on the market that are capable of obtaining the analytic properties within a parabola-shaped region that slightly extends into the time-like regime [27], we develop and introduce a novel numerical technique that relies on simple deformations of the integration contours and is – in principle – not limited to a subset of complex Euclidean momenta. The calculations are numerically quite demanding, thus a high level of parallelization is required, which we achieve by using graphics processing units (GPUs) and hybrid CPU-GPU clusters. The method is developed by studying a (perturbative) example of Yang-Mills theory that can be solved analytically. We then apply the method to study scalar glueball operators (0^{++}) at the Born level, where the aim is to investigate the positivity properties for different gluon propagator parametrizations. Finally, the extension of our method to non perturbative treatment (such as DSEs) is addressed.

Chapter 5 is the section covering the part of this thesis which is dedicated to the realm of non-vanishing chemical potential. There, we study inhomogeneous color superconducting phases that might be present in the interior of neutron stars. In this scenario we study the Deformed Fermi Surface (DFS) phase and discuss a possible instability of the phase. We furthermore introduce and study the possibility of four-quark condensation in flavor-asymmetric strongly coupled dense matter by investigating a $SU(2)_{spin} \times SU(2)_{flavor}$ toy model in the framework of exact renormalization group equations (ERGEs).

In Chapter 6 we provide a summary and point out future directions motivated by our findings. This chapter is followed by Acknowledgements, as well as by various appendices providing further details of the calculations.

thus complicate their calculation tremendously.

Chapter 2

Theoretical background

In each of the following chapters we will give a short introduction to the particular focus of the respective section. In this Chapter, we summarize the most basic aspects of QCD and point out the relevance of what is being discussed for the studies presented in this thesis.

2.1 Formulation of QCD

2.1.1 The QCD Lagrangian

The Lagrangian of QCD[1] is given by

$$\mathcal{L}_{QCD} = \bar{\psi}\left(-\not{D} + m\right)\psi + \frac{1}{4}F_{\mu\nu}F^{\mu\nu}, \tag{2.1}$$

where the ψ are the quark fields and $F_{\mu\nu}$ is the Yang-Mills field strength tensor given by

$$F^a_{\mu\nu} = \partial_\mu A^a_\nu - \partial_\nu A^a_\mu - g f^{abc} A^b_\mu A^c_\nu, \tag{2.2}$$

where f^{abc} are the structure constants of the gauge group and A^a_μ are the gauge fields[2]. The spin-$\frac{1}{2}$ fermion fields ψ transform under the fundamental representation of the gauge group $SU(N_C)$, the gauge fields A^a_μ transform

[1] In this thesis we work solely in Euclidean space, see Appendix A for definitions and conventions.

[2] In Section 4 we investigate certain properties of a correlator constructed of two squares of this field-strength tensor. This object is composed of gauge-fields only and corresponds to a scalar glueball.

under the adjoint representation. Even though in the QCD case the number of colors N_C is three[3], we will keep it as a free parameter and introduce a particular value when necessary. For the $N_C = 3$ case, the quarks come in three colors, and there are $3^2 - 1 = 8$ gluons. The covariant derivative D is given by

$$D_\mu \;=\; \partial_\mu + igA_\mu, \tag{2.3}$$

with

$$A_\mu = A_\mu^a t^a, \tag{2.4}$$

and where the generators t^a satisfy

$$\left[t^a, t^b\right] = if^{abc}t^c. \tag{2.5}$$

In (2.1) and throughout this thesis we also use the Feynman slash notation, defined through

$$\not{D} \;\equiv\; \gamma_\mu D^\mu, \tag{2.6}$$

where the Euclidean Gamma matrices γ^μ are given in Appendix A. The covariant derivative establishes a link between the fermion fields to the gauge fields via the coupling g.

2.1.2 The generating functional of QCD

One can define a generating functional by employing the Euclidean path-integral formulation,

$$\begin{aligned} &Z\left[\eta, \bar{\eta}, j\right] = \\ &\int \mathcal{D}\left[\psi\bar{\psi}A\right] \exp\left\{-S_{QCD}\left[\psi, \bar{\psi}, A\right] + \int d^4x \left(A_\mu^a j_\mu^a + \bar{\eta}\psi + \bar{\psi}\eta\right)\right\}, \end{aligned} \tag{2.7}$$

where the QCD action follows from the integral over the Lagrangian density (2.1) ,

$$S_{QCD}\left[\psi, \bar{\psi}, A\right] = \int d^4x \left\{\mathcal{L}_{QCD}\right\}, \tag{2.8}$$

[3]Evidence for $N_C = 3$ in QCD is discussed in detail in [2].

and where we have introduced Grassmann valued sources η and $\bar{\eta}$ for the fermion fields $\bar{\psi}$ and ψ, as well as a source j_μ^a for the gauge fields A_μ^a. By performing functional derivatives with respect to the sources, one can derive correlation functions of the theory.

2.1.3 Fixing the gauge

The necessity of gauge fixing arises due to the invariance of the action under local transformations $U(x)$, $S[A] = S\left[A^U\right]$, where

$$A_\mu^U(x) = U(x) A_\mu(x) U^\dagger(x) + \frac{i}{g} (\partial_\mu U(x)) U^\dagger(x), \tag{2.9}$$

and

$$U(x) = e^{ig\Theta_a t_a}. \tag{2.10}$$

The integration over all gauge configurations in the path integral overcounts gauge-equivalent configurations belonging to the same gauge orbit. Only one representative per gauge orbit should be taken into account, thus one has to find a way to implement this requirement. On the level of the generating functional, one can perform the procedure proposed by Faddeev and Popov [28], which gives rise to a modified generating functional,

$$\begin{aligned} &Z[\eta, \bar{\eta}, j, \sigma, \bar{\sigma}] = \\ &\int \mathcal{D}\left[\psi\bar{\psi}Ac\bar{c}\right] \exp\left\{-S_{QCD}\left[\psi, \bar{\psi}, A\right] + \int d^4x \left(A_\mu^a j_\mu^a + \bar{\eta}\psi + \bar{\psi}\eta\right)\right\} \\ &\times \exp\left\{\int d^4x \left(\bar{\sigma}c + \bar{c}\sigma\right) - \int d^4x \left(\left(\frac{\partial_\mu A_\mu}{2\zeta}\right)^2 - i\partial_\mu \bar{c} D_\mu c\right)\right\}, \end{aligned} \tag{2.11}$$

where the fields c and $\bar{c}$ are the Grassmanian ghost fields, D_μ is the covariant derivative and ζ is a gauge parameter. In this thesis we study Green's functions in the Landau gauge, which corresponds to a choice of $\zeta = 0$ and implies $\partial_\mu A_\mu = 0$. This gauge is particularly convenient, as it is a fixed point with respect to renormalization, and it is a preferred gauge for Dyson-Schwinger studies. Note that the Faddeev-Popov procedure still does not completely isolate one representative per gauge orbit–there are still gauge-equivalent configurations left, the Gribov copies [29]. Formally, one can view the Faddeev-Popov procedure as introducing a hyper-plane in the space of gauge field configurations. The representatives chosen by the procedure are

the intersections of the gauge orbits with this hyper-plane. As a gauge orbit might intersect the plane more than once, an over-counting arises. Further restrictions have to be imposed in order to minimize the number of copies. see e.g. [30, 31, 32] for a discussion.

2.1.4 Renormalization and regularization

Renormalization is a very important concept in quantum field theory. Loop integrals in a quantum field theory can possess ultra violet (UV) divergences when the cut-off of the loop momentum is taken to infinity. Physically, such divergent loop integrals correspond to field-fluctuations which grow large on short scales, eventually giving rise to ill-defined quantities in the corresponding quantum field theoretical description. In order to render such a theory meaningful one has to employ a renormalization scheme. In a renormalizable theory this can be achieved by absorbing the divergences into the (unphysical) bare parameters of the theory see e.g. the book of [33]. For a recent study on how one can use Hopf-algebras to gain insights into the mechanisms of renormalization see e.g. [34].

With the renormalized Becchi, Rouet, Stora and Tyutin (BRST) algebra [35, 36] of the gauge fixed theory [37] we can proceed by considering the renormalization procedure for our Lagrangian. We introduce renormalization constants as follows,

$$\begin{aligned} &\mathcal{L}_q = \\ &Z_2\bar{\psi}\left(-\not{\partial}_\mu + Z_m m_b\right)\psi - i\ g\ Z_{1F}\left(\bar{\psi}\gamma_\mu t^a \psi A^a_\mu\right), \end{aligned} \tag{2.12}$$

where we restrict our consideration to the quark sector for simplicity. Similarly one has to introduce further renormalization constants for the Yang-Mills sector. As far as the quarks are concerned, we introduced the quark-wave function renormalization constant Z_2, a renormalization constant to shift the bare mass m_b to its physical value, as well as a renormalization constant Z_{1F} for the quark-gluon vertex. In our study of the quark gluon vertex we also have to deal with the Yang-Mills sector, so in addition we have the renormalization constants Z_1, $\tilde{Z}_1$ and $\tilde{Z}_3$ in our truncation. In Landau gauge one can employ $\tilde{Z}_1 = 1$ [38], and we are left with the ghost renormalization constant and the renormalization constant for the ghost-gluon vertex. Using Slavnov-Taylor identities [38, 39] one can establish a relation between the renormalization constants. In our calculation of the quark-gluon vertex we will make use of that by employing

$$Z_{1F} = \frac{Z_2}{\tilde{Z}_3}, \tag{2.13}$$

where the renormalization of the Yang-Mills system has to be such that the overall procedure of renormalization imposed on the system is consistent. In the study of the F^2 correlator in Chapter 4 we will also have to deal with divergent loop integrals. There, however, we will regularize the expressions using the Bogoliubov-Parasiuk-Hepp-Zimmermann (BPHZ) prescription [40, 41, 42].

2.2 Positivity and confinement

In Chapter 4 we study correlators constructed from purely gluonic degrees of freedom. One important ingredient for this study is the observation that we use colored objects to form the correlator of squares of the Yang-Mills field strength tensor. The correlator itself is then a color-neutral object, meaning that the transition from absence of the ingredients to presence of the result in the space of asymptotic states has to be manifest in our calculation somehow. There are different scenarios of how confinement could be realized in a quantum field theoretical framework[4]. One possibility to tell whether a certain degree of freedom is absent from the space of asymptotic states is to look for positivity violations that might spoil a probabilistic interpretation through negative norm contributions[5]. Correlators with negative norm contribution do not possess a Källén-Lehmann spectral representation [48, 49] and are absent from the space of asymptotic states. In this sense, one can consider them as being 'confined'. Positivity violations of the gluons are evident from lattice studies [50, 51] and from functional studies [52, 53, 54]. For a two-point function $\Delta(p^2)$ of a spin-zero operator Φ we may write a spectral representation,

$$\Delta(p^2) = \int \frac{d^d p}{(2\pi)^d} e^{i\,p\cdot x} \langle \Phi(x)\Phi(0)\rangle = \int_{\tau_0}^{\infty} d\tau \frac{\rho(\tau)}{\tau + z}, \tag{2.14}$$

with τ_0 the lowest energy that is possible for a state. The spectral density $\rho(p^2)$ is related to the discontinuity of a branch cut,

$$\rho(p^2) = \frac{1}{2\,\pi\,i} \lim_{\epsilon\to 0^+} [\Delta(-p^2 - i\,\epsilon) - \Delta(-p^2 + i\,\epsilon)], \tag{2.15}$$

[4]For summaries see e.g. [43, 44].

[5]In Minkowski space an axiomatic formulation of quantum field theory is provided by the Wightman axioms [45]. For a Euclidean field theory, an axiomatic system analogous to the Minkowski formulation has been defined [46, 47].

with $-p^2 > \tau_0$. Thus one can look for positivity violations of the spectral function by extracting the discontinuity of the branch cut.

2.3 Functional methods

2.3.1 Dyson-Schwinger equations (DSEs)

Dyson-Schwinger equations [5, 6, 55] are the equations of motion of the Green's functions of a theory, see [56, 57, 58, 59] for reviews. They provide an infinite tower of coupled equations for the n-point functions of the theory. They are not limited to the weakly coupled regime, but can be employed to study non-perturbative phenomena such as confinement and dynamical chiral symmetry breaking. One big advantage as compared to lattice methods is, that, as DSEs are formulated in the continuum, all scales are in principle accessible. DSEs do not suffer from a sign problem, and also the chiral limit can be studied easily. While the equations are exact once they have been derived, one has to impose careful truncations on the system in order to solve the equations.

DSEs follow from the observation that, with appropriate boundary conditions, an integral over a derivative vanishes,

$$\begin{aligned} 0 &= \int \mathcal{D}[\phi] \frac{\delta}{\delta\phi} e^{-S+\int dx \phi(x) J(x)} \\ &= \left(\frac{\delta S}{\delta\phi}\left[\frac{\delta}{\delta J}\right] + J \right) Z[J] \,. \end{aligned} \tag{2.16}$$

Differentiating this equation repeatedly with respect to the sources J, one obtains an (infinite) set of recurrence relation between the n-point functions. These are the Dyson-Schwinger equations, see [60, 61] for text books presenting the derivation.[6] Let us discuss the necessity of truncating a DSE system by considering the Yang-Mills system in the Landau gauge. The untruncated DSEs for the Yang-Mills propagators, together with the DSE for the quark propagator are depicted in Figure 2.1.

The system has to be truncated, that is, certain contributions are neglected. In Figure 2.2 we show the truncated version of the system, where we labeled the steps of the truncation with numbers. The quark-loop contribution in the box labeled with '1' corresponds to a quenched approximation.

[6] The derivation of DSEs can be quite technical, thus there are Mathematica packages available that can perform DSE derivations [62] and even DSE and ERGE derivations [63] automatically. Also a framework for solving DSEs is available [64].

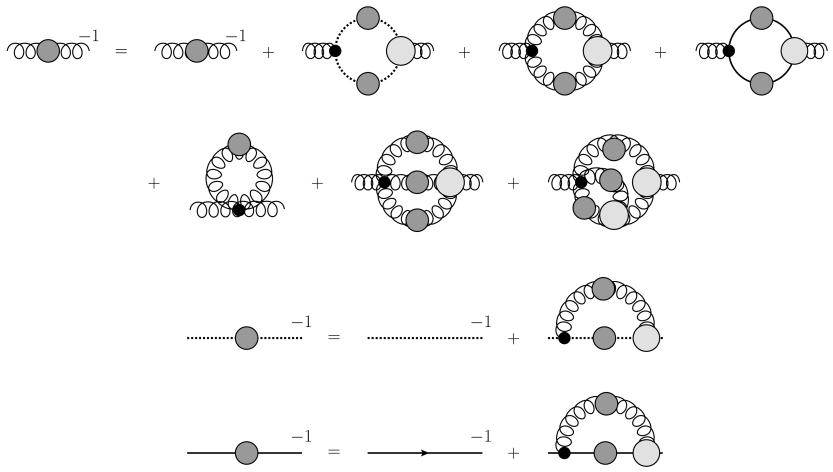

Figure 2.1: The DSEs of the Yang-Mills propagators, together with the DSE for the quark propagator in Landau gauge. Wiggly lines correspond to gluons, dotted lines to ghosts and solid lines to quarks.

The matter sector does not couple back onto the Yang-Mills sector, thus we have also drawn a line between the two realms in Figure 2.2. The contribution in box number 2, the tadpole, can be neglected as it only amounts for an overall constant that can be removed by normalization. The last box, labeled as '3', are the two-loop terms, the sunset and the squint diagram. As far as the infrared physics is concerned, these diagrams are sub-leading in the Landau gauge and are also neglected. In our study of the quark-gluon vertex we employ parametrizations of solutions of the Yang-Mills sector that has been truncated in this fashion, where also an ansatz for the three-gluon vertex has been employed.

The main subject of this thesis is a study of the coupled equations of the quark-gluon vertex and the quark propagator Dyson-Schwinger equations. As a starting point we take the study of [11]. There, the authors also studied the quark-gluon vertex in quenched QCD in the Landau gauge. For the quark-gluon vertex, there are two versions of the DSE, see Figures 2.3 and 2.4.

Without truncations, these two equations are equivalent. In our study of the quark-gluon vertex we proceed in the same way as the authors in [11] by employing a truncation for the quark-gluon vertex that resembles the second versions of the DSE depicted in Figure 2.4, where all vertices are dressed and where the last diagram is omitted. Such a truncation can be derived

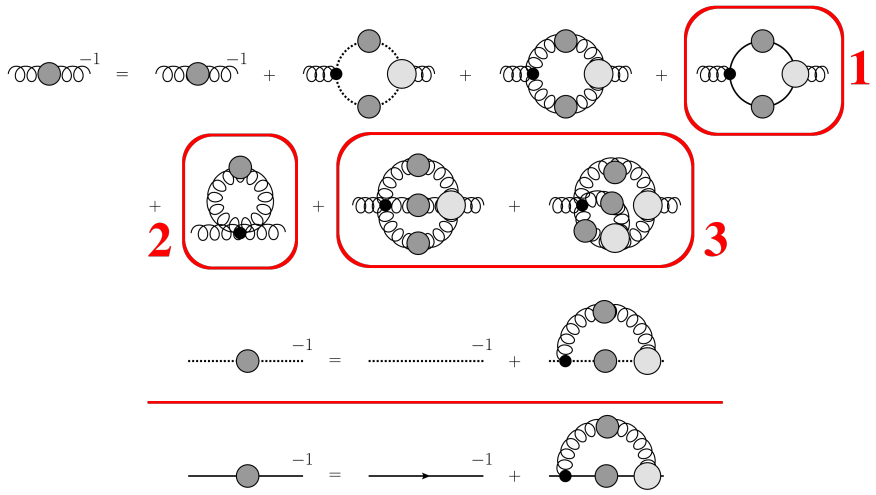

Figure 2.2: A truncation for the gluon propagator DSE, see text.

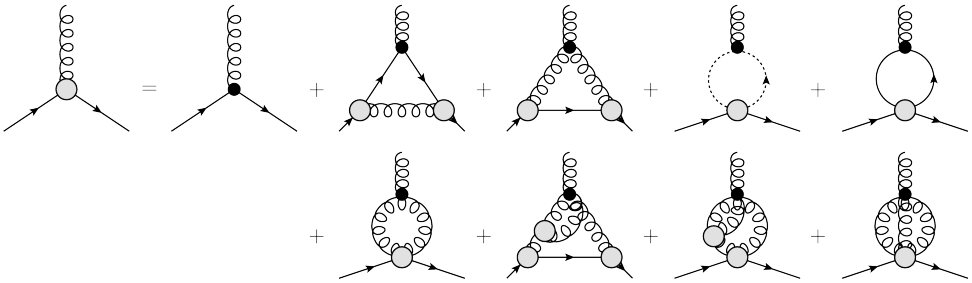

Figure 2.3: The DSE for the quark-gluon vertex.

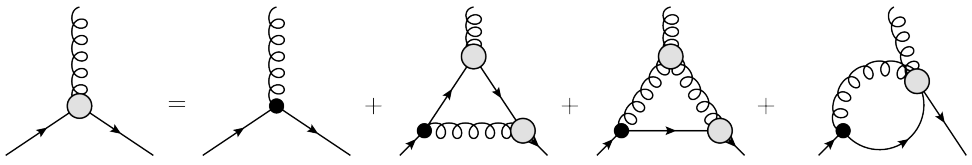

Figure 2.4: The vertex DSE can also be written like this, where the external gluon is coupled to a bare vertex.

from a 3PI effective action [65]. Note that a similar truncation scheme has also been employed in a very recent study on the quark-gluon vertex [26]. However, the great improvement of our study is that no fully back-coupled vertex equation has been considered so far. In this thesis we provide the first full solution of the vertex with all tensor structures taken into account.

2.3.2 Exact renormalization group equations (ERGEs)

Closely related to the functional integral equations of the DSE framework are the exact renormalization group equations (ERGEs) [66], for reviews see e.g. [67, 68]. They are functional differential equations and express the change of the effective average action under variation of a regulator scale k. One starts at an ultraviolet scale with the UV action S and can smoothly run down to the quantum effective action in the infrared. In this sense, the frameworks acts like a microscope, the scale being the magnification that is driven from microscopic towards macroscopic scales. Consider the (scale dependent) functional for connected Green's functions,

$$W_k[J] = \ln \int \mathcal{D}[\chi] \exp\left\{-S[\chi] - \Delta S_k[\chi] + \int d^4x J\chi\right\}, \tag{2.17}$$

where J are the sources and χ is a field. Hereby we have introduced a modification as compared to the usual functional. We have implemented an additional term $\Delta S_k[\chi]$ that acts as an IR cut-off,

$$\Delta S_k[\chi] = \frac{1}{2}\int \frac{d^4q}{(2\pi)^4}\, \chi(-q)\, R_k(q)\, \chi(q). \tag{2.18}$$

The function $R_k(q)$ has to satisfy certain constraints. For a fixed q, it has to vanish when k tends to zero, while it should go to infinity as k goes to infinity (or to the UV cutoff scale). This ensures that the regulator vanishes as k is taken to zero, giving rise to the full effective action. The second requirement ensures that we obtain the initial action when the scale is taken to infinity. As the regulator is quadratic in the fields, Fourier modes of χ with $q < k$ acquire a mass contribution. Contrary, for $q \gg k$, the suppression of the regulator leaves the theory unchanged. It is thus evident that it serves indeed as an infrared regulator. There are various choices of regulator functions available, we will however employ an optimized regulator, see [69, 70].

Going back to the functional (2.17) we can perform a Legendre transform to obtain the average action $\Gamma_k[\Xi]$,

$$\Gamma_k[\Xi] = -\Delta S_k[\Xi] - W_k[J] + \int d^4q \; J\Xi, \tag{2.19}$$

where Ξ is the expectation value of χ,

$$\Xi = \langle\chi\rangle = \frac{\delta W_k[J]}{\delta J}. \tag{2.20}$$

Now we want to derive the flow equation. To this end it is helpful to define

$$\tilde{\Gamma}_k[\Xi] = \Gamma_k[\Xi] + \Delta S_k[\Xi]. \tag{2.21}$$

Plugging this into equation (2.19) we obtain

$$\tilde{\Gamma}_k[\Xi] = -W_k[J] + \int d^4q \; J\Xi. \tag{2.22}$$

Performing a derivative with respect to k on the last expression, we find

$$\begin{aligned} &\frac{\partial}{\partial k}\tilde{\Gamma}_k[\Xi] = \\ &-\frac{\partial W_k}{\partial k}[J] - \int d^4q \; \underbrace{\left(\frac{\delta W_k}{\delta J}\right)}_{\overset{(2.20)}{=}\Xi} \left(\frac{\partial J}{\partial k}\right) + \int d^4q \Xi \frac{\partial J}{\partial k} \\ = \; &-\frac{\partial W_k}{\partial k}[J]. \end{aligned} \tag{2.23}$$

We can compute the derivative of W_k by looking at its definition in equation (2.17). As we perform the derivative with respect to the scale k, we expect only a contribution from the regulator term we introduced above. Thus we are left with

$$\begin{aligned} \frac{\partial}{\partial k}\tilde{\Gamma}_k[\Xi] &= \langle\frac{\partial}{\partial_k}\Delta S_k[\Xi]\rangle \\ &\overset{(2.18)}{=} \langle\frac{1}{2}\int d^4p \int d^4q \; \chi(q) \frac{\partial}{\partial k} R_k(q,p) \chi(p)\rangle, \end{aligned} \tag{2.24}$$

and $R_k(p,q) = R_k(q)\,\delta(p-q)$. From the functional for connected Green's functions we can derive a two-point function by performing two functional derivatives with respect to the sources,

$$G_k(q,p) = \frac{\delta W_k}{\delta J(q)\,\delta J(p)}, \tag{2.25}$$

which can be decomposed according to

$$\begin{aligned}\langle \Xi(q)\,\Xi(p)\rangle &= G(q,p) + \langle\chi(q)\rangle\langle\chi(p)\rangle \\ &\overset{(2.20)}{=} G(q,p) + \Xi(q)\,\Xi(p)\,.\end{aligned} \tag{2.26}$$

This expression can now be used to introduce the two-point function in equation (2.24),

$$\begin{aligned}\frac{\partial}{\partial_k}\tilde{\Gamma}_k[\Xi] &= \langle\frac{1}{2}\int d^4p\int d^4q\;\chi(q)\,\frac{\partial}{\partial k}R_k(q,p)\,\chi(p)\rangle \\ &= \frac{1}{2}\int d^4p\int d^4q\left[\frac{\partial}{\partial k}R_k(q,p)\,G(q,p) + \Xi(q)\,\frac{\partial}{\partial k}R_k(q,p)\,\Xi(p)\right] \\ &= \frac{1}{2}\mathrm{Tr}\left[G\frac{\partial}{\partial k}R_k\right] + \frac{\partial}{\partial k}\Delta S_k[\Xi]\,.\end{aligned} \tag{2.27}$$

Now we can use the definition (2.21), as well as the fact that the Green's function G is the inverse of $\left[\Gamma_k^{(2)}[\Xi] + R_k\right]$, to write down the Wetterich equation [66],

$$\frac{\partial}{\partial k}\Gamma_k[\Xi] = \frac{1}{2}\mathrm{Tr}\left\{\left(\Gamma_k^{(2)}[\Xi] + R_k\right)^{-1}\frac{\partial}{\partial k}R_k\right\}. \tag{2.28}$$

In Chapter 5 we will use this equation to study the possibility of four-fermion condensation in strongly interacting asymmetric matter.

2.4 Bosonization

In Chapter 5 we have to bosonize a theory that features an eight-fermion interaction term. To this end we use a Hubbard-Stratonovich transformation [71, 72]. Here we introduce the procedure by discussing a simple example. Consider some Lagrangian density $\mathscr{L}$ with a four-fermion interaction,

$$\mathscr{L} \;=\; \bar{\psi}\left(i\not{\partial} - m_0\right)\psi - g_2\left(\bar{\psi}\psi\right)^2, \tag{2.29}$$

such that the path integral reads

$$Z \;=\; \int \mathscr{D}\left[\bar{\psi}\right]\mathscr{D}\left[\psi\right]\exp\left\{-\int d^4x\mathscr{L}\right\}. \tag{2.30}$$

The idea behind the Hubbard-Stratonovich transformation is to use the observation that a bilinear appearing in the exponential function can be interpreted as being the result of a Gaussian integral, i.e. for a one-dimensional non-functional integral the relation

$$\sqrt{\frac{2\pi}{m^2}}\exp\left\{\frac{g^2b^2}{2m^2}\right\} \;=\; \int_{-\infty}^{\infty} dx\exp\left\{-\frac{m^2}{2}x^2 - gbx\right\} \tag{2.31}$$

holds. Applying this observation to the more general case of functional integrals we can remove the quartic term from the Lagrangian by introducing a new scalar field φ with mass m_φ, together with a Yukawa coupling g_2^Y. The couplings are related by

$$\frac{\left(g_2^Y\right)^2}{2m_\varphi^2} \;\stackrel{!}{=}\; g_2. \tag{2.32}$$

Applying this to the example above, we find

$$\begin{aligned} &\exp\left\{\int dx\; g_2\left(\bar{\psi}\psi\right)^2\right\} \\ \propto\;& \int \mathscr{D}\left[\varphi\right]\exp\left\{-\int dx\left(m_\varphi^2\varphi^2 + g_2^Y\varphi\bar{\psi}\psi\right)\right\}, \end{aligned} \tag{2.33}$$

where the proportional-symbol indicates that the constant factor has been dropped[7].

After the Hubbard-Stratonovich transformation we are left with

$$\begin{aligned} Z \;=\; &\int \mathscr{D}\left[\bar{\psi}\right]\mathscr{D}\left[\psi\right]\mathscr{D}\left[\varphi\right]\exp\left\{-\int d^4x\mathscr{L}_{free}\right\} \\ &\times\exp\left\{-\int dx\left(\frac{m_\varphi^2}{2}\varphi^2 + g_2^Y\varphi\bar{\psi}\psi\right)\right\}. \end{aligned} \tag{2.34}$$

[7]Due to the normalization of physical correlators, this constant can be neglected.

In Chapter 5 we have to apply this procedure once to bosonoize the eight-fermion interaction, and two further times to bosonize the resulting terms containing four fermions each. Further details on that particular case are given in Chapter 5 and in Appendix I.

Chapter 3

The fully dressed quark-gluon vertex in the Landau gauge

3.1 Introduction

In this Chapter we present our study of the dressed quark-gluon vertex, an object that has been in the focus of many studies in the past, see e.g. [73, 74, 11, 75, 76, 26]. One motivation behind this study is to gain deeper insights into a possible relation between dynamical chiral symmetry breaking and confinement that might be manifest in the solutions to the vertex [11]. Another reason for this study is to obtain solutions to improve model building and to provide a minimum of tensor structures that have to be taken into account to capture the relevant physics[1], which is important for studies that need the quark-gluon vertex as an input. Furthermore, in studies of QCD with a large number of fundamentally charged quark flavors, the quark-gluon vertex has been identified to have an impact on the critical number of fermion flavors above which the coupling forms a plateau [77, 78], which also requires detailed knowledge of this Green's function. We work in Landau gauge, using Dyson-Schwinger equations to perform the calculation in the strongly coupled regime. The vertex is solved together with the Dyson-Schwinger equation of the quark propagator, so we seek solutions for two dressing functions depending on one variable for the propagator and eight dressing functions depending on three Lorentz invariants for the eight transverse structures of the quark-gluon vertex. The progress of this project has been reported in conference proceedings [79, 80], a paper with our results is in preparation. The calculation presented in this thesis is also implemented by a fellow PhD student [81]. This is necessary, as the computation itself is

[1] This is related to the question of finding a suitable basis to span the vertex.

quite involved, so a high level of reliability of our results is achieved by comparing the results of the two independent implementations. For a discussion of the first comparison of our results, see Section 3.5.4 below. Further details of this study will become available in [81], here we present some first qualitative results. This chapter is organized as follows. In Section 3.2 we introduce our truncation scheme. Different possibilities of basis systems are discussed in Section 3.3, renormalization and a step-by-step guide of how to solve the system are presented in Sections 3.4 and 3.5 respectively. Finally we present our results in Section 3.6 and conclude. An alternative approach of how to solve the coupled system of the quark-propagator and the quark-gluon vertex DSE is presented in Appendix C.

3.2 The truncation scheme

3.2.1 The Yang-Mills sector

For the Yang-Mills propagators we used parametrizations [23], as well as a discrete data set that has been obtained from a separate DSE calculation provided by [24]. The discrete data set has been extended to an arbitrary momentum range by matching the data set to an IR and UV solution, for the intermediate regime we used cubic spline interpolation. The power laws for the gluon and ghost dressings in the infrared are given by

$$Z(x) \sim x^{2\kappa}, \tag{3.1}$$
$$G(x) \sim x^{-\kappa}, \tag{3.2}$$

with $\kappa = \frac{93-\sqrt{1202}}{98}$. In order to get the renormalization procedure for the whole system consistent, one has to be careful to adjust the renormalization procedure according to the Yang-Mills input.

Furthermore, we need the three-gluon vertex as an input, see [25, 82, 83, 84, 85, 86, 87] for some recent studies. Here we are interested in obtaining qualitative information on how important different tensor structures in the quark-gluon vertex are. The actual model for the three-gluon vertex has an impact on any quantitative prediction, but it does not alter the overall picture of important tensor structures. For the results shown in this Chapter we thus employed a model for the three gluon vertex where the tree-level structure is multiplied by a function h which is given by[2]

[2]See [25] for details .

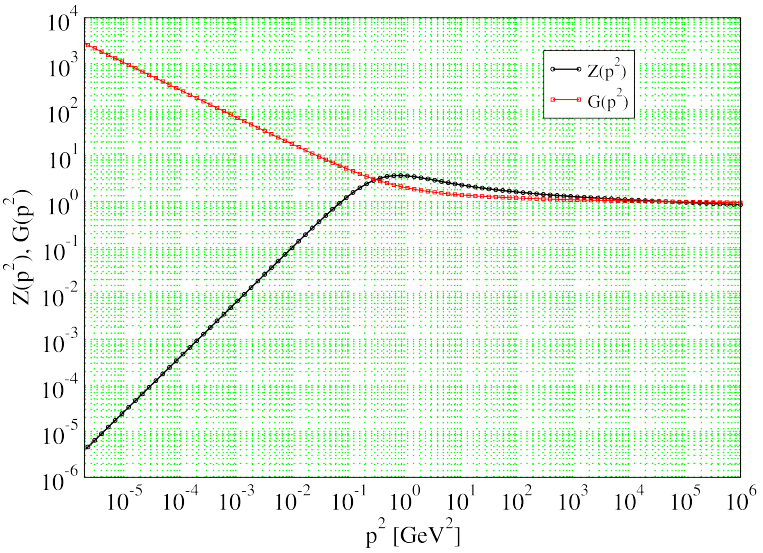

Figure 3.1: Gluon and ghost dressing functions are needed as input.

$$h\left(x,y,z\right) \;=\; \frac{h_1}{Z_1} Z\left(\frac{x+y+z}{2}\right)^{-1-3\delta} G\left(\frac{x+y+z}{2}\right)^{-2-6\delta}, \qquad (3.3)$$

where we used $Z_1 = 1.01$, $\delta = -\frac{9}{44}$ and where h_1 is a constant that can be adjusted to increase or reduce the strength provided by the three-gluon vertex. The Yang-Mills sector also provides the renormalization constant $\tilde{Z}_3$ which is needed to determine the renormalization constant Z_{1F} below.

3.2.2 The truncated equations

The system of equations we treat throughout this chapter is shown in Figures 3.2 and 3.3. In our truncation, the quark-gluon vertex equation results from a 3PI effective action [65]. This truncation scheme has already been considered and studied in [11], where the connection to the DSE for the quark-gluon vertex is discussed in more detail (see also Chapter 2 for some remarks on the truncation).

Apart from the tree-level structure there are two diagrams contributing to the vertex equation, the 'abelian' and the 'non-abelian' diagram[3]. Note that, contrary to a Dyson-Schwinger equation derived from a 1PI functional, all vertices are dressed in this self-consistent integral equation. As a last

[3]The latter is called non-abelian because it contains a purely gluonic interaction vertex.

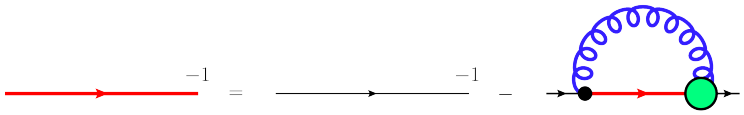

Figure 3.2: The propagator Dyson-Schwinger equation.

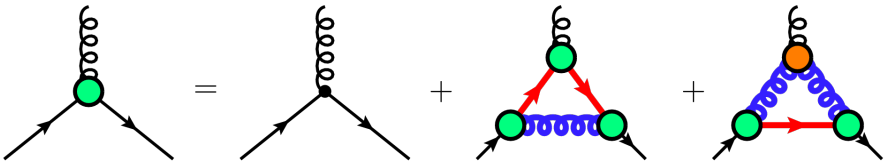

Figure 3.3: The vertex equation in a 3PI formulation.

step in truncating the system we neglect the abelian diagram. On the one hand, a leading order skeleton expansion shows that the abelian diagram is suppressed dynamically. On the other hand, the color factors of the diagrams are such that the abelian diagram is suppressed by a factor of N_C^2 as compared to the non-abelian diagram. This leaves us finally with the truncated system we are about to solve, see Figure 3.4.

The truncated system is then given by the propagator equation shown in Figure 3.2, together with the truncated vertex equation in a 3PI formulation as shown in Figure 3.4.

Algebraically, the truncated propagator equation is given by

$$\begin{aligned} S(p)^{-1} &= Z_2 S_0^{-1}(p) \\ &\quad - Z_{1F} g^2 C_P \int \frac{d^4q}{(2\pi)^4} \gamma^\nu S(q) \Gamma^\mu(p,q;p\cdot q) D^{\mu\nu}(p-q), \end{aligned} \tag{3.4}$$

where $C_P = \frac{N_C^2-1}{2N_C}$. The vertex is expanded in a certain basis, see Section 3.3 below. The vertex equation reads

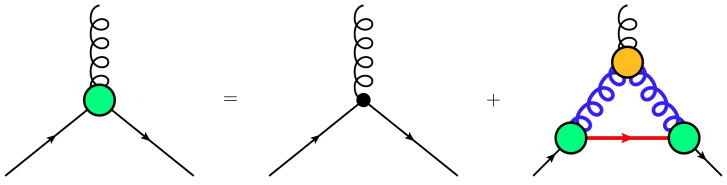

Figure 3.4: Our truncation for the vertex equation.

$$\Gamma^{\mu}(p,q;p\cdot q) = Z_{1F}\gamma^{\mu} + g^2 C_V \int \frac{d^4w}{(2\pi)^4}\Gamma^{\rho}(w,q;w\cdot q)\,S(w) \tag{3.5}$$
$$\times\Gamma^{\nu}(p,w;p\cdot w)\,D^{\nu\nu'}(p-w)\,\Gamma^{\nu'\rho'\mu}(p,q,w,)\,D^{\rho\rho'}(w-q)\,,$$

with $C_V = \frac{iN_C}{2}$ (see Section B.1.3). The coupling at the renormalization point is introduced via the relation

$$\alpha(s) = \frac{g^2}{4\pi}. \tag{3.6}$$

3.3 Choosing a basis

Throughout the calculation we use two different basis sets for the quark-gluon vertex. One set is constructed such that it is orthonormal. This basis set will be referred to as being the 'outer basis', as we will use it to update the quark-gluon vertex dressing functions in each iteration. Internally, a second basis set is employed. This set is not orthonormal and is used for every vertex on the right hand side of the self-consistency equations. We call this basis the 'inner basis'. Both basis sets consist of eight transverse tensor structures. In principle one could use the same basis for the outer and the inner vertices, but this affects the number of terms in the integration kernels. The here employed basis sets turned out to be a good choice for this study.

3.3.1 The outer basis of the vertex

The outer basis set is orthonormal and transverse with respect to the momentum of the gluon. It is constructed from the following elements,

$$\left\{ \begin{array}{c} \frac{1}{\sqrt{2}}\gamma^{\mu}_{TT} \\ s^{\mu} \\ d^{\mu} \end{array} \right\} \otimes \left\{ \begin{array}{c} \mathbb{1} \\ \not{s} \\ \not{d} \\ \not{s}\not{d} \end{array} \right\}, \tag{3.7}$$

where the subscript TT stands for double-transverse (see below for an explanation). The corresponding basis elements are summarized in Table 3.1.

The momentum $d^{\mu}$is the normalized gluon momentum,

$$d^{\mu} = \frac{\Delta^{\mu}}{||\Delta^{\mu}||}, \tag{3.8}$$

$\tau_1^\mu = \frac{1}{\sqrt{2}}\gamma_{TT}^\mu$	$\tau_5^\mu = \frac{i}{\sqrt{2}}\not{s}\gamma_{TT}^\mu$
$\tau_2^\mu = i\ s^\mu \mathbb{1}$	$\tau_6^\mu = \not{s}s^\mu$
$\tau_3^\mu = \frac{i}{\sqrt{2}}\not{d}\gamma_{TT}^\mu$	$\tau_7^\mu = \frac{1}{\sqrt{2}}\not{s}\not{d}\gamma_{TT}^\mu$
$\tau_4^\mu = \not{d}s^\mu$	$\tau_8^\mu = i\ \not{s}\not{d}s^\mu$

Table 3.1: The orthonormal basis of the quark gluon vertex, inspired by [88].

with $\Delta^\mu = p^\mu - q^\mu$ the gluon momentum. The momentum s^μ is then given by normalizing the $\Delta-$transverse part of the average quark momentum $\Omega^\mu = \frac{1}{2}(p^\mu + q^\mu)$,

$$\begin{aligned} s^\mu &= \frac{(\delta^{\mu\nu} - d^\mu d^\nu)\,\Omega^\nu}{||\,(\delta^{\mu\nu} - d^\mu d^\nu)\,\Omega^\nu||} \\ &= \frac{\Omega^\mu - d^\mu d\cdot\Omega}{||\Omega^\mu - d^\mu d\cdot\Omega||}. \end{aligned} \tag{3.9}$$

The subscript TT in γ_{TT}^μ is to indicate that this element is transverse to both, the normalized gluon momentum d^μ and the normalized average quark momentum s^μ, that is,

$$\begin{aligned} \gamma_T^\mu &:= (\delta^{\mu\nu} - d^\mu d^\nu)\,\gamma^\nu \\ &= \gamma^\mu - d^\mu \not{d}, \end{aligned} \tag{3.10}$$

and

$$\begin{aligned} \gamma_{TT}^\mu &= (\delta^{\mu\nu} - s^\mu s^\nu)\,\gamma_T^\nu \\ &= \gamma_T^\mu - s^\mu\,(s.\gamma_T) \\ &= \gamma^\mu - d^\mu \not{d} - s^\mu \not{s}. \end{aligned} \tag{3.11}$$

The relation of orthonormality is then given by

$$\frac{1}{4}\mathrm{Tr}_D\left\{\bar{\tau}_i^\mu, \tau_j^\mu\right\} = \delta_{ij}, \tag{3.12}$$

where the bar indicates hermitean conjugation. The conjugate elements are thus the same as the elements shown in Table 3.1, except that the elements number 2 and 7 acquire an additional minus sign.

3.3.2 The inner basis of the vertex

The inner basis is employed for every quark-gluon vertex that appears internally within another diagram, that is, in the quark self-energy and within the

non-abelian diagram in our truncation. There is no reason to demand that the inner basis fulfills an orthonormality relation. However, as we are interested in the transverse structure we take the same basis elements as before but do not normalize them, nor do we make them transverse to the average quark momentum. The elements of the internal basis are combinations of

$$\left\{ \begin{array}{c} \gamma_T^\mu \\ s^\mu \\ d^\mu \end{array} \right\} \otimes \left\{ \begin{array}{c} \mathbb{1} \\ \not{s} \\ \not{d} \\ \not{s}\not{d} \end{array} \right\}. \tag{3.13}$$

The elements of this basis are summarized in Table 3.2.

$\rho_1^\mu = \gamma_T^\mu$	$\rho_5^\mu = i\not{s}\gamma_T^\mu$
$\rho_2^\mu = i\ s^\mu \mathbb{1}$	$\rho_6^\mu = \not{s}s^\mu$
$\rho_3^\mu = i\not{d}\gamma_T^\mu$	$\rho_7^\mu = \not{s}\not{d}\gamma_T^\mu$
$\rho_4^\mu = \not{d}s^\mu$	$\rho_8^\mu = i\ \not{s}\not{d}s^\mu$

Table 3.2: The inner basis of the quark gluon vertex.

As before, γ_T^μ is given by equation (3.10).

3.3.3 Change of basis

The basis systems are

$$\Gamma^\mu(p,q;p\cdot q) = \sum_{i=1}^{8} f_i(p,q;p\cdot q)\,\tau_i^\mu, \tag{3.14}$$

and

$$\Gamma^\mu(p,q;p\cdot q) = \sum_{i=1}^{8} g_i(p,q;p\cdot q)\,\rho_i^\mu, \tag{3.15}$$

where the normalized momenta have to be expressed in the corresponding Lorentz invariants. The change of basis is now readily computed. The relation between the dressing functions of the outer basis, f_i, and the dressing functions of the inner basis, g_i, follows from evaluating

$$\begin{aligned} &\frac{1}{4}\mathrm{Tr}_D\left\{\bar{\tau}_i^\mu, \sum_{j=1}^{8} f_j(p,q;p\cdot q)\,\tau_j^\mu\right\} \\ = \ &\frac{1}{4}\mathrm{Tr}_D\left\{\bar{\tau}_i^\mu, \sum_{j=1}^{8} g_j(p,q;p\cdot q)\,\rho_j^\mu\right\}. \end{aligned} \tag{3.16}$$

The left hand side of this equation yields $f_i\left(p,q;p\cdot q\right)$ per construction, while the right hand side can be evaluated either by hand or by using e.g. FORM [89]. Evaluating the right hand side of (3.16) one finds for the desired dressings $g_i\left(p,q;p\cdot q\right)$

$$\begin{aligned} g_i &= \frac{1}{\sqrt{2}} f_i \text{ for } i \in \{1,3,5,7\}\,, && (3.17)\\ g_2 &= f_2 - \frac{1}{\sqrt{2}} f_5, && (3.18)\\ g_4 &= f_4 + \frac{1}{\sqrt{2}} f_7, && (3.19)\\ g_6 &= f_6 - \frac{1}{\sqrt{2}} f_1, && (3.20)\\ g_8 &= f_8 + \frac{1}{\sqrt{2}} f_3. && (3.21) \end{aligned}$$

3.4 Renormalization

The renormalization of the system is performed by employing a momentum subtraction (MOM) scheme for the propagator, the vertex is renormalized by using the Slavnov-Taylor identity, as we will detail below. The quark propagator has two dressing functions, A and B, see Figure A.1. The formal structure of the decoupled self-consistent integral equations is given by

$$\begin{aligned} A &= Z_2 + Z_{1F}\Sigma_A, && (3.22)\\ B &= Z_2 Z_m m_0 + Z_{1F}\Sigma_B, && (3.23) \end{aligned}$$

with $\Sigma_{A,B}$ the self energy parts. In the following, a subscript s means that the corresponding quantity has to be taken at the renormalization point s. The renormalized dressing functions A and B are then given by

$$\begin{aligned} A &= \underbrace{A_s}_{=1} + Z_{1F}\left(\Sigma_A - \Sigma_{A,s}\right) && (3.24)\\ &= 1 + Z_{1F}\left(\Sigma_A - \Sigma_{A,s}\right), \end{aligned}$$

$$\begin{aligned} B &= \underbrace{B_s}_{=m_0} + Z_{1F}\left(\Sigma_B - \Sigma_{B,s}\right) && (3.25)\\ &= m_0 + Z_{1F}\left(\Sigma_B - \Sigma_{B,s}\right), \end{aligned}$$

where we used the renormalization conditions that the dressing functions A and B should acquire a value of 1 and m_0 at the renormalization point respectively. The renormalization constant Z_{1F} is determined via the Slavnov-Taylor identity,

$$Z_{1F} = \frac{Z_2}{\tilde{Z}_3}, \tag{3.26}$$

and is also used for the vertex equation.

3.5 Solving the system

This section is meant as an instruction manual of how the system of the propagator equation and the vertex equation can be solved. Many aspects of the procedure are further detailed in Appendix B, such that the computation can be reproduced if desired. Note that this calculation is presented for non-parallel execution. Once the single core code has been written and tested, one can parallelize it as discussed below. Running as one thread on a standard desktop computer, the system converges within a couple of hours with reasonable precision.

3.5.1 Preparational steps

We want to solve the coupled integral equations (3.4) and (3.5). The propagators and vertices are defined as shown in Figures A.1 and A.2, so we have ten integral equations to solve. Two correspond to the propagator dressings A and B, the remaining eight equations correspond to the vertex. For the vertex on the right hand side of equation (3.4) we employ the basis system (3.15) for the vertex. The same basis is also used for the two quark-gluon vertices on the right hand side of the vertex equation (3.5). On the left hand side of equation (3.5) however, we use the orthonormal basis system given by equation (3.14). As a first step, one has to find the equations for A and B. To this end, we perform the projections

$$P_A = \frac{1}{4}\mathrm{Tr}_D\left\{\frac{i\not{p}}{p^2}\circ\right\}, \tag{3.27}$$

$$P_B = \frac{1}{4}\mathrm{Tr}_D\left\{\circ\right\}, \tag{3.28}$$

on both sides of equation (3.4), where $\circ$ has to be replaced by either the left or the right hand side of (3.4) respectively. For the vertex equation we perform a similar procedure, this time using

$$P_{f_i} \quad = \tfrac{1}{4}\mathrm{Tr}_D \quad \{\bar{\tau}_i^{\mu} \circ\}\,, \tag{3.29}$$

which gives rise to eight equations corresponding to the eight dressing functions in the orthonormal basis $f_i\,(p, q; p \cdot q)$. The Lorentz contractions and Dirac traces are conveniently computed using FORM [89], where the number of terms can be reduced considerably if the gluon momenta in the non-abelian diagram are abbreviated by introducing new variables, $u^\mu = w^\mu - q^\mu$ and $v^\mu = p^\mu - w^\mu$. A further reduction is possible by using the transverse projected three-gluon vertex, see Section B.1.4 for details on this step.

3.5.2 Numerical strategy

In this section we briefly discuss the numerical strategy we used to solve the system of DSEs. For all angles appearing in the system of equations we use nodes and weights according to a quadrature based on Gauss-Chebyshev polynomials of the second kind [90][4]. For the radial grid however, we employ two different grids that have no coinciding nodes[5] Having different grids externally and internally provides numerical stability, as numerically pathological points are removed in an elegant way, see Section J.1 of Appendix J for details.

Using different integration grids for external and internal nodes makes it clear that we have to interpolate the quark-propagator and the quark-gluon vertex throughout the calculation. The internal grid is applied for the loop momenta q and w, see (3.4) and (3.5), where the former is the loop momentum of the quark self-energy, the latter the loop momentum of the non-abelian diagram. The propagators are evaluated at the external grid-points and are interpolated at the values of the internal grid using cubic spline interpolation. Employing cubic splines adds global information to the system, as the functions are expected to be smooth in the end. For the vertex we have to deal with the same situation, only that we have two external grids, one for the square of the momentum p and one for the square of q. One could use bi-cubic spline interpolation here, and in fact we use this technique to calculate the output once the system has converged to the desired level of accuracy – however, throughout the iteration the necessity of splining both

[4]For this study, 8 angular nodes are sufficient

[5]This procedure has been suggested by Richard Williams.

external vertex grids at the same time does not arise, as the left vertex in the non-abelian diagram has one external leg with momentum q^2 and the right vertex has one external leg with momentum p^2. Also in the quark-self energy there is one leg which only requires external information. It is thus sufficient to use one-dimensional cubic splines to spline-interpolate at values of w^2, one time for the left leg and one time for the right leg of the vertex.

3.5.3 Parallelization

Designing the system as discussed above provides also a setting that is suitable for a hybrid CPU-GPU based parallelization. One can use MPI threads for coarse graining the external grids of both, the propagator and the vertex equation and use GPUs to operate on the internal grids. A parallelized implementation will become available at [81].

3.5.4 Validity of the results

This calculation has been implemented also by a fellow PhD student [81]. At the time of writing this thesis we established agreement for a defined set of parameters, up to a small overall shift of our solutions. The eight vertex dressings and the propagator are however in perfect qualitative agreement. We present the numerical solutions of the fully dressed quark-gluon vertex, an analysis of the importance of the structures, as well as solutions that have been obtained with a reduced set of tensor structures below.

3.6 Numerical results

Here we present the numerical results that have been obtained following the procedures described in Section 3.5 and Appendix B.

3.6.1 Solution with all eight tensor structures

In the following we present the solution of the coupled system of the fully dressed quark-gluon vertex and the quark propagator. We see dynamical chiral symmetry breaking as indicated by the mass function acquiring a non-zero value in the infrared. In this truncation and with our numerical approach we do not see a scaling behavior of the vertex. The fact that the system decouples in the infrared might be due to numerical reasons. This issue is definitely an interesting subject for future studies. We proceed by presenting solutions of the system with a reduced set of tensor structures and show the

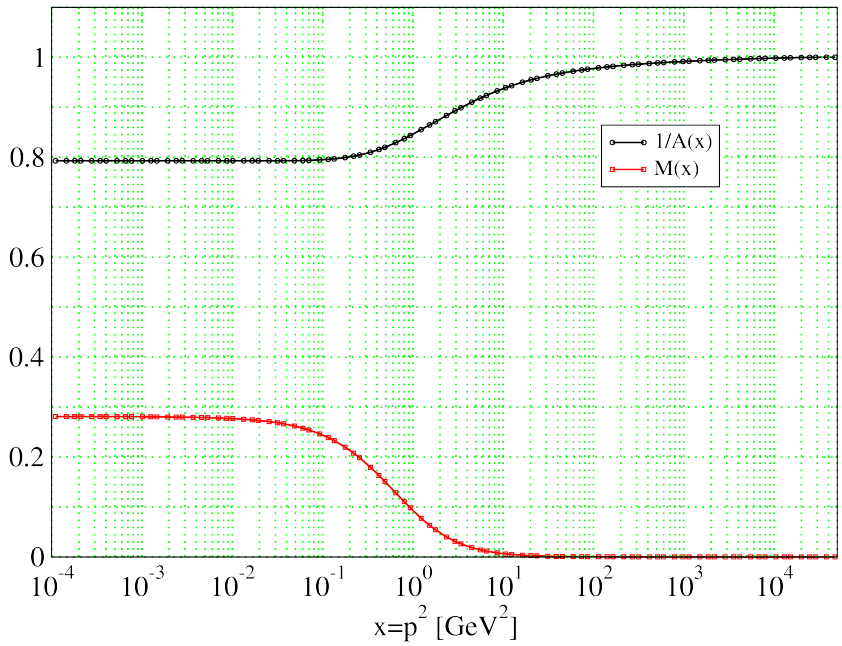

Figure 3.5: The solution of the quark-propagator dressing functions with all 8 vertex dressing functions taken into account, leading to dynamical chiral symmetry breaking as indicated by the mass function. The mass function is obtained from $M(x) = \frac{B(x)}{A(x)}$. The parameters of this and all the other runs are given in the main text.

impact of the various basis elements on the dressing functions of the vertex and the propagator. The calculations in this section have been performed in the chiral limit with an IR cut-off of 10^{-4} GeV^2, an UV cut-off of 5×10^4 GeV^2, where we used the last node as renormalization point. For this calculation we used 32 external nodes and 93 internal integration nodes, as well as 8 angular nodes for all angles. The value of the coupling at the renormalization point has been put to $\alpha_s = 0.1$, and the renormalization constant $Z_{1F} = 1$. The three-gluon vertex has been modeled by equation (3.3). In Figure 3.5 we show the solution of the quark-propagator dressing functions with all vertex dressings taken into account. In Figures 3.6 and 3.7 we show the solutions of the chirally symmetric and anti-symmetric tensor structures of the vertex at the kinematic points where the squares of the external momenta are equal and where the cosine of the angle between them vanishes[6].

[6]In fact, almost vanishes, as we evaluate the expression at the angular node that is closest to zero. With 8 second-kind Gauss-Chebyshev quadrature nodes this is around $z = \pm 0.1736$.

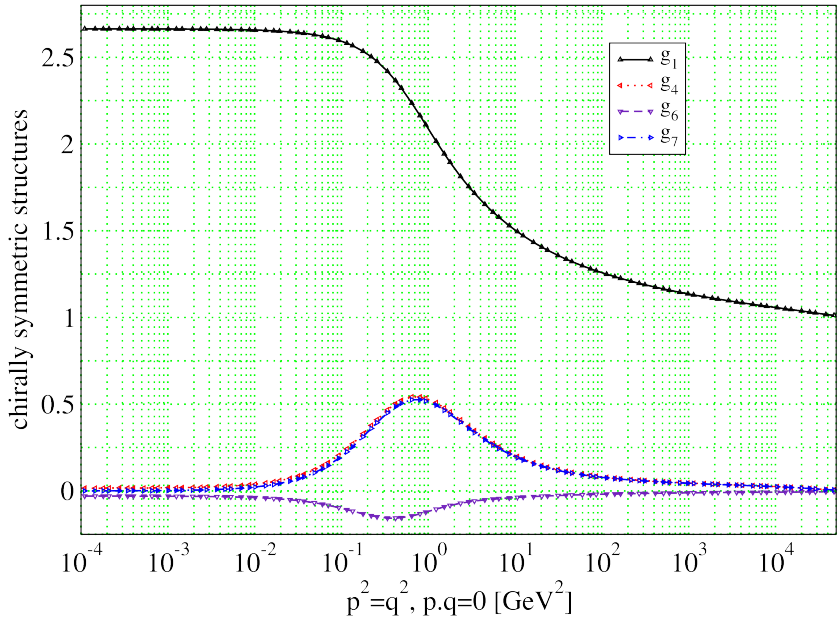

Figure 3.6: The full solution of the four dressing functions going with the chirally symmetric tensor structures.

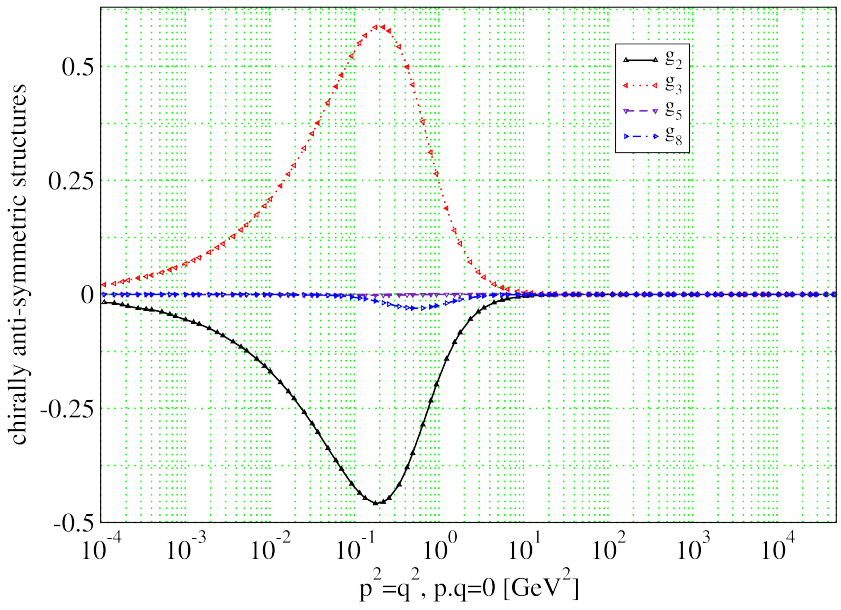

Figure 3.7: The full solution of the four dressing functions going with the chirally anti-symmetric tensor structures.

3.6.2 Solutions with one tensor structure removed

In this section we provide solutions of the system where one tensor structure has been removed. By doing that we can see the effect of individual tensor structures on the system. The tree-level structure $\rho_i^\mu = \gamma_T^\mu$ is kept in all reduced systems. For every solution with $\{g_i\} \setminus g_j,\ j \in [2, 8]$, where the g_i are the dressing functions of the basis elements summarized in Table 3.2, we show the chirally symmetric and anti-symmetric dressing functions of the quark-gluon vertex. Additionally, the propagator dressing functions $1/A$ and M are shown as an inset-plot in the anti-symmetric solutions. In all plots we show the full solution given by thin solid lines with symbols marking the node positions. The dashed and dashed-dotted lines correspond to the solutions of the reduced system. All runs have been made using 32 external radial nodes distributed according to J.1 over a range given by an IR cut-off of 10^{-4} GeV^2 and an UV cut-off of 5×10^4 GeV^2. We used 3 intermediate Gauss-Legendre nodes for every interval with neighboring external nodes, such that we have $3 \times (32 - 1) = 93$ internal integration nodes. The renormalization point used for this calculation is 5×10^4 GeV^2. All plots have been generated for $p^2 = q^2$ and $p \cdot q = 0$, and represent just one slice of the three-dimensional array. Qualitative insights into the effects of removing structures can still be observed, in particular also the effect on the propagator dressings. A quantitative analysis of the effect of removing tensor structures will be presented in a paper on the quark-gluon vertex, as well as in [81], where the effect on the pion decay constant and the chiral condensate will be studied.

3.6.3 Solution with three tensor structures removed

The analysis of the importance of the tensor structures suggests that we can at least neglect three structures, namely ρ_5^μ, ρ_6^μ and ρ_8^μ, see Figures 3.14, 3.15, 3.16, 3.17, 3.20 and 3.21. The solutions of the dressings with the reduced system are shown in Figures 3.22 and 3.23.

3.7 Conclusions

In this Chapter we presented solutions of the fully dressed quark-gluon vertex, coupled to the quark propagator Dyson-Schwinger equation. The propagator acquires a dynamical mass. The eight vertex dressings show a decoupling behavior in our numerical implementation. This behavior has to be investigated more closely in future studies. We investigated the impact of the tensor structures on the solution of the reduced system. We found two tensor structures to be negligible, the elements ρ_5^μ and ρ_8^μ. They cause only very

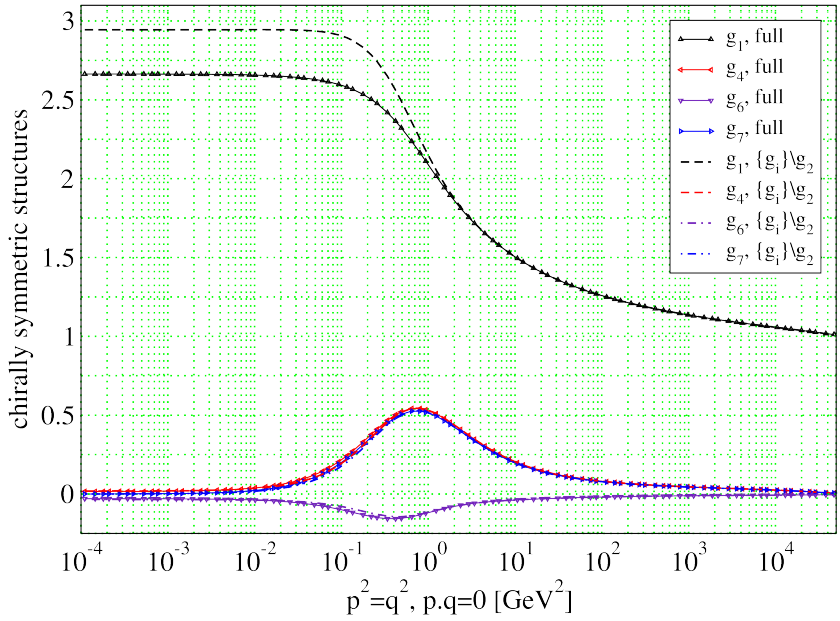

Figure 3.8: Chirally symmetric solutions of the vertex without ρ_2^μ. Neglecting this structure leads to some overshooting of the tree-level structure, the remaining solutions are practically on top of each other.

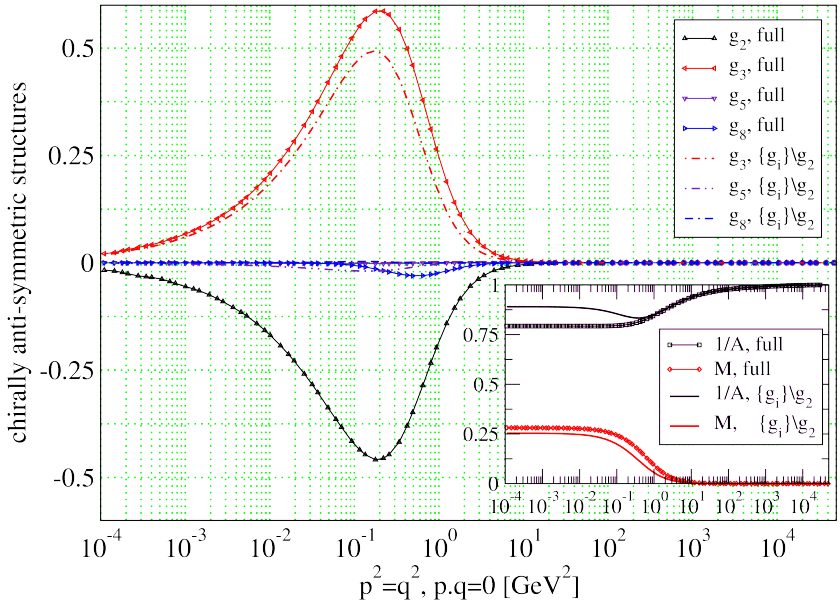

Figure 3.9: Chirally anti-symmetric solutions of the vertex without ρ_2^μ. Only minor deviations can be found when the second structure is neglected. The mass generation (see inset plot of $1/A$ and M) is close to the one of the full solution.

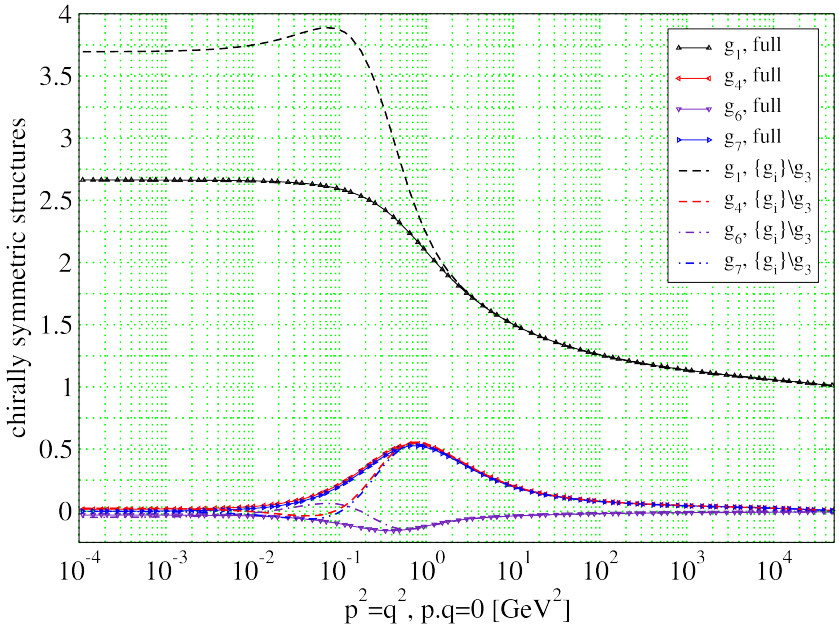

Figure 3.10: Chirally symmetric solutions of the vertex without ρ_3^μ. Neglecting the third structure leads to a significant shift in the dressings of the other tensor structures.

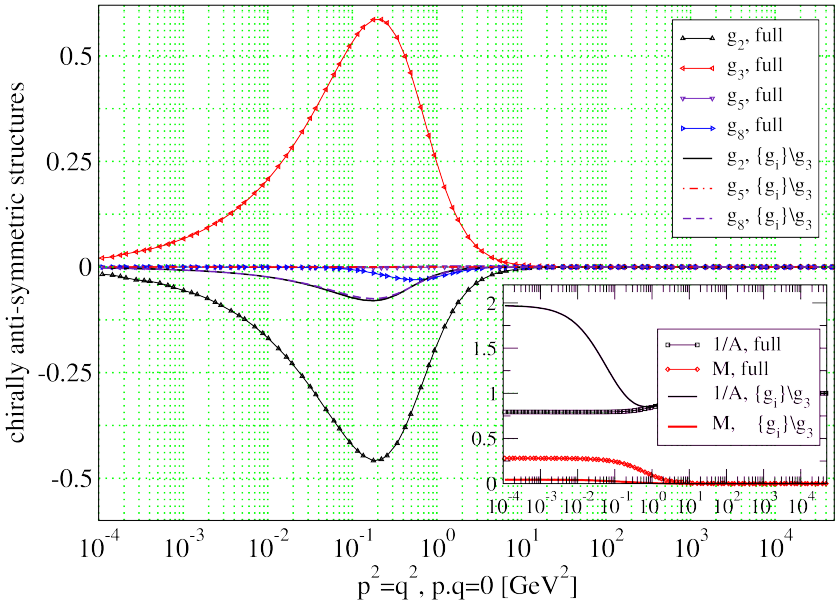

Figure 3.11: Chirally anti-symmetric solutions of the vertex without ρ_3^μ. Without the third structure, no mass is generated (see inset plot of propagator), so it has to be taken into account.

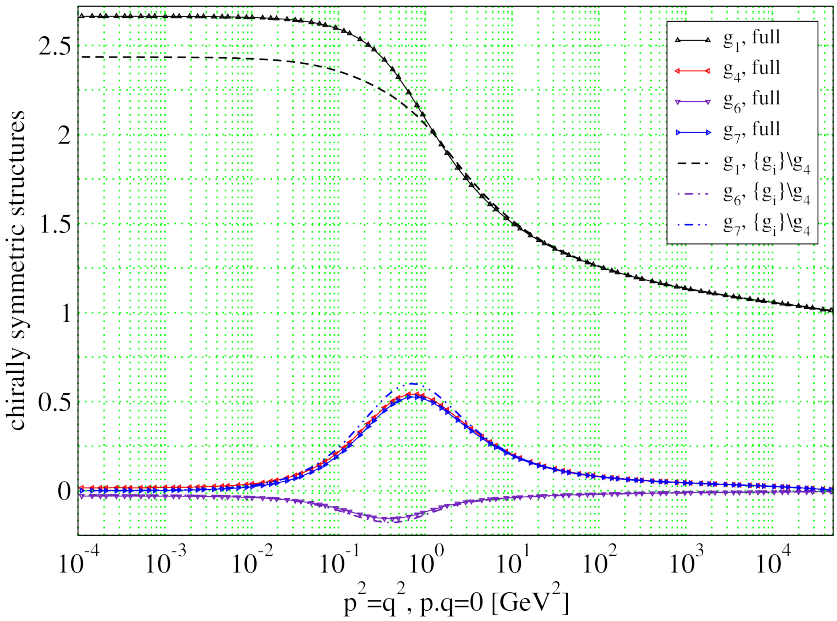

Figure 3.12: Chirally symmetric solutions of the vertex without ρ_4^μ. The effect is a slight shift in most of the remaining dressings.

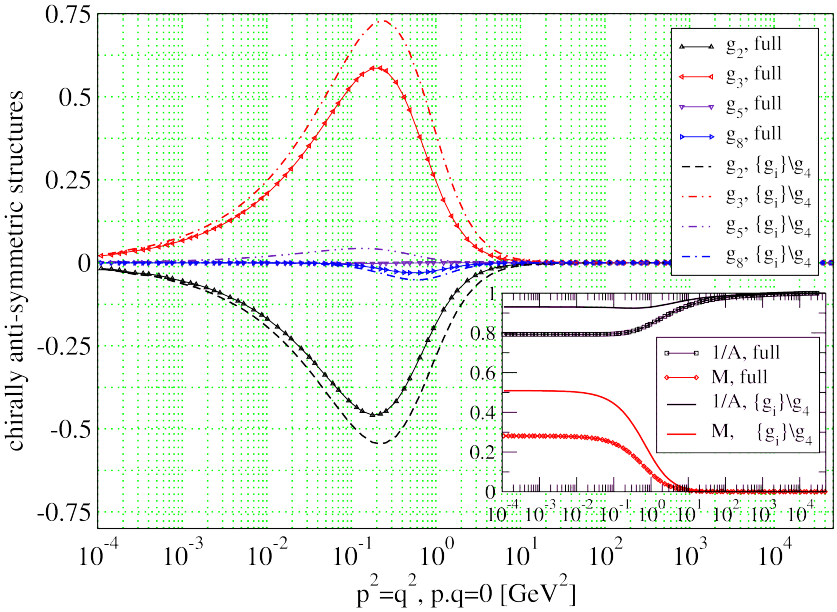

Figure 3.13: Chirally anti-symmetric solutions of the vertex without ρ_4^μ. All remaining structures are shifted when neglecting the fourth dressing. The dynamical mass overshoots its original value by almost 100 percent.

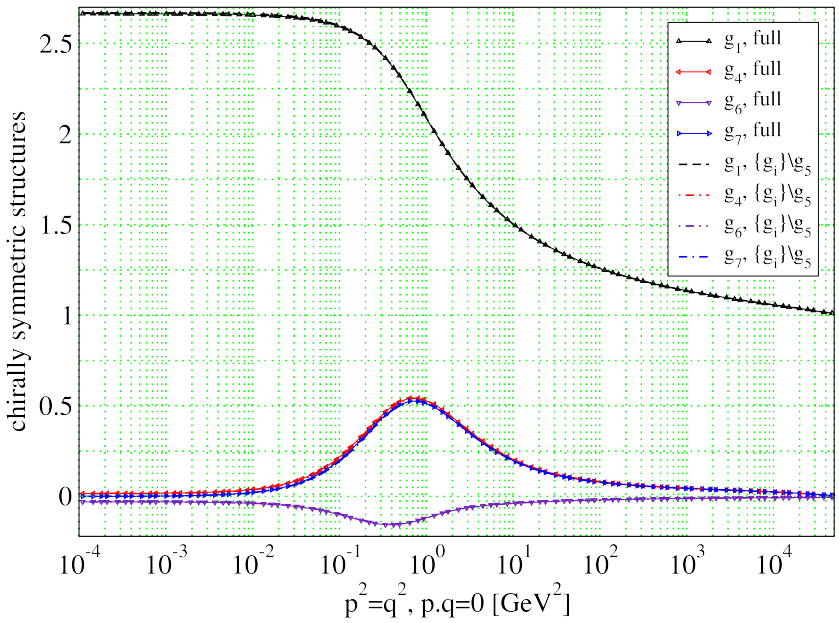

Figure 3.14: Chirally symmetric solutions of the vertex without ρ_5^μ. This structure can safely be neglected, as there is no visible effect from removing it.

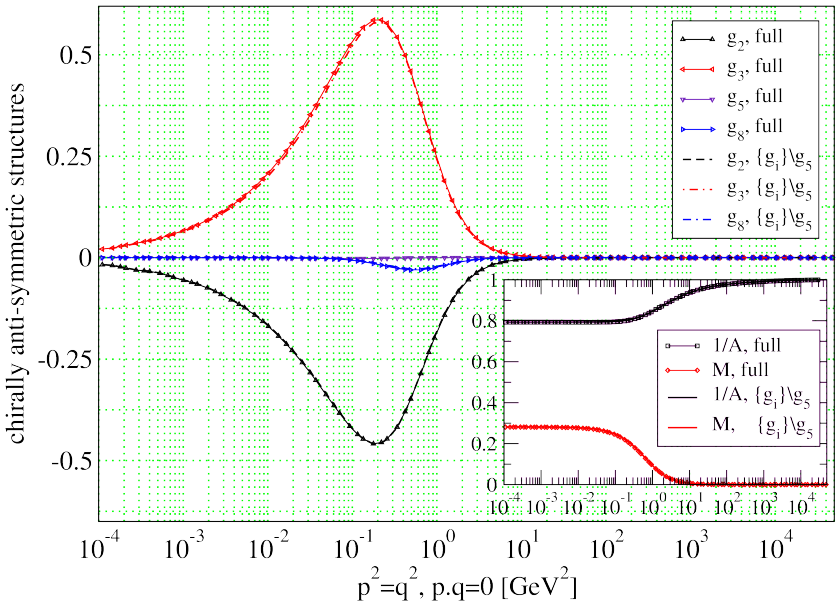

Figure 3.15: Chirally anti-symmetric solutions of the vertex without ρ_5^μ. The solution is practically unchanged when the fifth structure is removed. Also the propagator dressings are on top of each other.

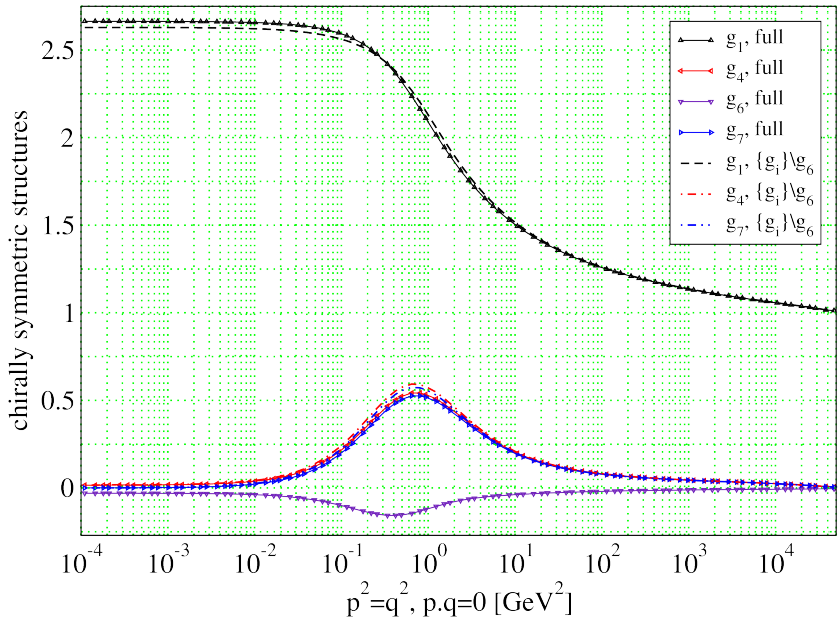

Figure 3.16: Chirally symmetric solutions of the vertex without ρ_6^μ. This structure can safely be neglected, as there is no visible effect from removing it.

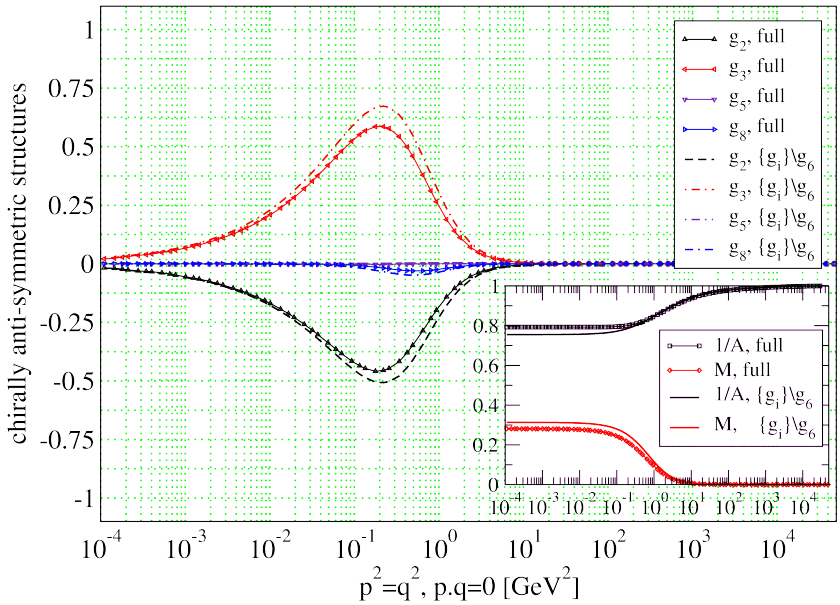

Figure 3.17: Chirally anti-symmetric solutions of the vertex without ρ_6^μ. There is a small effect on the propagator dressing functions visible.

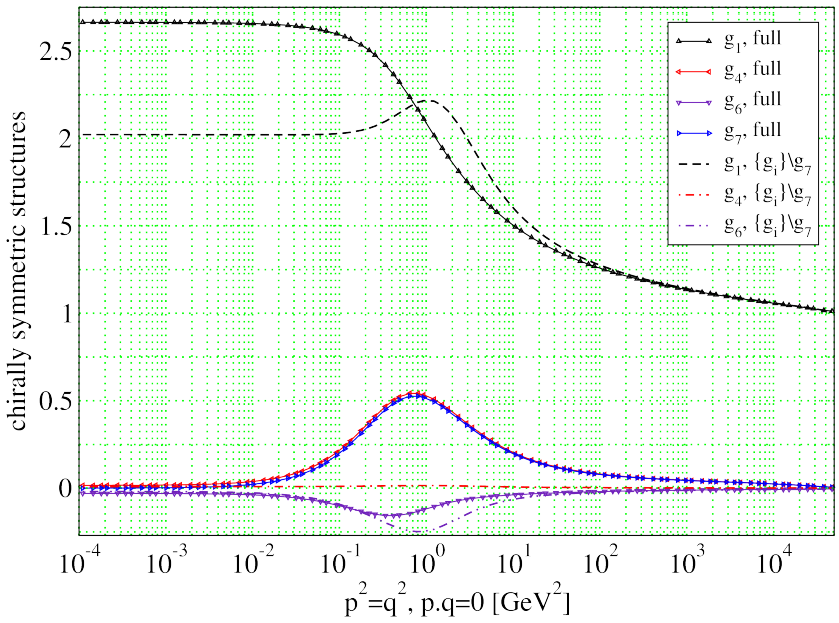

Figure 3.18: Chirally symmetric solutions of the vertex without ρ_7^μ. This structure has to be taken into account.

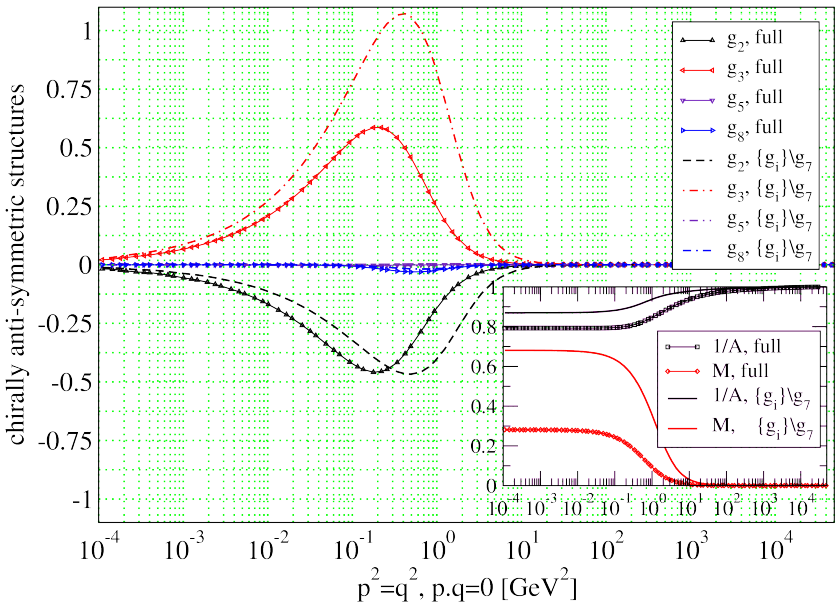

Figure 3.19: Chirally anti-symmetric solutions of the vertex without ρ_7^μ. All dressings respond to the removal of this structure.

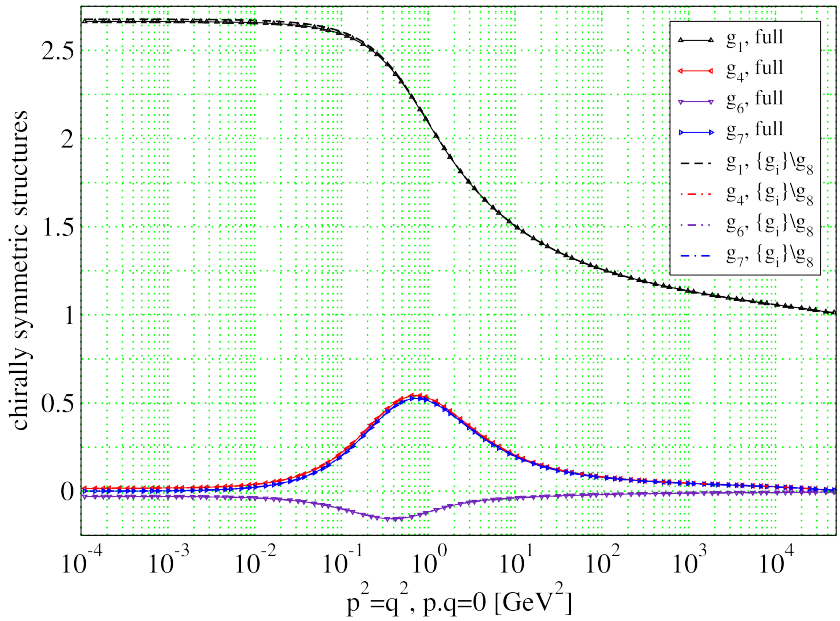

Figure 3.20: Chirally symmetric solutions of the vertex without ρ_8^μ. This structure can safely be neglected, as there is no visible effect from removing it.

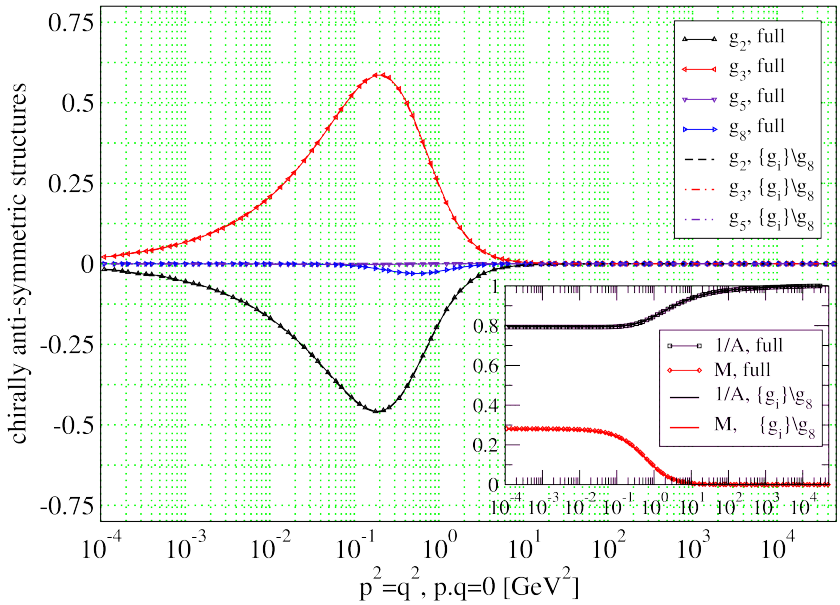

Figure 3.21: Chirally anti-symmetric solutions of the vertex without ρ_8^μ. Like the fifth structure, this basis element can be neglected.

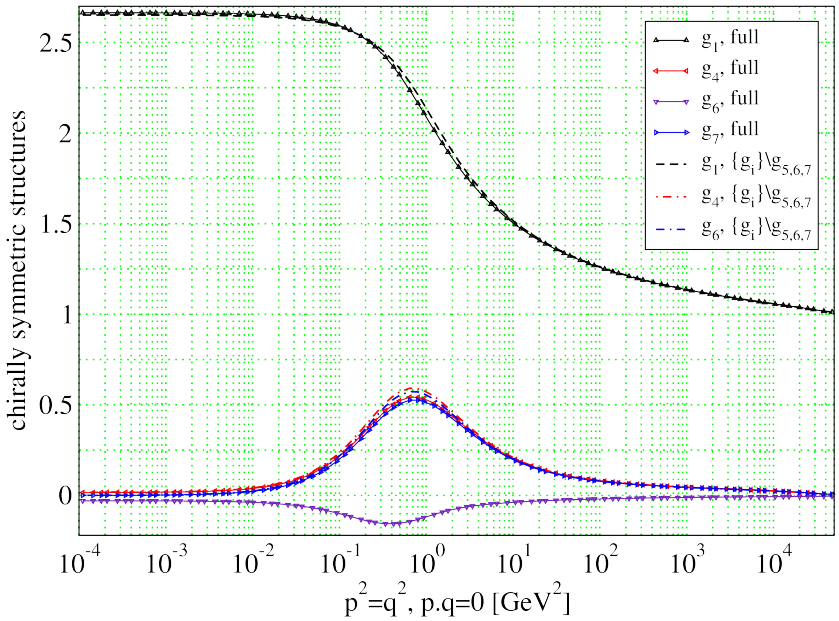

Figure 3.22: Chirally symmetric solutions of the vertex without structures ρ_5^μ, ρ_6^μ and ρ_8^μ.

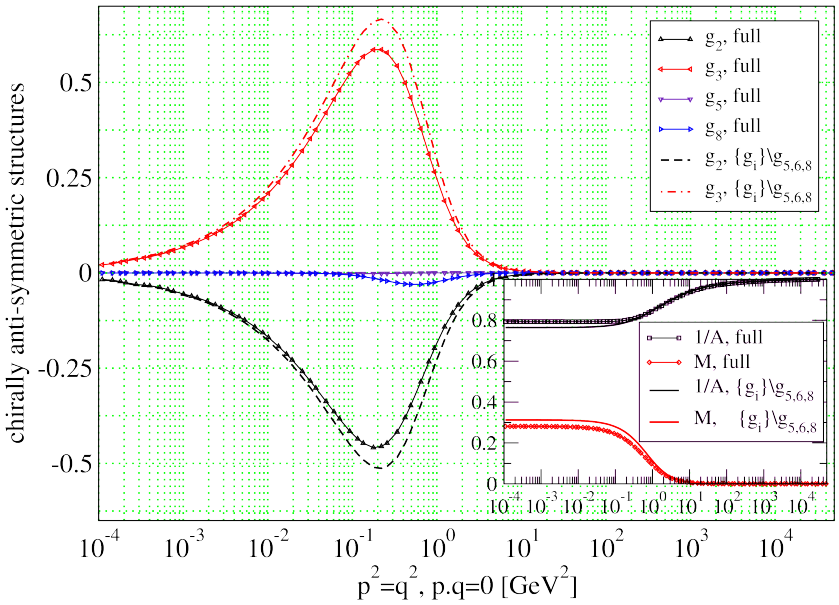

Figure 3.23: Chirally anti-symmetric solutions of the vertex without structures ρ_5^μ, ρ_6^μ and ρ_8^μ. Even with only 5 structures left, the system produces results that deviate only slightly from the full solution.

slight deviations from the full result. Depending on the desired level of accuracy one might also neglect another tensor structure, namely the element ρ_6^μ. Also ρ_2^μ does not have a huge impact and might also be neglected. Next we will have to establish full quantitative agreement of our two independent solutions and quantify the qualitative discussion presented in this section. Another interesting aspect for future studies is to investigate the impact of the three-gluon vertex on the solution. Reducing the system to the four most important tensor structures might also make non-vacuum calculations feasible, and one could also try to include the reduced vertex in the study of the complex quark propagator discussed in Section 4.6 of Chapter 4.

Chapter 4

The analytic structure of Green's functions

4.1 Introduction

This chapter is dedicated to the computation of the analytic structure of Green's functions in Euclidean space. Over the years, various attempts of calculating the analytic structure of fermionic Green's functions have been made, see [91, 92, 93, 94, 52] for a not complete list of studies throughout the last decades. The constant interest in this field is not surprising, as the analytic structure of Green's functions plays an important role in bound state equations such as the Bethe-Salpeter equation (BSE). Additionally, studying the analytic structure of fundamental Green's functions is a very interesting subject on its own, as the notion of reflexion positivity provides a simple mechanism of confinement by expelling degrees of freedom that violate this property from the space of physical states. Here we are interested in calculating the analytic properties of the Landau gauge quark propagator DSE numerically. Only very recently, a study on this subject has been published [95]. However, we try to not restrict the area of evaluation to a parabolic region, but we are aiming at solving the quark propagator for arbitrary complex external momenta. Such an investigation has also become available for the gluon propagator recently, where the authors solved the gluon Dyson-Schwinger equation in the complex plane [54]. In order to compute the analytic structure of the quark propagator, the analyticity properties of the quark-gluon vertex will play an important role. In [96], the authors consider the coupled system of the quark and quark-gluon vertex DSE for complex Euclidean momenta[1], where they employ a numerical method developed in

[1] See also [26] for a very recent study.

[27]. For a study performed in Minkowski space see e.g. [97].

This Chapter is organized as follows. First we introduce our numerical technique and apply it to perturbative Yang-Mills one-loop studies, see Appendix F and Sections 4.2, 4.4, 4.5[2]. In Section 4.6 we discuss a possible extension of the method to non-perturbative self-consistent integral equations. The major difference as compared to the perturbative case is, that the location of the poles induced by the quark propagator are not known a priori. As these poles play a decisive role in the determination of the actual form of the contour deformation, we have to find a way to address this issue in order to get the deformation right. The numerical setting is also more demanding as in the perturbative case. In order to make up for the increasing numerical effort, we developed a hybrid parallelization framework using CPUs and GPUs. While the framework is already set up and tested, the computation of the analytic structure of the quark propagator DSE is still work in progress by the time of writing this thesis.

4.2 A test case for the numerical procedure

The aim of this section is to provide the numerical framework that we developed in order to cope with the problems arising throughout the calculations of perturbative one-loop amplitudes in the complex plane of squares of the external momentum. The advantage of studying perturbative expressions before considering non-perturbative quantities lies in the fact that the analytic structure of the integrand of the loop integral can be fully analyzed, which allows for the development of contour deformations without having to deal with the problem that the actual structure of the integrand is not known beforehand[3], as it is the case for the dressed quark propagator showing up in the quark self-energy of the propagator DSE. In order to perform high accuracy calculations for a reasonable number of x-points[4] in the complex plane ($x = p^2$, the square of the external momentum) we use GPUs for parallelization. As a test case, we use equation (32) of [100], which is a correlator that can be computed analytically in the complex plane. The calculation and the result is presented in [100]. Here we will use their result as a test case for our numerical procedure, whose most general form is described in Appendix F. Furthermore we will use this example to explicitly work out each of the steps of the procedure, such that the interested reader can apply it to a suitable

[2]The perturbative method and an application have been published in [98, 99]

[3]This issue will be addressed below when we discuss the extension of the method to non-perturbative treatment.

[4]We used 128^2, 256^2 and 512^2 lattices in the complex plane.

problem.

The correlator of the test example is given by

$$\mathscr{G}\left(p^2\right) = \int \frac{d^D k}{(2\pi)^4} \frac{1}{(p-k)^2 - i\sqrt{2}\theta^2} \frac{1}{k^2 + i\sqrt{2}\theta^2}. \tag{4.1}$$

In Ref. [100] they show, that in four Euclidean dimensions, with the choice of $2\sqrt{2}\theta^2 = 1$, the solution of the (regularized) correlator (4.1) takes the form

$$\mathscr{G}_{sub}\left(x\right) = \frac{1}{16\pi^2}\left(1 - \frac{\pi}{2x} + \frac{\sqrt{1-x^2}}{x}\arccos\left(x\right)\right). \tag{4.2}$$

The aim is to obtain this result employing our numerical procedure, where we furthermore rescale the result such that the trivial pre-factor is gone,

$$\mathscr{G}_{sub,rescaled}\left(x\right) = \left(1 - \frac{\pi}{2x} + \frac{\sqrt{1-x^2}}{x}\arccos\left(x\right)\right). \tag{4.3}$$

Now we can elaborate each of the steps outlined in Appendix F.

4.2.1 STEP 1 (A): *Hyper-spherical coordinates*

We have to evaluate $(16\pi^2) \times$ [Eq. (4.1)] for $D = 4$ and with $2\sqrt{2}\theta^2 = 1$. Switching to hyper-spherical coordinates using equation (A.7), we get

$$\begin{aligned} \mathscr{G}_{rescaled}\left(x\right) &= \frac{16\pi^2}{(2\pi)^3}\int_0^\infty dy\; y \int_{-1}^{1} dz\sqrt{1-z^2} \\ &\quad \times \frac{1}{\left(x + y - 2\sqrt{x}\sqrt{y}z - \frac{i}{2}\right)} \frac{1}{\left(y + \frac{i}{2}\right)} \end{aligned} \tag{4.4}$$

4.2.2 STEP 2 (A): *Regularization*

The superficial degree of divergence follows from equation (4.1) with $D = 4$. The integral measure yields four powers in the loop momentum k, and the propagators yield -2 powers in k each, such that we are left with a superficial degree of divergence $s = 4 - 4 = 0$. The integral diverges logarithmically. Using equations (F.4) and (F.5) we construct the regularized integrand,

$$\begin{aligned}\mathscr{F}_{sub}\left(x,y,\sqrt{x}\sqrt{y}z\right) &= \left(1-t^0\right)\mathscr{F}\left(x,y,\sqrt{x}\sqrt{y}z\right) \\ &= \frac{1}{\left(x+y-2\sqrt{x}\sqrt{y}z-\frac{i}{2}\right)}\frac{1}{\left(y+\frac{i}{2}\right)} \\ &\quad -\frac{1}{\left(y-\frac{i}{2}\right)}\frac{1}{\left(y+\frac{i}{2}\right)} \\ &= \frac{-x+2\sqrt{x}\sqrt{y}z}{\left(x+y-2\sqrt{x}\sqrt{y}z-\frac{i}{2}\right)\left(y^2+\frac{1}{4}\right)}.\end{aligned} \tag{4.5}$$

With this integrand the correlator becomes

$$\begin{aligned}\mathscr{G}_{rescaled}\left(x\right) &= \frac{2}{\pi}\int_0^\infty dy\; y\int_{-1}^{1}dz\sqrt{1-z^2} \\ &\quad \times\frac{-x+2\sqrt{x}\sqrt{y}z}{\left(x+y-2\sqrt{x}\sqrt{y}z-\frac{i}{2}\right)\left(y^2+\frac{1}{4}\right)},\end{aligned} \tag{4.6}$$

where we also canceled the trivial pre-factor.

4.2.3 STEP 3 (A,N): *Analysis of the integrand*

In this step we have to determine the analytic structure in the complex plane of the radial integration variable, induced by the angular integral. First, let us follow the procedure outlined in Appendix D. With the definitions

$$\begin{aligned}\mathscr{G}_{rescaled}\left(x\right) &= \frac{2}{\pi}\int_0^\infty dy\;\underbrace{\frac{y}{\left(y^2+\frac{1}{4}\right)}}_{A} \\ &\quad \times\underbrace{\int_{-1}^{1}dz\sqrt{1-z^2}\frac{-x+2\sqrt{x}\sqrt{y}z}{\left(x+y-2\sqrt{x}\sqrt{y}z-\frac{i}{2}\right)}}_{B},\end{aligned} \tag{4.7}$$

we see that A features two poles in the complex $y-$plane at $y=\pm\frac{i}{2}$. The angular integral B induces a branch cut in the y-plane. Following the analytic approach first, we look at the denominator (now again expressed in terms of momenta p and k) in search for all values of k such that

$$p^2+k^2-2pk\cos\theta_1-\frac{i}{2} = 0 \tag{4.8}$$

is satisfied. We find two redundant solutions for this equation, which can be used as a parametrization for the branch cut,

$$\tilde{\xi}\left(p^2,\theta_1\right) \;=\; p\cos\theta_1 \pm \sqrt{-p^2\sin\theta_1+\frac{i}{2}},\; 0\le\theta_1\le\pi. \tag{4.9}$$

As we have found the solution with respect to k, the parametrizations of the branch cut in the complex plane of the radial momentum square, y, is given by

$$\xi\left(p^2,\theta_1\right) \;=\; \left(\sqrt{p^2}\cos\theta_1 \pm \sqrt{-p^2\sin\theta_1+\frac{i}{2}}\right)^2,\; 0\le\theta_1\le\pi. \tag{4.10}$$

We have found complex conjugate poles, as well as a branch-cut in the complex y-plane, where the pole information can be read off term A of equation (4.7), while the branch cut parametrization is given by equation (4.10). We also performed this analysis numerically, where we used again GPUs to evaluate the angular integral for a given value of x with high precision. Figure 4.1 shows that we find perfect agreement with the analytic prediction.

Now we have to work out the restrictions imposed on the contour by this branch cut. In this case it turns out that there is a parabola shaped region in the complex plane of x where no contour deformation is necessary, see Figure 4.2.

It is convenient to split the complex plane into regions where different classes of contour deformations are employed. Region 1 does not need any deformation, so we only have to find contour deformations for the regions 2 to 5.

- **Region 2 and 5**
  - $\mathscr{C}_{(2,5),1}:\; 0\le t\le 1$
    $\mathscr{C}_{(2,5),1}(t) = 15t\exp\{i\arg(x)\}$
  - $\mathscr{C}_{(2,5),2}:\; 1\le t\le 2$
    $\mathscr{C}_{(2,5),2}(t) = 15(2-t)\exp\{i\arg(x)\} - (1-t)\Lambda^2$
- **Region 3**
  - $\mathscr{C}_{3,1}:\; 0\le t\le 1$
    $\mathscr{C}_{3,1}(t) = t0.4i$
  - $\mathscr{C}_{3,2}:\; 1\le t\le 2$
    $\mathscr{C}_{3,2}(t) = 0.1(\sin((2-t)\pi) + i(\cos((2-t)\pi)+5))$

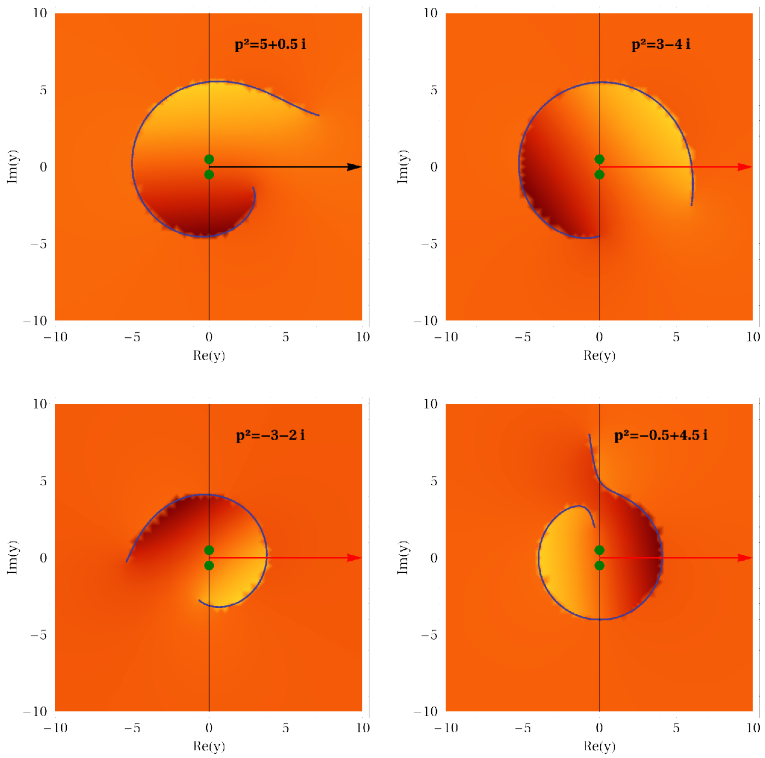

Figure 4.1: The analytic structure in the complex y-plane for given $x \in \mathbb{C}$. The solid lines are visualizations of equation (4.10), the density plot in the background has been obtained numerically on a GPU. The arrow running from the origin along the positive real axis represents the undeformed radial integration contour. Only in the upper left plot the contour is not affected by the branch cut.

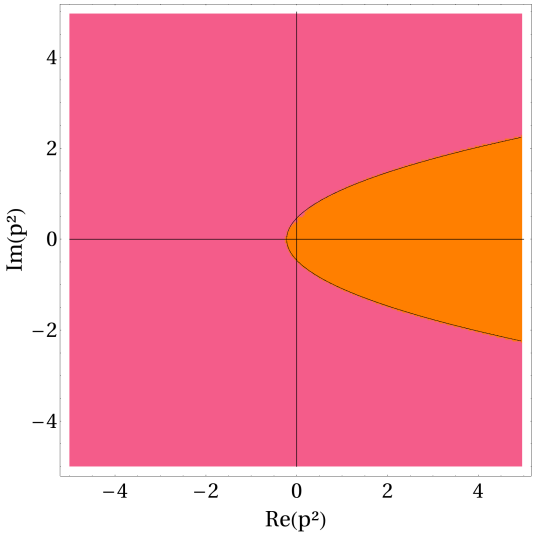

Figure 4.2: In the parabolic region one can keep the contour undeformed, while in the region outside of the parabola the contour has to be modified.

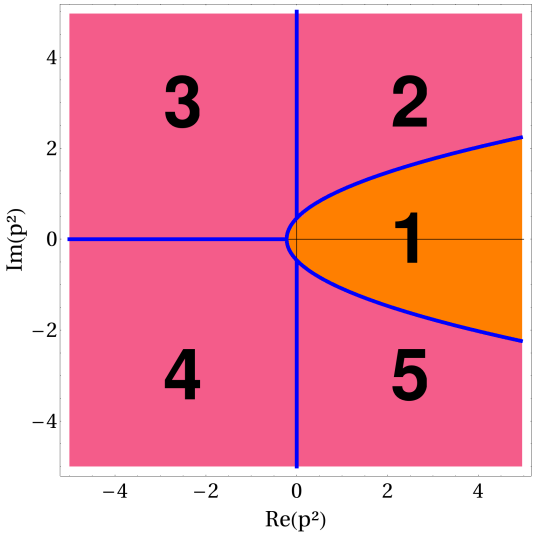

Figure 4.3: The complex plane is split into regions where different classes of contour deformations are employed.

  - $\mathscr{C}_{3,3}: \ 2 \leq t \leq 3$
    $\mathscr{C}_{3,3}(t) = (3-t)(0.6i) - (2-t)13\exp\{i\arg(x)\}$
  - $\mathscr{C}_{3,4}: \ 3 \leq t \leq 4$
    $\mathscr{C}_{3,4}(t) = (4-t)13\exp\{i\arg(x)\} - (3-t)(-20+18i)$
  - $\mathscr{C}_{3,5}: \ 4 \leq t \leq 5$
    $\mathscr{C}_{3,5}(t) = (4-t)(-20+18i) - (3-t)\Lambda^2$

- **Region 4**

  - $\mathscr{C}_{4,1}: \ 0 \leq t \leq 1$
    $\mathscr{C}_{4,1}(t) = -t0.4i$
  - $\mathscr{C}_{4,2}: \ 1 \leq t \leq 2$
    $\mathscr{C}_{4,2}(t) = 0.1(\sin((t-2)\pi - \pi) + i(\cos((t-2)\pi - \pi) - 5))$
  - $\mathscr{C}_{4,3}: \ 2 \leq t \leq 3$
    $\mathscr{C}_{4,3}(t) = (3-t)(-0.6i) - (2-t)13\exp\{i\arg(x)\}$
  - $\mathscr{C}_{4,4}: \ 3 \leq t \leq 4$
    $\mathscr{C}_{4,4}(t) = (4-t)13\exp\{i\arg(x)\} - (3-t)(-20-18i)$
  - $\mathscr{C}_{4,5}: \ 4 \leq t \leq 5$
    $\mathscr{C}_{4,5}(t) = (4-t)(-20-18i) - (3-t)\Lambda^2$

Figures 4.4 to 4.6 show examples of contours in this regions[5].

4.2.4 STEP 4 (N): *Initialization*

For this test case we used a discrete lattice for the complex values of x of size 128^2. We restricted the region in the complex plane to $-5 \leq \Re x \leq 5$ and $-5 \leq \Im x \leq 5$. The discrete points are equally distributed over the these intervals. This preparation step is performed on a GPU, where the complex matrix is filled with the discretized x values. Patches in multiples of the warp size[6] are executed in parallel on the GPU. In this preparation step, but also for the actual evaluation, each thread running on the GPU operates on one point of the external grid only. The fact that blocks can be 2-dimensional quantities allows for a straight-forward mapping of the threads to the grid-points. A perturbative integral in the complex plane is a perfect candidate for parallelization on a GPU, as there is no communication between the individual threads required. One could also use multiple GPUs,

[5] Two dimensional animations of the contours moving with the external parameter x can be found on the DVD enclosed to this thesis. For a short description of the movies see Appendix K.

[6] See e.g. [98] for a brief discussion of GPU programming.

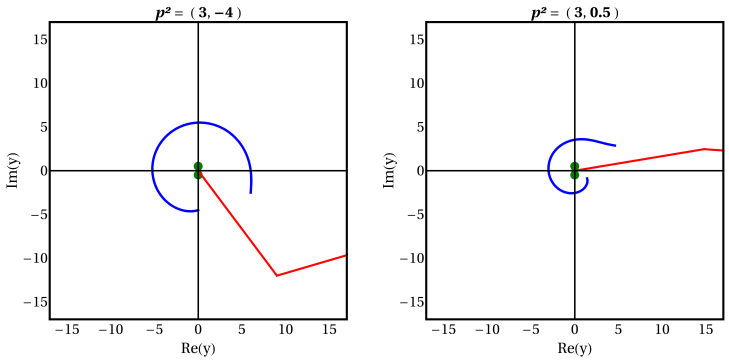

Figure 4.4: The dots are poles, the circular line is the branch cut. The contour is composed of straight line segments. Left: Contour deformations employed in regions 2 and 5. Right: This point lies within the parabola, so one could also keep the contour undeformed.

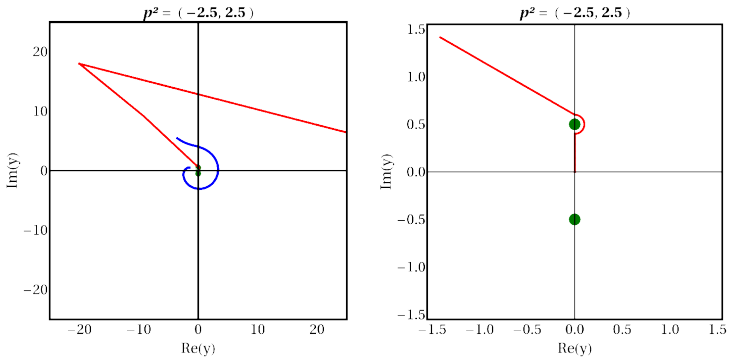

Figure 4.5: The dots are poles, the circular line is the branch cut. The contour is composed of straight line segments. Left: Contour deformation employed in region 3. Right: The pole is avoided by a small circular deformation.

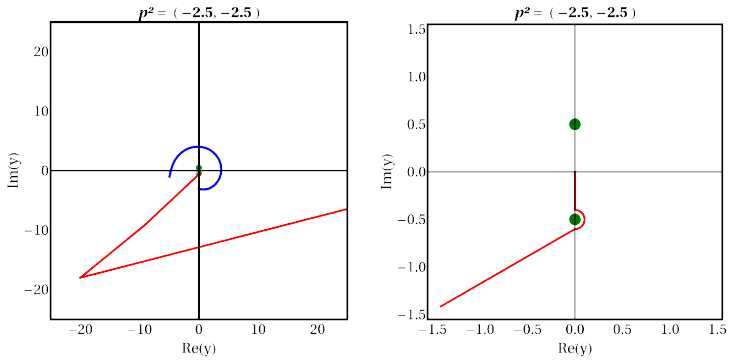

Figure 4.6: The dots are poles, the circular line is the branch cut. The contour is composed of straight line segments. Left: Contour deformations employed in region 4. Right: Again the pole is avoided by a small circular deformation.

as we employ for the non-perturbative case. There, however, communication becomes important.

4.2.5 STEP 5 (N): *Evaluation*

This is the final step of the procedure. For each value in the matrix that has been constructed in the previous step, a dynamically adjusted contour is computed by a thread on the GPU. As before, each thread operates on one entry only and performs the integrations, where the radial integration now runs along the appropriate contour. As always we use non-adaptive Gaussian quadrature rules to perform the numerical integration. For visualization, we processed the data using Mathematica.

4.2.6 Numerical results

In Figures 4.7 and 4.8 we show the results of our computation. The solid plots show the exact solution (4.3), the blue dots are the numerical solutions on a 128^2 grid. Running times on the GPU are summarized in Table 4.1.

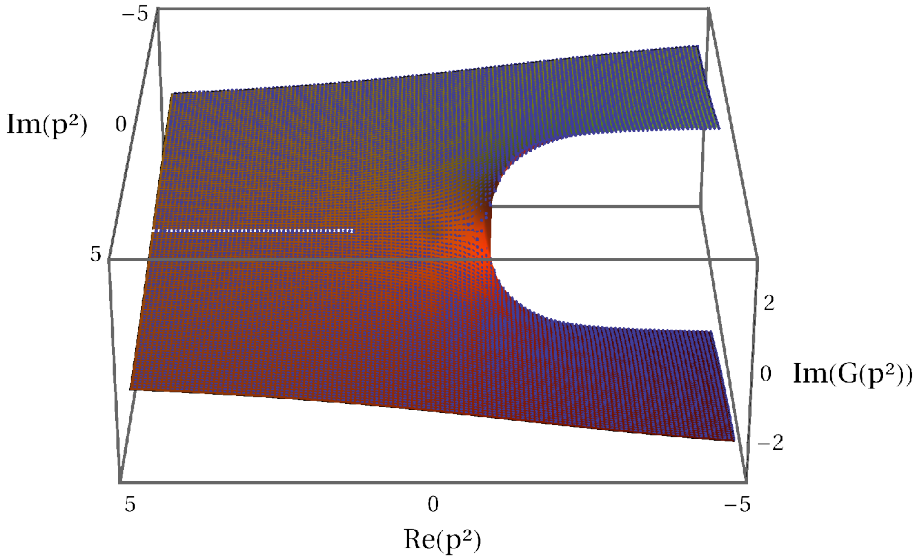

Figure 4.7: The imaginary part of the solution. The solid plot corresponds to the exact solution (4.3), the blue dots have been obtained numerically by employing our algorithm on a GPU.

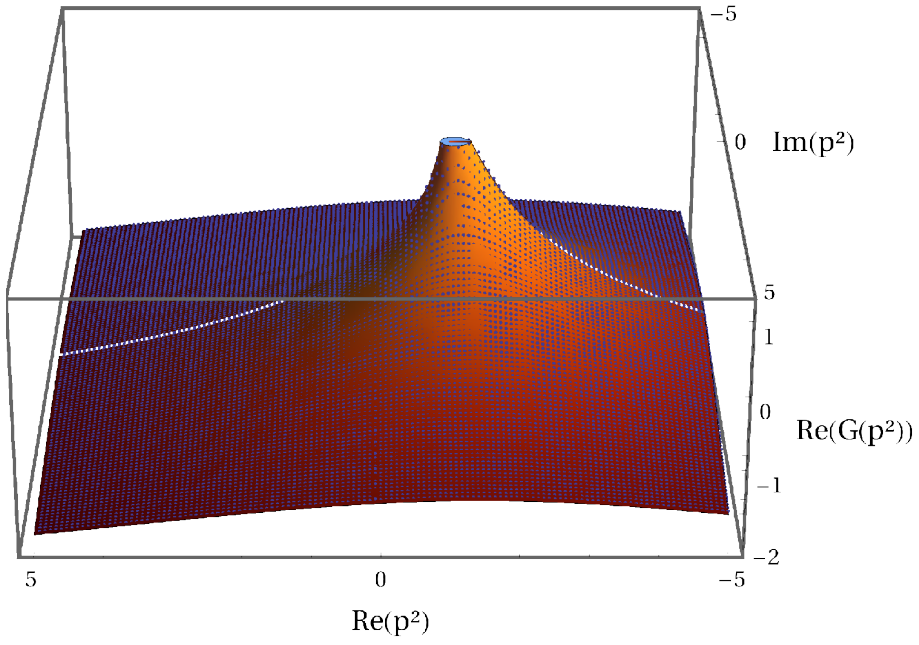

Figure 4.8: The real part of the solution. The solid plot corresponds to the exact solution (4.3), the blue dots have been obtained numerically by employing our algorithm on a GPU.

	Intel CPU	**NVIDIA GPU**		
Device	Xeon X5650	GTX 550 Ti	GTX 480	Tesla C2070
Runtime	252m 2s	6m21s	4m21s	2m38s
Speedup (A)	1	≈ 39.6	≈ 57.9	≈ 95.5
Speedup (B)	1	≈ 3.3	≈ 4.9	≈ 8.1

Table 4.1: Comparison of running times on various GPUs. In case 'A' we compared the GPU running time against one thread running on the Xeon CPU. This is however a quite unfair comparison, so we included case 'B', where we use the one-thread data and adapted it to $2 \times 6 = 12$ hypothetical threads running on the 6 cores of the Xeon using Hyper-Threading.

4.2.7 Conclusions

The procedure outlined above, as well as the results of the test case depicted in Figures 4.7 and 4.8 show that we have developed a framework that allows for fast and reliable numerical calculations of the analytic structure of Green's functions. If a higher level of parallelization is sought, one can easily extend the procedure to use multiple GPUs, as we employ for the non–perturbative case. Even though the test case can be solved without the need of any numerics, it still features all the non-trivial obstacles typically arising in this kind of calculations. This particular test case is a very valuable opportunity for a comparison, as it allowed us to learn how to cope with the obstructive structures arising in the radial integrand. The method is now ready to use and has been published in [98].

4.3 Scalar glueball operators at the Born level

In Section 4.2 we proved the validity of our numerical approach that evaluates correlators perturbatively at one-loop level in the complex plane. Now we want to apply this procedure to a case that cannot be solved analytically. While still operating at the perturbative level, we are interested in calculating the analytic structure of a correlator of two Yang-Mills field strength tensor squares, $\langle F^2(x)\, F^2(0)\rangle$, which corresponds to a scalar glueball. Details of this study can be found in [99, 101]. Glueballs are studied in a variety of approaches, for a review see e.g. [102]. The expression of the momentum space operator corresponding to the F^2 correlator in d Euclidean dimensions is presented in [100]. In Appendix G however, we give an explicit derivation for the expression and re-obtain the result of [100]. The d-dimensional

expression at the Born level reads

$$\mathscr{O}\left(p^2\right) = \int \frac{d^d k}{(2\pi)^d} \mathscr{G}\left(k^2\right) \mathscr{G}\left((p-k)^2\right) \left(k^2 (p-k)^2 + (d-2)\left(k \cdot (p-k)\right)^2\right), \tag{4.11}$$

where

$$\langle F^2(x) F^2(0)\rangle_d = \int \frac{d^d p}{(2\pi)^4} \exp\left\{i\ p \cdot x\right\} \mathscr{O}_d\left(p^2\right). \tag{4.12}$$

Born level means, that throughout the construction of $\mathscr{O}\left(p^2\right)$ we completely neglect the presence of the non-abelian term in the field strength tensor. The functions $\mathscr{G}\left(p^2\right)$ are the scalar parts of the gluon propagators we plug into the expression,

$$D_{\mu\nu}(p^2) = \left(\delta_{\mu\nu} - \frac{p_\mu p_\nu}{p^2}\right) \mathscr{G}(p^2). \tag{4.13}$$

The transverse projectors of the gluons have been absorbed throughout the construction of the expression. Even though the self-interacting part of the field strength tensor is missing, we are now in the comfortable position that we can use non-perturbative gluonic expressions as an input. The advantage of being able to do that is at least two-fold. On the one hand, using fits to non-perturbatively obtained gluon propagators introduces some amount of self interaction again, such that from this point of view one might consider this framework as being semi-perturbative. On the other hand, as we are interested in using positivity violation as a signature of 'confinement'[7] here, so we use positivity violating parametrizations as an input. The construction should then take care of producing a positivity respecting quantity, which is an interesting thing to observe. In the following we study the two-dimensional and the four-dimensional case, where we use two different types of parametrizations for the gluon propagators in the latter case.

4.4 The analytic structure of F^2 in two dimensions

We start by considering the two-dimensional case, because in two dimensions the expression corresponding to the correlator diverges only quadratically,

[7] By this we just mean that degrees of freedom possessing negative norm contributions are absent from the space of asymptotic states.

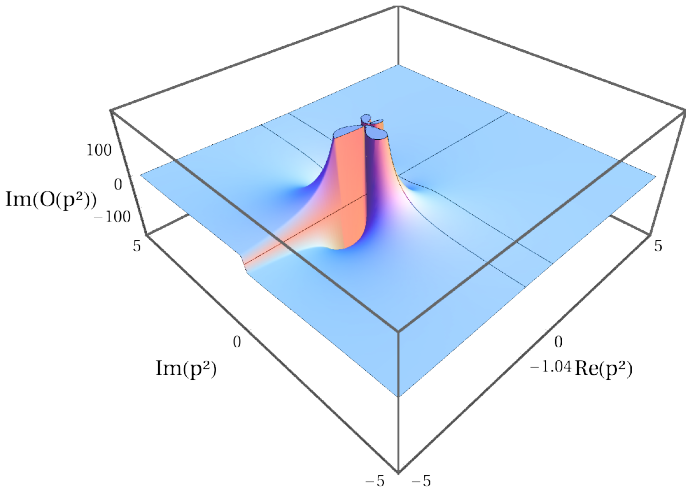

Figure 4.9: Imaginary part of the solution of (4.12) using (4.14) as an input. There are two branch-cuts (one lies behind the peaked structure).

allowing for an easier treatment. The two-dimensional case features only one type of solution, whose infrared parametrization reads [52]

$$\mathscr{G}(p^2) = w\frac{1}{p^2}\left(\frac{p^2}{p^2+\Lambda^2}\right)^{1+2\kappa}, \tag{4.14}$$

with $\kappa = 0.2$ [103]. The value $\kappa = 0$ has also been considered and excluded by [104]. The parametrization (4.14) reproduces lattice data [105, 106] and solutions from functional methods [104] with $w = 1.065$ and $\Lambda = 1$ GeV. However, we used the 4-dimensional parameters $w = 2.5$ and $\Lambda = 0.51$ GeV also for the two dimensional case, which allows for easier comparison. UV and mid-momentum deviations are small and irrelevant for this study. Using Cutkosky cut-rules [107], one expects a branch cut at the position $x = -1.04$ GeV^2. However, the cut-rules are not exactly applicable in this scenario, see for example [108]. Nevertheless we can perform the analysis outlined in Appendix E to predict the position of the branch-point. This analysis confirms the point $x = -1.04$ GeV^2 as a branch point, however, we find an additional branch point at $x = -\Lambda^2 = -0.2601$ GeV^2.

4.4.1 Numerical results

Performing the numerics on a GPU, we obtain the results shown in Figures 4.9 and 4.10.

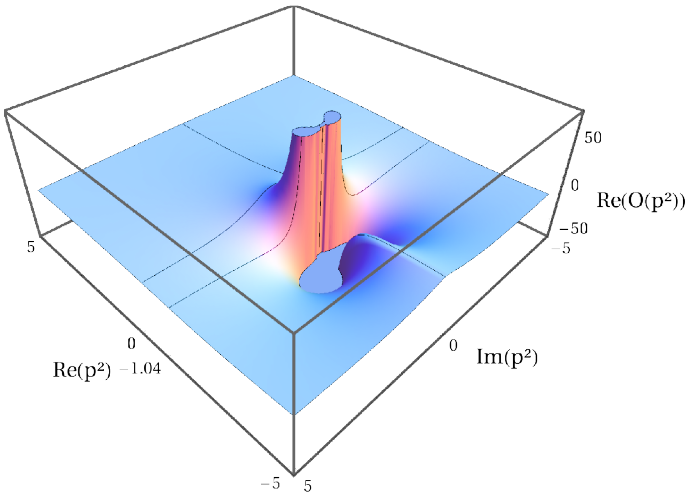

Figure 4.10: Real part of the solution of (4.12) using (4.14) as an input.

There are two branch cuts showing up in the solution, as predicted by the analysis of the integrand. One starts at $x_1 = -1.04$ GeV^2 and runs towards $\Re x \to \infty$. The other cut has an opposite discontinuity and opens at $x_2 = -0.26$ GeV^2, running towards the first branch point x_1. The discontinuity has been extracted and is shown in Figure 4.11. The peaked structure located at x_1 is also shown as a density plot in Figure 4.12.

4.4.2 Conclusions

The extraction of the analytic structure of the two dimensional case only served as a technical test case for to prepare the numerics for the four dimensional investigation. Interestingly, we get an additional branch cut of finite length in this case. The origin of this cut might be some truncation artifact. The remaining branch cut gives rise to a negative spectral density, signaling the absence of the computed quantity from the asymptotic state space. This is of course expected, as in two dimensions there are no glueballs present. The resolution of the branch points however worked well and the calculation produced smooth and trustable results. We can thus move on to the physically more interesting four dimensional case.

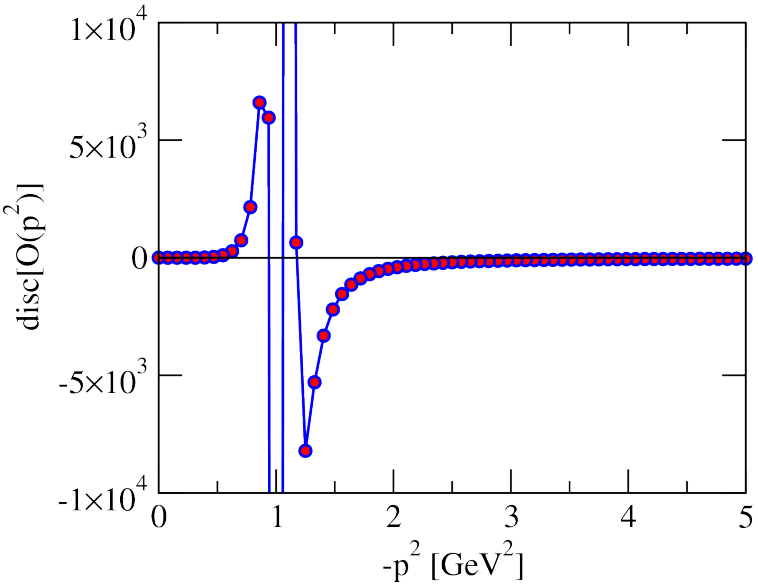

Figure 4.11: The discontinuity of the 2-dimensional case. There are two branch cuts present, see main text.

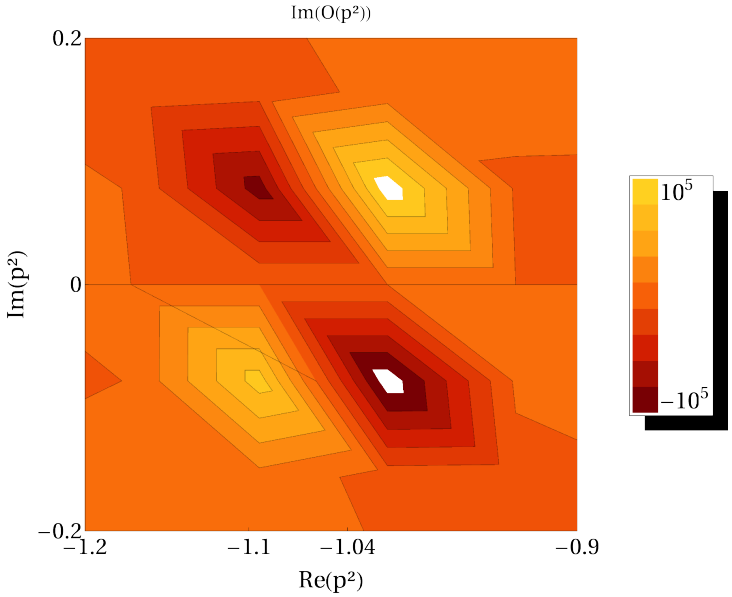

Figure 4.12: A density plot of the peaked structure that arises in the 2-dimensional case around $x_1 = -1.04$ GeV^2.

4.5 The analytic structure of F^2 in four dimensions

4.5.1 Decoupling propagator

Let us start the discussion of the four dimensional case by considering propagators of the decoupling-type first. From the functional equation point of view, there are two solutions to the gluon propagator, depending on the chosen boundary conditions of the equations [53]. There are solutions of the decoupling type [53, 109, 110, 111, 112] and the scaling type [53, 113, 114, 25], see also [115, 116, 31] for reviews on the subject. At zero momentum, the decoupling solution acquires a non-vanishing value, such that $\mathscr{G}(0)^{-1}$ serves as a screening mass. The scaling solution, on the other hand, vanishes like $(p^2)^{2\kappa-1}$ in the infrared, where $\kappa = 0.595353$[103, 117].

A decoupling fit of the form

$$\mathscr{G}(p^2) \sim 1/(p^2 + m^2), \tag{4.15}$$

featuring a constant mass is not suitable for reproducing lattice data [118, 119]. The introduction of a mass with momentum dependence, i.e. $m \to m\,(p^2)$, leads to better results. A model for the IR part of $m\,(p^2)$reads

$$m^2(p^2) = \frac{m_0^4}{p^2 + m_0^2}, \tag{4.16}$$

see [120], where also terms with the correct UV behavior are presented. In the Refined Gribov Zwanziger (RGZ) framework, more parameters are needed due to the dimension two condensates, see [121, 122]. A suitable fit-form reproducing lattice data is given by [123]

$$\mathscr{G}(p^2) = C\frac{p^2 + s}{p^4 + u^2p^2 + t^2}. \tag{4.17}$$

The fit eq. (4.15) with (4.16) is contained in this more general expression when choosing $s = u^2 = t = m_0^2$. For our study, we used the parameters summarized in Table 4.2.

Here we only employ and investigate the fit (4.17), but we do not work with the RGZ action[8]. A similar propagator has been used in a recent study

[8]If we did, we would get mixing between the F^2 operator with other operators [124].

C [1]	s [GeV^2]	t [GeV^2]	u [GeV]
0.784	2.508	0.72	0.768

Table 4.2: The parameters for the fit (4.17), see [123].

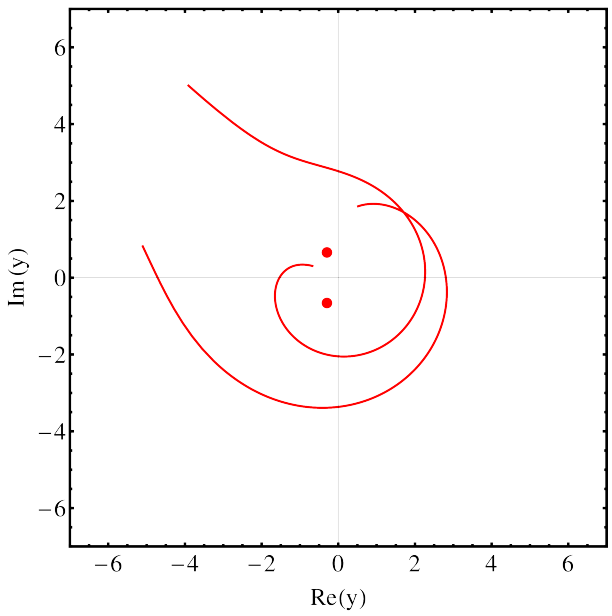

Figure 4.13: The imaginary part of the obstructive structure in the complex y-plane for an external momentum square x=-2+2i. The lines are cuts, dots correspond to poles. This parametrization has been obtained analytically, following the prescription in Appendix D.

and allowed for a pole mass extraction via bubble-resummation within the toy-model [125].

The decoupling case turned out to be rather complicated, as the numerical evaluation has to be performed very carefully. Following the steps of the procedure outlined in Appendix F, we have to perform a thorough analysis of the analytic structure of the radial integrand. As shown in Appendix D, branch cuts show up in the complex plane of the radial integration variable y. In the particular case of a propagator of the form (4.17), we find two branch cuts and a pair of complex conjugate poles in the complex y-plane. The exact shape and location of these non-analyticities has been extracted analytically, as well as numerically, see Figures 4.13 and 4.14.

Knowing the obstructive structure is most important, as the contours have to be adjusted in order to avoid them. They also allow for a prediction of where to expect the branch points of the result, see Appendix E for the

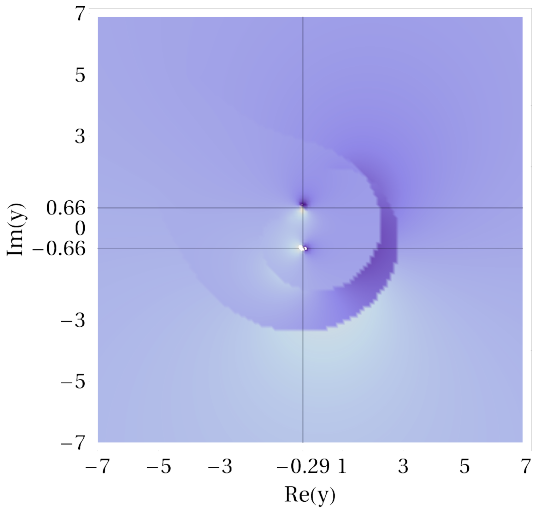

Figure 4.14: The imaginary part of the obstructive structure in the complex y-plane for an external momentum square x=-2+2i. This solution has been obtained by solving the angular integral for 128^2 values of $y \in \mathbb{C}$ numerically using a GPU. The obtained structure perfectly coincides with the one shown in Figure 4.13.

procedure. One can also employ the Cutkosky cut-rules. From the previous analysis we know that there are poles located at

$$k_{1,2}^2 \;=\; -0.29 \pm 0.66\, i. \tag{4.18}$$

Taking these values to Minkowski space, we can use

$$\left(\sqrt{-k_i^2} + \sqrt{-k_j^2}\right)^2, \tag{4.19}$$

to predict the branch-points. Hereby i and j are either 1 or 2. Taking the result back to Euclidean space, one obtains a branch point located at $x_1 = -2.03$ GeV^2 for $i \neq j$. For $i = j$, there are two solutions, $x_{2,3} = -1.18 \pm i2.63$ GeV^2. The latter cuts are considered as being unphysical, as they spoil the possibility to write down a spectral representation[9]. However, strictly speaking we used the cut rules for a situation where they are not applicable. However, we find agreement with the cut-rule based result when we employ the procedure of Appendix E. The result of our analysis is shown in Figures 4.15, 4.16 and 4.17.

[9]This was one of the motivations for the introduction of the so-called i-particles in [100].

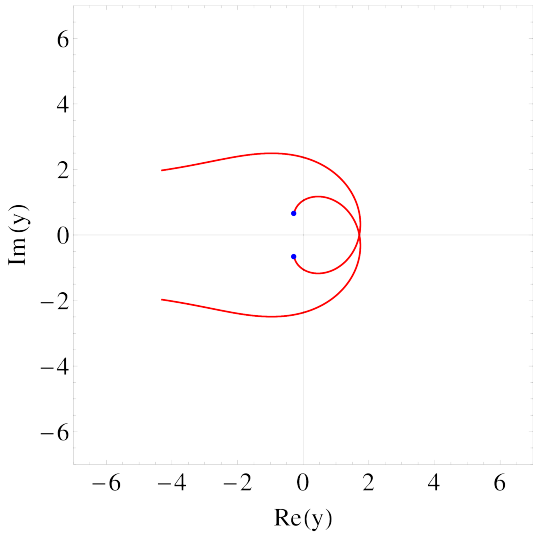

Figure 4.15: This configuration gives rise to the physical branch cut (lines). The poles are depicted as dots. Even though one might think that a contour connecting the origin with the UV cutoff can be obtained by continuous deformation from the axis, this is not the case, because regardless of whether the contour is closed above or below, one always picks up the residue of one of the poles. The external value for this situation is $x = -2.03\text{GeV}^2$.

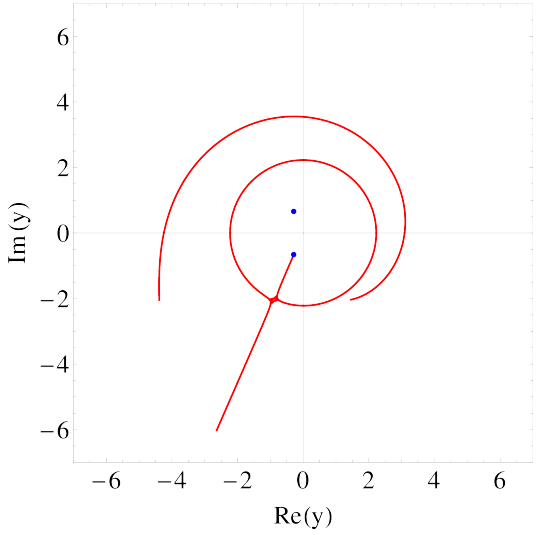

Figure 4.16: The configuration in the y-plane for $x = -1.18 - 2.7i$. Lines correspond to cuts, dots to poles. Also this value of x corresponds to a branch point of the overall expression.

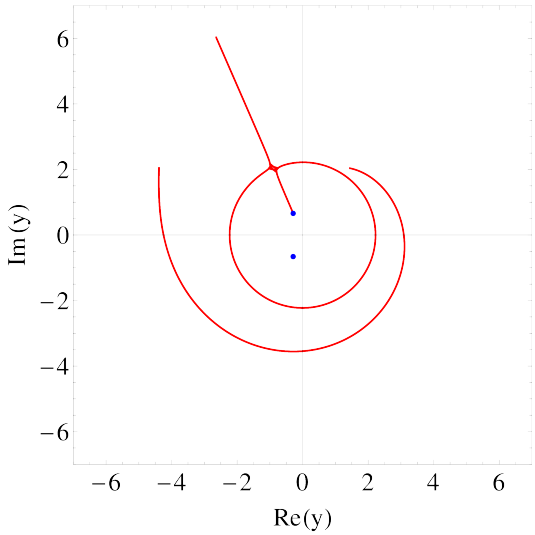

Figure 4.17: The complex conjugate situation of 4.16.

There are three 3d-movies concerning the obstructive structure and the branch-point locations of the overall expression on the DVD enclosed to this thesis, see Appendix K for a short description of the movies.

4.5.2 Numerical results: Decoupling propagator

The obstructive structure of the decoupling propagator fit we employed made it quite hard to produce a robust result numerically. We succeeded in getting smooth results, however, the branch point locations were very hard to resolve and led to a bad numerical signature for smaller values of x. In Figures 4.18 and 4.19 we show the imaginary and real part of the F^2 correlator using decoupling fits as input. All three branch cuts are clearly visible. Despite the bad resolution of the branch points, which causes a small dip to negative values of the discontinuity of the physical cut, the spectral density corresponding to the physical cut is positive everywhere, see Figure 4.20.

4.5.3 Scaling propagator

In the infrared, a four dimensional fit to the scaling propagator is given by [52]

$$\mathscr{G}(p^2) = w\frac{1}{p^2}\left(\frac{p^2}{p^2+\Lambda^2}\right)^{2\kappa}, \tag{4.20}$$

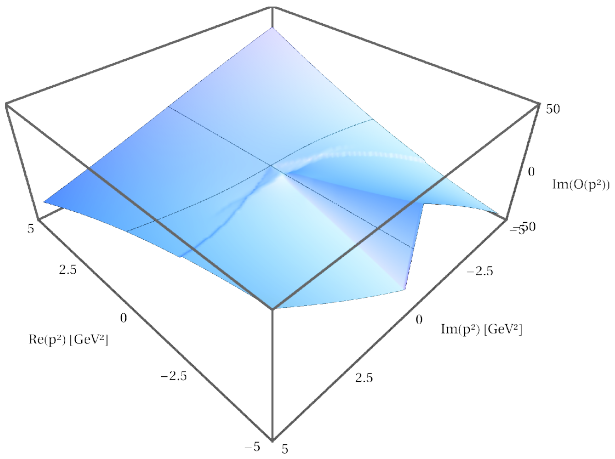

Figure 4.18: The imaginary part of the solution using a RGZ propagator fit. There are two unphysical cuts, as well as a physical cut in the solution. The branch point resolution is very bad, as the obstructive structure in the complex y-plane gives rise to a very noise numerical signal.

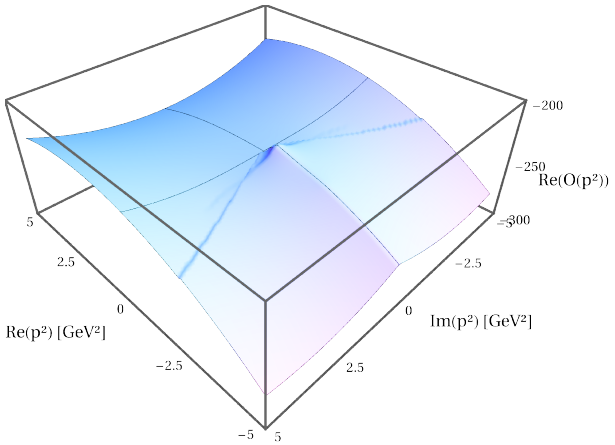

Figure 4.19: The real part of the solution using a RGZ propagator fit as input.

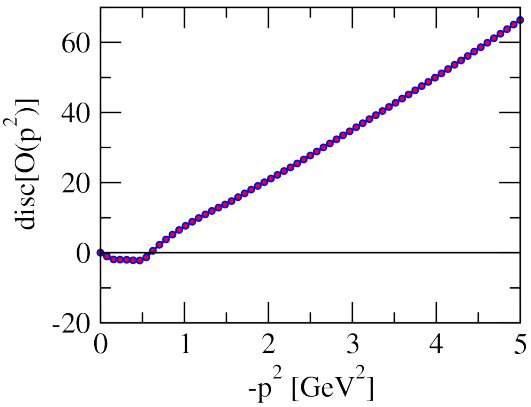

Figure 4.20: The discontinuity of the physical cut shown in Figure 4.18. Due to numerical issues, the discontinuity becomes negative in the beginning and rises too early, that is, the branch cut is expected to open much later.

with $\kappa = 0.595353$ [103, 117]. Here we neglected the UV part of the parametrization, as we are solely interested in the non-perturbative part of the propagator. The absence of the UV tail is also an advantage from a numerical point of view, as there is less structure to deal with. For the parameters in the fit we took $w = 2.5$ and $\Lambda = 0.51$ GeV. The obstructive structure arising in the complex y-plane can be avoided easily in the scaling case, such that the numerics is well under control for that case. The expected branch cut opening at $x = 1.04$ GeV^2 was nicely reproduced.

4.5.4 Numerical results: Scaling propagator

The results of the F^2 correlator using scaling propagators as an input are shown in Figures 4.21 and 4.22.

The discontinuity of the branch cut gives rise to a positive definite spectral density, see Figure 4.23.

4.5.5 Conclusions

As a non-trivial application of the numerical technique developed in Appendix F and Section 4.2 we studied the analytic structure of an operator corresponding to the correlator of two Yang-Mills field strength squares in four Euclidean dimensions at the Born level. Expressing the operator in terms of scalar gluonic input allowed us to investigate the analytic structure of this expression depending on the parametrization (fit) of the gluon propagator. We studied parametrizations of the 'decoupling' and 'scaling'

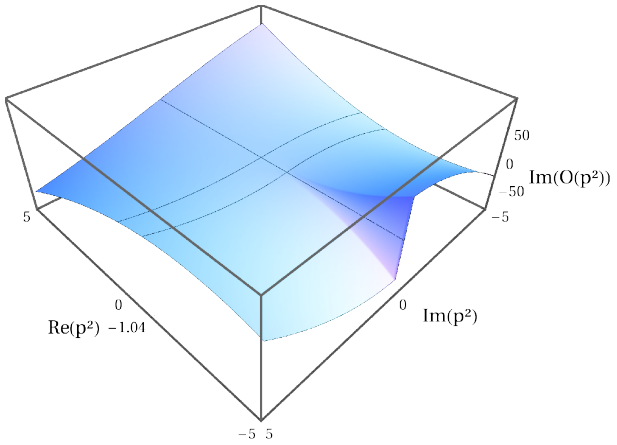

Figure 4.21: The imaginary part of the F^2 correlator with scaling propagators as input. As expected, a branch cut opens at $x = 1.04$ GeV^2.

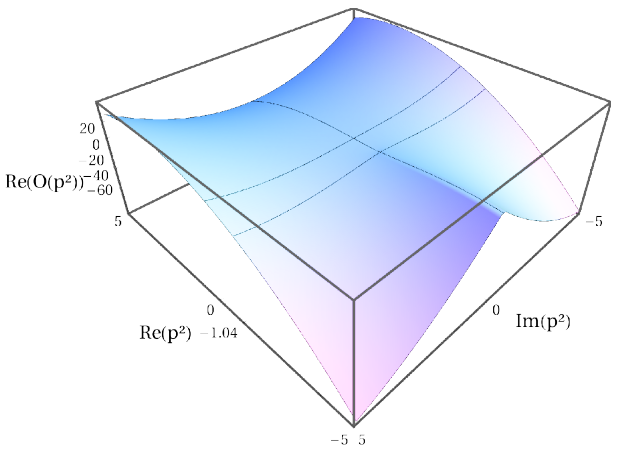

Figure 4.22: The real part of the F^2 correlator with scaling input.

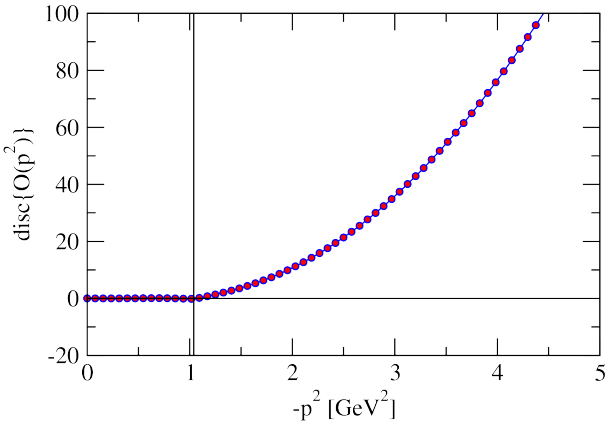

Figure 4.23: The discontinuity of the branch cut arising in the scaling case, leading to a positive definite spectral density.

type. The former leads to an analytic structure that features two unphysical branch cuts in addition to one that can be considered being physical, while in the latter case only a physical branch cut remains. There are no poles signaling the glueball mass, as we are operating solely at the Born level. In both cases we used positivity violating gluon input, which spoils a probabilistic interpretation and can be understood as an indication for the absence of these two-point functions from the asymptotic state space. After convolving the gluon input to calculate the F^2 correlator, we find physical cuts whose discontinuities give rise to positive definite spectral densities in both cases. The composite object respects positivity and is thus, at least by this simple argument, not removed from the physical subspace. Note that for the decoupling fit, two additional unphysical branch cuts are present[10]. Even though one might argue that these unphysical contributions might be canceled once higher order contributions are taken into account, it could still be interpreted as a shortcoming of the proposed fit form employed for this propagator. This statement is also supported by a recent study, where the analytic structure of the gluon propagator has been calculated non-perturbatively by solving the gluon DSE in the complex plane [54].

After a successful test (Section 4.2) and application (Section 4.3) of our method we are now ready to go one step further and extend the procedure such that it is suitable for non-perturbative investigations.

[10]See [100] for how to cure this issue.

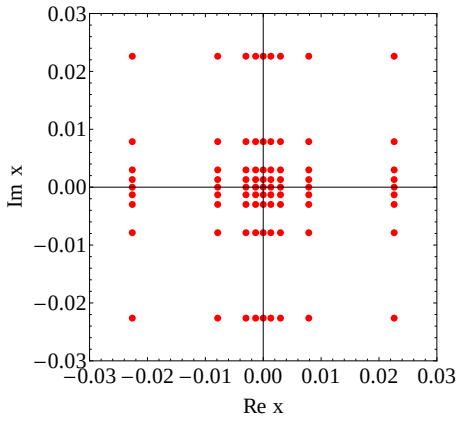

Figure 4.24: The discretized complex external momentum plane close to the origin.

4.6 The analytic structure of the quark propagator

4.6.1 The numerical method

As in the perturbative case, we have to discretize the plane of external complex momenta, which from now on will be referred to as the x-plane. In the perturbative case it was sufficient to restrict the calculation to complex momenta to the region of interest. For the DSE approach however, this does not apply anymore. Here we have to choose a mapping from the complex numbers to the discretized x-plane, $\mathbb{C} \to X$, in a way that allows for a high resolution in the infrared, while the node density in the ultraviolet is less important. A further constraint is, that the (discretized) real axis should be a subset of the discretized x-plane, including the origin[11]. In our setting, the grid is constructed such that it features a Gauss-Legendre node distribution[12] in real and imaginary direction. Figure 4.24 shows a closeup of the (logarithmically mapped) density of the external complex momentum nodes close to the origin. Note that the discretized real axis is a subset of the discrete x-plane.

The overall structure of the grid is shown in Figure 4.25.

As we will use Gauss-Legendre quadrature integrators to perform the

[11]We solve the real-axis DSE in a separate computation and compare it against the complex calculation. This provides at least some check for the numerics, as in the complex study the real axis solution is computed as any other point in the complex plane, involving the full machinery of deformations.

[12]See [90] for the Gauss-Chebyshev quadrature.

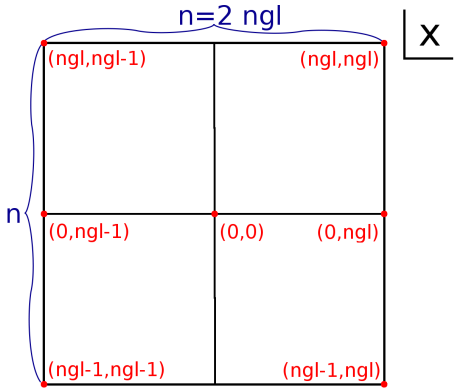

Figure 4.25: The discretized plane of complex external momenta, see text for explanation.

radial part of the integration, the grid features nodes corresponding to the roots of the Legendre polynomials on the interval $[0, \Lambda^2]$, where ngl nodes are used. The grid points are then remapped in a way to provide a better resolution of the infrared region. After generating the nodes on the real axis, the nodes are flipped and assigned to the negative real half axis. As we want the grid to feature an even number of nodes along its two dimensions, the grid ends one node below the cutoff at negative values. Then the same procedure is applied to the imaginary axis, where again the negative half-axis features one node less than the positive half axis. Thus we are left with a matrix $X \in \mathscr{M}(n \times n, \mathbb{C})$, $n = 2\ ngl$. This matrix provides the values of where A and B are to be evaluated. Thus, the dressing functions A and B are matrices in the same space, and the usual real-valued solutions $A(x \in \mathbb{R})$ and $B(x \in \mathbb{R})$ are contained within them. An absolutely crucial ingredient of the method is the way of interpolating the data. Here we perform a complex bi-cubic spline interpolation, see Section J.3 of Appendix J for details on our routine. Apart from the non-analytic points expected to show up in the solution, A and B are smooth functions. Using bi-cubic spline interpolation implements this information in our calculation. Test calculations showed that the level of resolution increases tremendously by using bi-cubic splines. With this technique we can deform the contours in the complex plane (and thus also in the matrices A and B), using a very high resolution along the radial integration contours.

The main problem in the non-perturbative case is, that the structure of the integrand changes throughout the iteration steps. To account for that, we start the iterations by guessing the deformation of the contours. Here the experience with the perturbative integrals is very helpful, as it allowed

us to gain some insight in the generic features of obstructive structures. A standard deformation would thus be to start integrating into the direction of $\arg(x)$, before closing the contour above (Quadrant I and II) or below (Quadrant III and IV). The occurrence of complex conjugate poles at some values x_0 ,$(\bar{x_0})$, can then be read off from the solution, as their position is indicated by numerical noise starting at angles equal or larger than $\arg(x_0)$. Additionally we take 'snapshots' of the y-plane every couple of iterations to check on the dynamically generated obstructive structures, re-adjusting the contours if necessary.

4.6.2 The truncated quark DSE

The ansatz for the inverse quark propagator is

$$S^{-1}(p) = -i\not{p}\, A\left(p^2\right) + B\left(p^2\right) \tag{4.21}$$

and the quark propagator becomes

$$S(p) = \frac{i\not{p}\, A(p^2) + B(p^2)}{p^2 A^2(p^2) + B^2(p^2)}. \tag{4.22}$$

The bare inverse quark propagator is

$$S_0^{-1}\left(p^2\right) = Z_2\left(-i\not{p} + Z_m m_0\right), \tag{4.23}$$

and the free Landau gauge gluon propagator reads

$$D_{free}^{\mu\nu}(p) = \frac{1}{p^2}\left(\delta^{\mu\nu} - \frac{p^\mu p^\nu}{p^2}\right). \tag{4.24}$$

The rainbow truncated quark propagator DSE is then given by

$$\begin{aligned} S^{-1}(p) = {} & S_0^{-1}(p) + Z_{1F} g^2 \frac{N_C^2 - 1}{2N_C} \int \frac{d^4q}{(2\pi)^4} \left[Z\left((p-q)^2\right)\right. \\ & \left. \times (p-q)^2 D_{free}^{\mu\nu}(p-q)\, \gamma^\mu S(q)\, \gamma^\nu\right], \end{aligned} \tag{4.25}$$

where we already dealt with the color space, and Z is the gluon dressing function. In order to solve the equation numerically, we have to isolate the quark propagator dressing functions A and B. As before, we apply (3.27) and (3.28) to both sides of equation (4.25). The traces are taken in Dirac space. The decoupled equations are then

$$
\begin{aligned}
A\left(p^2\right) &= Z_2 + \frac{Z_{1F} g^2}{p^2} \frac{N_C^2 - 1}{2N_C} \int \frac{d^4q}{(2\pi)^4} \left[\frac{Z\left((p-q)^2\right)}{(p-q)^2} \right. \\
&\times \frac{A(q^2)}{q^2 A^2(q^2) + B^2(q^2)} \left(\left(-2p^2 q^2 \right. \right. \\
&\left. \left. + p.q \left(p^2 + q^2\right) \right) + 2p.q \right) \Big] ,
\end{aligned} \tag{4.26}
$$

$$
\begin{aligned}
B\left(p^2\right) &= Z_2 Z_m m_0 + Z_{1F} g^2 \frac{N_C^2 - 1}{2N_C} \int \frac{d^4q}{(2\pi)^4} \left[\frac{Z\left((p-q)^2\right)}{(p-q)^2} \right. \\
&\times \left. \frac{3B(q^2)}{q^2 A^2(q^2) + B^2(q^2)} \right] .
\end{aligned} \tag{4.27}
$$

In order to get rid of the renormalization constants $Z_2$and Z_m we demand that the dressing functions A and B become one and m_0 at the renormalization point respectively. They can be subtracted in a straight forward way by employing a momentum subtraction (MOM) renormalization scheme, see Section 3.4. The functions A and B on the real axis serve as a check for the subsequent complex evaluation of the equations, where the real axis is a subset of the external grid and is treated in the same, more general way as all other complex values of the external momentum. In particular, a different integration grid is employed, as the integration contour is deformed in several steps and the integration boundaries are mapped to 0 and 1 respectively. Taking the quark-gluon vertex in the self-energy as a bare quantity alone is not sufficient to generate dynamical mass in the propagator. The Maris-Tandy [126] interaction we used in the beginning of this study,

$$
\begin{aligned}
Z_{1F}\ g^2 \frac{Z}{k^2} &= \frac{4\pi^2}{\omega^6} D k^2 e^{-\frac{k^2}{\omega^2}} \\
&+ 4\pi^2 \frac{\frac{12}{33 - 2N_f}}{\frac{1}{2} \ln \left[e^2 - 1 + \left(1 + \frac{k^2}{\Lambda_{QCD}^2} \right)^2 \right]} \mathscr{F}\left(k^2\right) ,
\end{aligned} \tag{4.28}
$$

with

$$
\mathscr{F}\left(k^2\right) = \frac{1}{k^2} \left(1 - e^{-\frac{k^2}{4m_t^2}} \right) ., \tag{4.29}
$$

with parameters $N_f = 4$, $\Lambda_{QCD}^{Nf=4} = 0.234$ GeV, $\omega = 0.3$ GeV, $D = 1.25$ GeV^2 and $m_t = 0.5$ GeV, turned out to be a rather complicated case to

start with. Thus we switched back to taking the vertex just bare, multiplied by some arbitrary constant to generate mass. One could also use a 1 BC construction[13], which we have on the agenda. However, in order to learn how to deal with the non-perturbative case, a constant times the tree-level structure is a reasonable setting.

4.6.3 Computational strategy

By now, we have fully developed the numerical framework to study the non-perturbative case with our method. The code is designed to run on hybrid clusters with CPUs and GPUs and features a coarse and a fine grained level of parallelization.

- *Coarse grained parallelization:* The strategy is to use as many Message Passing Interface (MPI) threads as GPUs are available on the cluster. Each MPI thread is assigned to a subset of the set of complex numbers contained in $X \in \mathscr{M}(n \times n, \mathbb{C})$, $n = 2\ ngl$. Each MPI thread claims one GPU that performs the fine grained parallelization.

- *Fine grained parallelization:* Each GPU operates on the subset of points contained in the partition that has been assigned to a particular MPI thread using CUDA Fortran [128]. Within this subset, each thread evaluates the DSE at a particular point, using an appropriate contour deformation. Once the results of all points are available they are broadcasted over the cluster using MPI. This step corresponds to one iteration of the system.

4.6.4 Conclusions

This project is still work in progress at the time of writing this thesis. However, we successfully constructed the whole numerical framework needed for this study and reduced the problem to a truncation that is suitable to refine and adjust our numerical procedure. We have found a promising strategy of how to cope with the dynamically generated obstructive structures in the complex plane of the radial integration variable, which is the main issue that has to be dealt with in such calculations.

[13] 1^{st} term of the Ball-Chiu vertex construction, [127].

Chapter 5

Color superconductivity in flavor asymmetric quark matter

5.1 Introduction

In the QCD phase diagram Figure 1.1 is a region marked as 'neutron stars', which is situated at the cold and intermediately dense regime[1]. This chapter is dedicated to study this region. Contrary to asymptotically high densities, where the coupling of QCD becomes weak, the intermediately dense regime features a strong coupling that does not allow for perturbative expansions. The phase structure in this regime can be explored employing Nambu–Jona-Lasinio (NJL) based approaches [129, 130, 131, 132], but there are also studies of this regime based on Dyson-Schwinger equations available[2], see e.g. [136, 137, 138, 139, 140, 141]. Our focus lies on color superconducting phases that might arise in this scenario, [142, 143, 144, 145, 132, 146, 147]. In particular, we are interested in the scenario where the chemical potential of the two species forming a Cooper pair are different–the case of asymmetric matter. It is convenient to introduce a common chemical potential $\bar{\mu} = \frac{1}{2}(\mu_1 + \mu_2)$ and a parameter for the separation of the Fermi spheres $\delta\mu = \frac{1}{2}(\mu_1 - \mu_2)\,,\ \mu_1 \geq \mu_2$, such that the individual chemical potentials can be written as $\mu_{1,2} = \bar{\mu} \pm \delta\mu$. This situation is a more realistic scenario than a system featuring a common chemical potential for all species and arises in a broad variety of systems, ranging from ultra-cold atoms to quark matter [148]. In the latter case, the asymmetry is induced by the strange quark mass and the requirement of beta equilibrium and charge neutrality as demanded for quark matter in a neutron star [149]. At vanishing separation, the Fermi seas coincide and

[1] See [22] for an introduction to dense matter in compact stars.

[2] For Dyson-Schwinger studies at lower densities see e.g. [133, 134, 135].

standard Bardeen-Cooper-Schrieffer (BCS) [150] pairing can occur. There, the constituents of the pair are arranged at antipodal points on the Fermi sphere, such that the pair has a vanishing net momentum. While in the original context of BCS the attractive interaction is phonon-mediated, in QCD one finds an attractive channel in the anti-symmetric anti-triplet[3] $\bar{\mathbf{3}}_A$ [142]. As the separation of the Fermi spheres grows large, the benefit from Cooper pair formation decreases. This is due to the fact that one can put a quark of the first species at its Fermi surface at zero costs in free energy, while one has to 'pay' the difference in free energy to bring the second constituent of the Cooper pair up to the position where it features a momentum that is equal in modulus but opposite in direction to the momentum of the first constituent. At some point the gain in energy due to condensation does not compensate the costs of pair formation and the ground state of the system goes from the BCS-like state back to the normal (unpaired) state. This transition has been predicted to be of first order [151, 152] by Chandrasekhar and Clogston. In the vicinity of the phase transition – the Chandrasekhar-Clogston limit (CCL)– however, the true ground state of the system might correspond to neither of these two possibilities, but to an inhomogeneous phase[4].

A first study concerning the physics of quark matter in this regime has been performed in [149]. They investigated the LOFF[5] phase [154, 155] in the context of quark matter. The LOFF phase, named after Larkin, Ovchinnikov, Fulde and Ferrell, is a particular type of an inhomogeneous phase that features a crystalline condensate. A LOFF-like phase for quark matter in a neutron star might provide an explanation of glitch phenomena[6] of neutron stars through the pinning of rotational vortices in the rigid structure of the crystalline condensate [143, 149, 146].

While the LOFF phase breaks rotational and translational invariance, another inhomogeneous phase has been proposed that breaks rotational, but maintains translational invariance, the Deformed Fermi Surface (DFS) phase, see [159, 160, 161, 162]. This sets the stage of our investigation[7]. This Chapter is organized as follows. In Section 5.2 we review the DFS phase in the

[3] $\mathbf{3}\otimes\mathbf{3} = \bar{\mathbf{3}}_A \oplus \mathbf{6}_S$, where the symmetric sextet channel features a (much weaker) induced pairing, see e.g. [146] and references therein.

[4] Here and in what follows we are interested in di-quark condensation only. However, one can also study chiral condensation in asymmetric systems, see [153] for a nice review on the subject.

[5] Sometimes also called FFLO phase in the literature (pronounce ['fʌfəloʊ]).

[6] A glitch is a sudden increase in the rotational frequency of a radio pulsar, see e.g. [156, 157, 158].

[7] I am very grateful to Mark Alford and Kai Schwenzer for introducing me to this exciting field of physics.

context of strongly interacting quark matter. In Section 5.3 we introduce the idea of four-fermion condensation in the context of quark matter with large flavor asymmetry, using exact renormalization group equations (ERGEs) to study a $SU(2)_f \times SU(2)_c$ toy model.

5.2 The Deformed Fermi Surface phase

The idea behind the Deformed Fermi Surface (DFS) phase [159, 160, 161, 162] is, that the system spontaneously chooses a direction along which it breaks rotational invariance by deforming the Fermi spheres. Starting from the spherical case, the Fermi surfaces of the fermionic species (e.g. up and down quarks) are deformed to an ellipsoidal shape such that the Fermi surfaces are close to each other in a certain region. This is achieved by deforming one Fermi sphere to an oblate, the other sphere to a prolate form, see Figures 5.1 and 5.2. Following the procedure as described in [159], the chemical potentials $\mu_{f=u,d}$ are deformed according to the prescription

$$\mu_f = \bar{\mu_f}\left(1 + (\varepsilon_S \pm \varepsilon_A)\sin^2\vartheta\right), \tag{5.1}$$

where the upper sign goes with u and the lower sine with the d quarks[8]. Equation (5.1) corresponds to an expansion of the spherical Fermi sea in Legendre polynomials, where only the 0^{th} and the 2^{nd} order polynomial have been taken into account,

$$\mu_f = \sum_{l=0}^{\infty} \mu_{f,l} P_l(\cos\vartheta) \approx \mu_{f,0} + \mu_{f,2}\frac{1}{2}\left(3\cos^2\vartheta - 1\right), \tag{5.2}$$

and where we defined

$$\bar{\mu_f} = \mu_{f,0} - \frac{1}{2}\mu_{f,2} \tag{5.3}$$

and

$$\varepsilon_{S/A} = \frac{3}{4}\left(\frac{\mu_{2d}}{\bar{\mu}_d} \pm \frac{\mu_{2u}}{\bar{\mu}_u}\right). \tag{5.4}$$

In Appendix H we show that these definitions lead to consistent equations. We furthermore detail the calculation in this and in the following section.

[8]Note that in [159] a cosine appears instead of the sine given in equation (5.1). Also they used the opposite sign convention for up and down quarks, which is why we give a redefinition of $\varepsilon_{S/A}$ below.

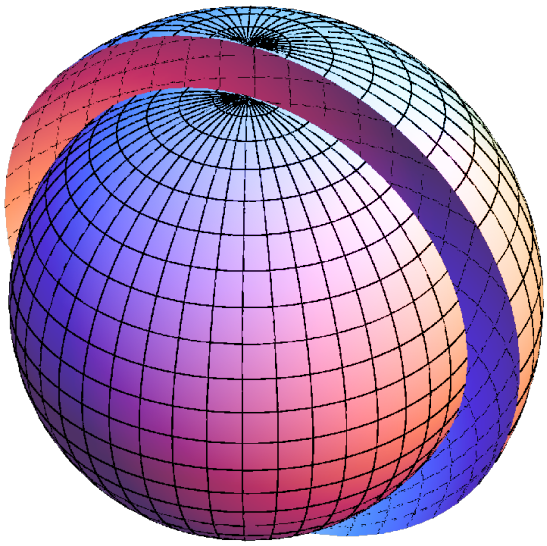

Figure 5.1: The larger d-quark and the smaller up-quark Fermi surfaces prior to deformation.

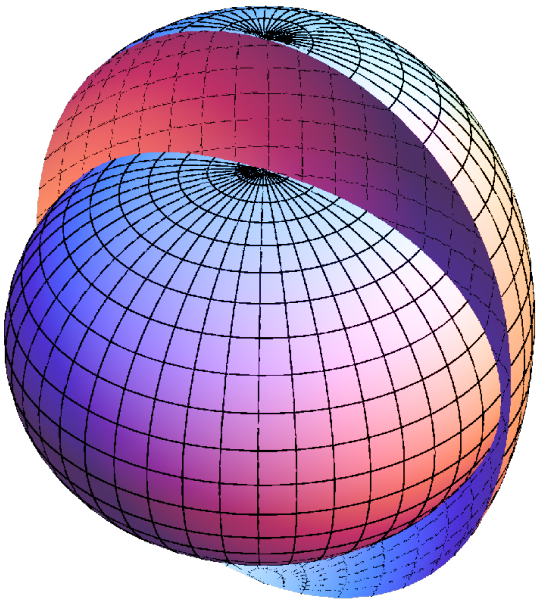

Figure 5.2: Deforming by means of equation (5.1) brings the Fermi surfaces close to each other in a certain region. Note that only proper normalization ensures conservation of the particle densities.

Note that the Fermi surfaces are not really deformed, but their shape is modified by removing and adding particles. There are four parameters controlling the process, $\bar{\mu}_u$, $\bar{\mu}_d$, ε_S and ε_A. In [160], the authors present a comparison of the LOFF phase and the DFS phase for isospin asymmetric nuclear matter. Letting LOFF and DFS compete with each other they find LOFF to correspond to a local minimum, while the state with the lowest free energy is DFS-like. This raises the question whether the state with lowest free energy is LOFF or DFS-like in flavor asymmetric quark matter around the Chandrasekhar–Clogston limit.

5.2.1 Estimate of the DFS free energy

In this Section we provide a very crude estimate of the free energy of a DFS state in flavor asymmetric quark matter. In a full-fledged calculation the system would adjust its deformation in a self-consistent way, however, here we assume that there is an optimal deformation parameter that provides the biggest gain in pairing at a minimum of deformation costs[9]. The aim is, to provide a parametric expression for the difference in free energy between the DFS state and the unpaired state in terms of the quantities of the average chemical potential, the gap and the separation of the Fermi surfaces. Equation (84) in [143] provides such an expression for the 2-flavor superconducting (2SC) phase. It is convenient to switch to an ellipsoidal coordinate system that suits this particular type of deformation,

$$\begin{aligned} \vec{r} &= \begin{pmatrix} \mu_f(\sin\vartheta)\sin\vartheta\cos\varphi \\ \mu_f(\sin\vartheta)\sin\vartheta\sin\varphi \\ \mu_f(\sin\vartheta)\cos\vartheta \end{pmatrix} \\ &= \begin{pmatrix} \bar{\mu_f}\left(1+(\varepsilon_S\pm\varepsilon_A)\sin^2\vartheta\right)\sin\vartheta\cos\varphi \\ \bar{\mu_f}\left(1+(\varepsilon_S\pm\varepsilon_A)\sin^2\vartheta\right)\sin\vartheta\sin\varphi \\ \bar{\mu_f}\left(1+(\varepsilon_S\pm\varepsilon_A)\sin^2\vartheta\right)\cos\vartheta \end{pmatrix}, \end{aligned} \tag{5.5}$$

where ϑ and φ are the usual spherical angles. Treating the u and d quarks as massless, the Jacobian can be written as

$$\begin{aligned} det\,(J)_f &= \frac{1}{8}k_f^2\,(2+(\varepsilon_S\pm\varepsilon_A) \\ &\quad\times -(\varepsilon_S\pm\varepsilon_A)\cos 2\vartheta)^3\sin\vartheta \\ &= k_f^2\left(1+(\varepsilon_S\pm\varepsilon_A)\sin^2\vartheta\right)^3\sin\vartheta. \end{aligned} \tag{5.6}$$

[9]This is of course a very rough estimate, but we are only interested in how the free energy of the system scales parametrically.

As in [161], we will not establish beta equilibrium or charge neutrality, but we will proceed in such a way that the baryon density is kept constant throughout the deformation process. In order to do this, we need the particle number density of the ellipsoidal Fermi seas. We thus have

$$\begin{aligned} n_f &= C \int_V \frac{d^3k_f}{(2\pi)^3} \\ &= \frac{C}{(2\pi)^3} \int_0^{k_{F,f}} dk_f \int_0^{\pi} d\vartheta \\ &\quad \times \int_0^{2\pi} d\varphi k_f^2 \left(1 + (\varepsilon_S \pm \varepsilon_A) \sin^2\vartheta\right)^3 \sin\vartheta, \end{aligned} \tag{5.7}$$

with C a general factor dealing with degeneracy (spin degree of freedom). Solving this expression (see Apendix H), we find

$$\begin{aligned} n_f &= \frac{C\ k_{F,f}^3}{6\pi^2} \left[1 + 2(\varepsilon_S \pm \varepsilon_A)\right. \\ &\quad \left. + \frac{8}{5}(\varepsilon_S \pm \varepsilon_A)^2 + \frac{16}{35}(\varepsilon_S \pm \varepsilon_A)^3\right]. \end{aligned} \tag{5.8}$$

This result can be used to readjust the deformation such that the particle density is preserved. The normalized parameter $k_{F,f}$ (and $\bar{\mu}_f$ in equation (5.1) respectively) depends on the momentum $k_{F,f}^{sph.}$ of the undeformed spherical case,

$$\begin{aligned} \frac{4\pi\ \left(k_{F,f}^{sph.}\right)^3}{3} &\stackrel{!}{=} \frac{4\pi\ k_{F,f}^3}{3} \left[1 + 2(\varepsilon_S \pm \varepsilon_A) + \frac{8}{5}(\varepsilon_S \pm \varepsilon_A)^2\right. \\ &\quad \left. + \frac{16}{35}(\varepsilon_S \pm \varepsilon_A)^3\right] \end{aligned} \tag{5.9}$$

$$\begin{aligned} \Rightarrow \quad k_{F,f} &= k_{F,f}^{sph.} \left[1 + 2(\varepsilon_S \pm \varepsilon_A) + \frac{8}{5}(\varepsilon_S \pm \varepsilon_A)^2\right. \\ &\quad \left. + \frac{16}{35}(\varepsilon_S \pm \varepsilon_A)^3\right]^{-1/3}. \end{aligned} \tag{5.10}$$

Now we have to evaluate the energy integrals for the deformed case. The calculation is again presented in Appendix H and yields the deformation

'costs' in terms of the energy density u,

$$\begin{aligned} u_{deform} &= \frac{C\ k_{F,u}^4}{8\pi^2}\left[1+\frac{8}{3}(\varepsilon_S+\varepsilon_A)+\frac{48}{15}(\varepsilon_S+\varepsilon_A)^2\right. \\ &\quad \left.+\frac{64}{35}(\varepsilon_S+\varepsilon_A)^3+\frac{128}{315}(\varepsilon_S+\varepsilon_A)^4\right] \\ &\quad -\frac{C\ \left(k_{F,u}^{sph.}\right)^4}{8\pi^2} \\ &+ \frac{C\ k_{F,d}^4}{8\pi^2}\left[1+\frac{8}{3}(\varepsilon_S-\varepsilon_A)+\frac{48}{15}(\varepsilon_S-\varepsilon_A)^2\right. \\ &\quad \left.+\frac{64}{35}(\varepsilon_S-\varepsilon_A)^3+\frac{128}{315}(\varepsilon_S-\varepsilon_A)^4\right] \\ &\quad -\frac{C\ \left(k_{F,u}^{sph.}\right)^4}{8\pi^2}. \end{aligned} \tag{5.11}$$

In this rough estimate we are only interested in an asymmetric deformation, i.e. $\varepsilon_s = 0$. Therefore an optimal ε_A can be determined which provides the best overlap of the two Fermi surfaces. For simplicity, the optimal choice of ε_A is obtained by demanding that the Fermi surfaces acquire the same value at a fixed inclination angle $\vartheta = \frac{\pi}{2}$. The optimal asymmetric deformation is then given by

$$k_{F,u}\left(1+\varepsilon_A^{opt}\right) \stackrel{!}{=} k_{F,d}\left(1-\varepsilon_A^{opt}\right) \tag{5.12}$$

$$\Rightarrow$$

$$\frac{k_{F,u}}{k_{F,d}}+\frac{k_{F,u}}{k_{F,d}}\varepsilon_A^{opt} = 1-\varepsilon_A^{opt} \tag{5.13}$$

$$\varepsilon_A^{opt} = \frac{1-\frac{k_{F,u}}{k_{F,d}}}{1+\frac{k_{F,u}}{k_{F,d}}} \tag{5.14}$$

$$\varepsilon_A^{opt} = \frac{k_{F,d}-k_{F,u}}{k_{F,d}+k_{F,u}} \tag{5.15}$$

$$\varepsilon_A^{opt} = \frac{\frac{1}{2}\left(\mu_d-\mu_u\right)}{\frac{1}{2}\left(\mu_d+\mu_u\right)} \equiv \frac{\delta\mu}{\mu}. \tag{5.16}$$

In order to establish a consistent choice of the parameters ε_A^{opt} and the properly normalized $k_{F,f}$, the system of equations (5.10) and (5.15) has to be solved in a closed form. This can be done numerically, however, as we

are interested in leading order effects only we will look into this matter analytically first[10]. The system has to be treated in a closed form, because ε_A^{opt} depends on the properly normalized momenta $k_{F,f}$, and the properly normalized momenta $k_{F,f}$ depend on the optimal deformation parameter, ε_A^{opt}. Thus we have to look at the condition for the optimal epsilon eq. (5.12) again and modify it by inserting the properly normalized $k_{F,f}$ eq. (5.10). We find an optimal ε_A^{opt} of

$$\varepsilon_A^{opt} \approx 3\frac{\delta\mu}{\mu}, \tag{5.17}$$

see Appendix H for the derivation. We assume that within a certain region of the deformed Fermi surfaces, BCS pairing is possible [11]. First, we consider shells of width 2Δ centered around each deformed Fermi surface, where $\Delta \approx \mathcal{O}(\delta\mu)$. The pairing region is then given by the overlap of the shells of the two Fermi seas, see Figure 5.3 for an explanation.

The resulting region where pairing is considered to occur is depicted in Figure 5.4.

The pairing region consists of two disjoint parts, one for hole-hole pairing below the up Fermi surface, and one for particle-particle pairing above the down Fermi surface. The regions are obtained by demanding that a point belonging to the region is either below/above the up/down Fermi surface, as well as within one Δ of the down/up Fermi surface. The regions can be parametrized as follows. Each region has two different ϑ-dependent boundaries for the radii $r_{i,j}$, where the first index i denotes whether the radius belongs to surface one or two, while the second index j labels the radius as inner or outer radius of that region. The radii are

$$\begin{aligned}
r_{11} &= \bar{\mu}_d \left(1 - \varepsilon_A \sin^2\vartheta\right) - \Delta, && (5.18)\\
r_{12} &= \bar{\mu}_u \left(1 + \varepsilon_A \sin^2\vartheta\right), && (5.19)\\
r_{21} &= \bar{\mu}_d \left(1 - \varepsilon_A \sin^2\vartheta\right), && (5.20)\\
r_{22} &= \bar{\mu}_u \left(1 + \varepsilon_A \sin^2\vartheta\right) + \Delta. && (5.21)
\end{aligned}$$

The first boundary value for the angle ϑ_{11} (where the first index again labels the surface while the second index labels the upper or lower value of the angle) are then obtained by solving

[10] In a numerical check we found agreement with our leading order result.

[11] Again we stress that the whole estimate is based on assuming a particular form of the optimal deformation parameter. Nevertheless our approach should be capable of capturing the parametrical behavior on a qualitative level.

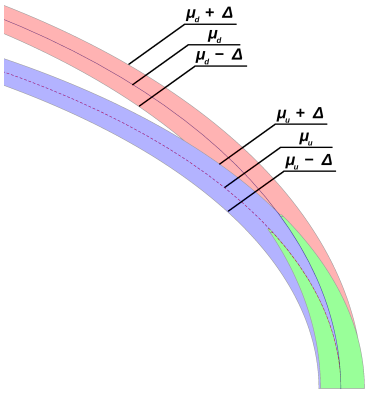

Figure 5.3: A part of the pairing region. To obtain this picture, we sliced the Fermi surfaces along the z and y axis and zoomed in to the region where the shells overlap. The dashed line is the Fermi surface of the up quarks, the thick solid line corresponds to the Fermi surface of the down quarks. Each surface serves as the center of a shell of width 2Δ. The region where BCS pairing is possible is the green area, which is the set of all points which are below the up Fermi surface but still within one Δ from the down Fermi surface, as well as the set of all points which are above the down Fermi surface and still within one Δ from the up Fermi surface. For this plot we used the following values for the undeformed Fermi seas: $\mu_d = 1$, $\mu_u = 0.95$, $\delta\mu$=0.025, Δ=0.025. The radii of the deformed Fermi surfaces, as well as the optimal asymmetric deformation parameter ε_A have been determined numerically and are in good agreement with the leading order calculation derived in the main text.

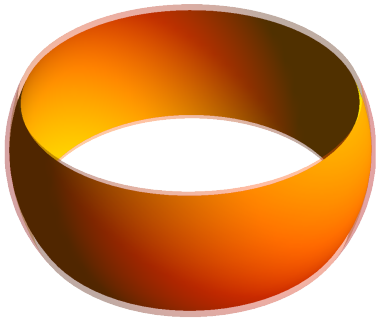

Figure 5.4: The three-dimensional region where pairing is considered to occur. The pairing region consists of the inner part (solid) and the outer part (opaque), which are disjoint. The structure of the pairing region is quite complicated. A section through the geometrical region is shown in Figure 5.5. For the calculation of the region we used the same parameters as in Figure 5.3.

$$\begin{aligned}
\bar{\mu}_d \left(1 - \varepsilon_A \sin^2 \vartheta_{11}\right) - \Delta &\stackrel{!}{=} \bar{\mu}_u \left(1 + \varepsilon_A \sin^2 \vartheta_{11}\right) && (5.22)\\
&\Rightarrow \\
\bar{\mu}_d - \Delta - \bar{\mu}_u &= \left(\bar{\mu}_u + \bar{\mu}_d\right) \varepsilon_A \sin^2 \vartheta_{11} && (5.23)\\
&\Rightarrow \\
\vartheta_{11} &= \arcsin \sqrt{\frac{\bar{\mu}_d - \bar{\mu}_u - \Delta}{\left(\bar{\mu}_u + \bar{\mu}_d\right) \varepsilon_A}} && (5.24)\\
&= \arcsin \sqrt{\frac{\delta\bar{\mu} - \frac{\Delta}{2}}{\varepsilon_A \bar{\mu}}}.
\end{aligned}$$

The second boundary, ϑ_{12}, follows immediately by symmetry, i.e.,

$$\vartheta_{12} = \pi - \vartheta_{11}. \tag{5.25}$$

Analogously we get for the first boundary value of the second surface

$$\begin{aligned}
\bar{\mu}_d \left(1 - \varepsilon_A \sin^2 \vartheta_{21}\right) &\stackrel{!}{=} \bar{\mu}_u \left(1 + \varepsilon_A \sin^2 \vartheta_{21}\right) + \Delta && (5.26)\\
&\Rightarrow \\
\bar{\mu}_d - \bar{\mu}_u - \Delta &= \left(\bar{\mu}_u + \bar{\mu}_d\right) \varepsilon_A \sin^2 \vartheta_{21} && (5.27)\\
&\Rightarrow \\
\vartheta_{21} &= \arcsin \sqrt{\frac{\bar{\mu}_d - \Delta - \bar{\mu}_u}{\left(\bar{\mu}_u + \bar{\mu}_d\right) \varepsilon_A}} && (5.28)\\
&= \arcsin \sqrt{\frac{\delta\bar{\mu} - \frac{\Delta}{2}}{\varepsilon_A \bar{\mu}}},
\end{aligned}$$

as well as

$$\vartheta_{22} = \pi - \vartheta_{21}. \tag{5.29}$$

The boundary angles are the same, so we can drop the region index for the angle,

$$\begin{aligned}
\vartheta_1 &= \arcsin \sqrt{\frac{\delta\bar{\mu} - \frac{\Delta}{2}}{\varepsilon_A \bar{\mu}}}, && (5.30)\\
\vartheta_2 &= \pi - \vartheta_1. && (5.31)
\end{aligned}$$

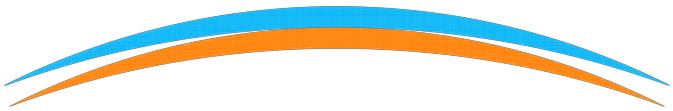

Figure 5.5: A section of the pairing regions we consider for our estimate. We assume that in the regions only either hole-hole pairing (lower region) or particle-particle pairing (upper region) is possible.

The cross section of the regions where both, hole-hole pairing and particle-particle pairing are possible are shown in Figure 5.5. This regions have to be integrated in order to estimate the gain due to Cooper pair condensation.

Assuming that pairing is possible in a shell of thickness 2Δ around the Fermi surface, we take a look at the standard BCS situation where the Fermi surfaces of the two species are level with each other. We thus have to integrate over the pairing regions, which we did by using Mathematica. We find that to leading order the benefit due to pairing in the DFS case is given by

$$\int_{pairing\ \ region} \Delta dA \quad \approx C \quad \frac{4}{3\pi^2}\sqrt{\frac{2}{3}}\bar{\mu}^2\Delta\delta\mu\sqrt{4+\frac{\Delta}{\delta\mu}},$$

which is parametrically of the same order as equation (84) in [143]. In this simple approximation one cannot find a parametrical suppression of this phase[12] as compared to others[13].

5.2.2 The stability of the DFS phase

In this section we provide a numerical stability check of the deformed phase. To this end we investigate the possibility of flavor-changing and non-flavor changing scattering processes numerically, taking energy and momentum conservation into account. We consider the following particular processes,

$$(k_F^u-\Delta)+\left(k_F^d-\Delta\right) \quad \rightarrow \quad (k_F^u+\Delta)+(k_F^s+\Delta)\,, \tag{5.32}$$
$$(k_F^u-\Delta)+(k_F^u-\Delta) \quad \rightarrow \quad (k_F^u+\Delta)+(k_F^u+\Delta)\,, \tag{5.33}$$
$$\left(k_F^d-\Delta\right)+\left(k_F^d-\Delta\right) \quad \rightarrow \quad \left(k_F^d+\Delta\right)+\left(k_F^d+\Delta\right)\,, \tag{5.34}$$
$$(k_F^u-\Delta)+\left(k_F^d-\Delta\right) \quad \rightarrow \quad (k_F^u+\Delta)+\left(k_F^d+\Delta\right)\,. \tag{5.35}$$

[12]First calculations of this kind with weak equilibrium and charge neutrality taken into account suggest that the overall behavior remains unchanged.

[13]We also investigated the breached-pairing phase [148] in a similar manner and found roughly the same parametrical behavior.

Hereby we make the simplified but conservative assumption that all species are gapped with Δ over their whole respective Fermi surfaces, thus these regions are not accessible for scattering processes[14]. We are looking for scattering processes where two filled particle states undergoing this process, both taken one Δ below their respective Fermi surfaces, scatter into two empty states just one Δ above their respective Fermi surface. States of width 2Δ around each Fermi surface are assumed to be blocked due to pairing. We find that all processes (5.32)-(5.35) can occur in this setting. This means that momenta can not only be exchanged by different species, but also among a single species. Examples of such processes are depicted in Figures 5.6, 5.7, 5.8 and 5.9.

From this very simplistic calculation we conclude that there are scattering processes that are out of detailed balance, as it is possible to scatter particles (even within one species) across the Fermi surfaces in the presence of the gap. In particular one can scatter into regions where no particles are present, as the system is not isotropic. Processes of that type cannot occur in reversed order, so they are leading to a violation of detailed balance. We conclude that due to this processes the system has the ability to re-arrange itself, and we deduce that the proposed ellipsoidal deformed surfaces will become unstable due to this freedom of re-arrangement. Then it is a natural question to ask where the system is driven to, but this is very hard to answer without having a numerical framework that computes the free energy of the deformed system while allowing for (arbitrary) deformations due to the scattering processes (5.32) - (5.35). However, providing at least an educated guess one might anticipate that the system acquires a form similar to the breached pairing (or interior gap binding) [148, 163] scenario, if not running into the LOFF or unpaired state.

5.2.3 Conclusions

We derived an estimate for the gain in free energy for the DFS phase by comparing the deformation costs in free energy with the pairing benefit due to some (assumed) pairing region. From this crude approximation one cannot draw a conclusion that shows whether DFS or 2SC is favored, as the net gain in free energy in both cases is parametrically of the same order. We then addressed the stability of the DFS phase by looking for momentum and energy preserving scattering processes that allow for a re-arrangement of the

[14]This assumption is very exaggerated, but also very generous in the sense that we consider a much larger region around the Fermi surfaces to be blocked than it would be the case for the real DFS state. This provides additional 'stability', as it is not possible to scatter into this region.

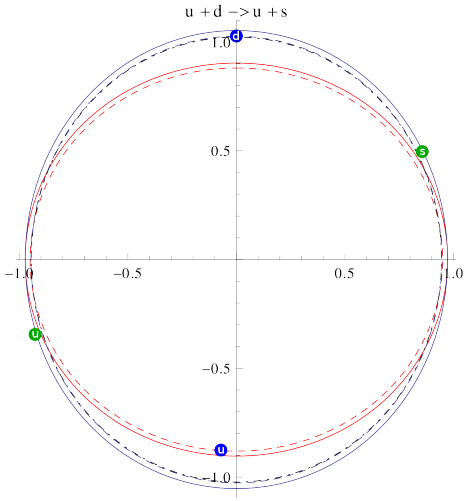

PARAMETER LIST	
μ–down spherical	1
μ–up spherical	0.95
μ–down normalized	1.0531
μ–up normalized	0.903501
strange mass	0.25
gap parameter Δ	0.025
$\delta\mu$ normalized	0.0747994
μ normalized	0.978301
ε optimal	0.0764585
CONSISTENCY CHECK	
energy balance	0.
momentum x–comp balance	-4.16334×10^{-16}
momentum y–comp balance	-5.55112×10^{-17}

Figure 5.6: This plot shows a (numerical) solution of a flavor-changing scattering process, (5.32), that gives rise to an instability of the ellipsoidal Fermi surfaces (see text). The outer solid line is the Fermi surface of the down quarks, the inner solid line the one of the up quarks. The dashed lines within the respective Fermi surfaces mark the depth of one Δ. Note that the Fermi surface of the strange quarks almost coincides with the one-Δ depth mark of the down Fermi surface. Starting form the 12-o'-clock position going clock wise, the dots mark the in-going down quark one Δ below its Fermi surface, the outgoing strange quark one Δ above its Fermi surface, the ingoing up quark one Δ below its Fermi surface, as well as the outgoing up quark one Δ above its Fermi surface. Ingoing particles are marked blue, outgoing particles are marked green, to provide some guidance for the eye. The parameters of this particular calculation are summarized in the table on the right.

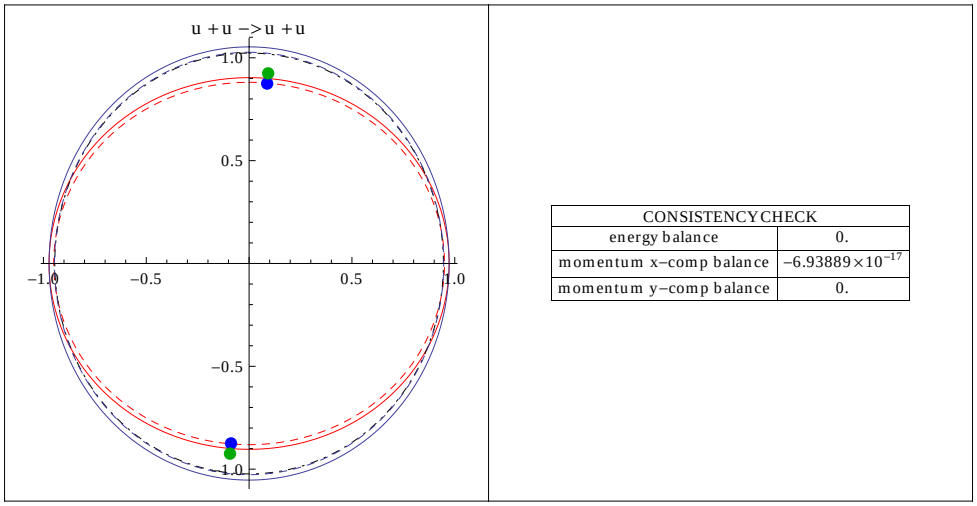

CONSISTENCY CHECK	
energy balance	0.
momentum x−comp balance	-6.93889×10^{-17}
momentum y−comp balance	0.

Figure 5.7: This plot shows a (numerical) solution of the scattering process eq. (5.33).

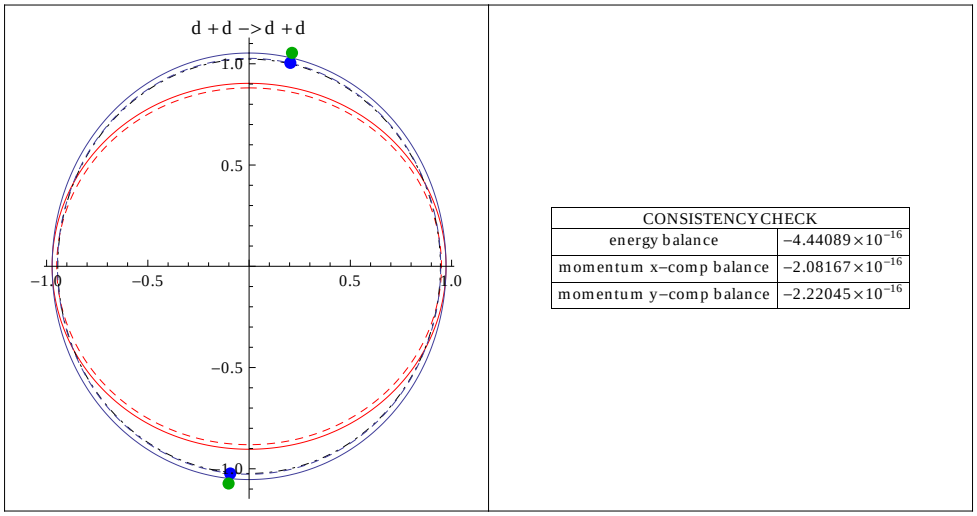

CONSISTENCY CHECK	
energy balance	-4.44089×10^{-16}
momentum x−comp balance	-2.08167×10^{-16}
momentum y−comp balance	-2.22045×10^{-16}

Figure 5.8: This plot shows a (numerical) solution of the scattering process eq. (5.34).

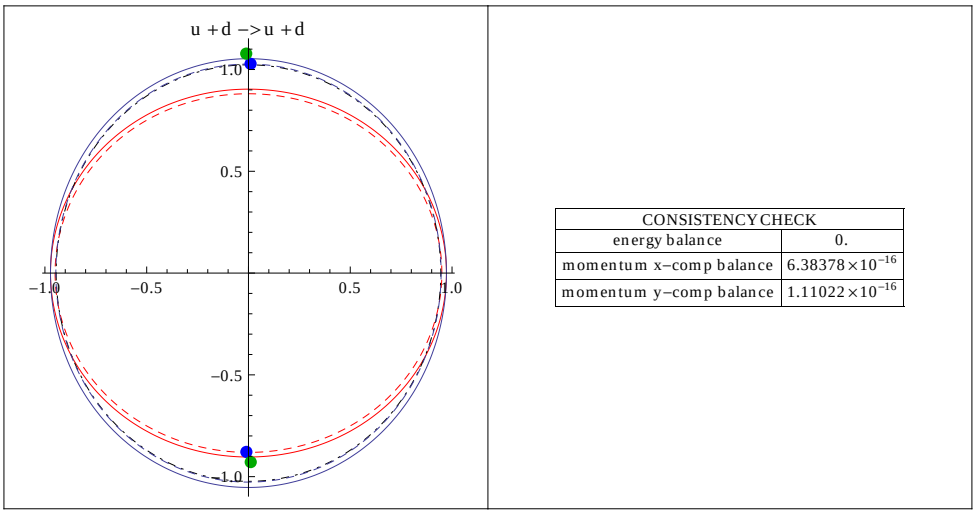

Figure 5.9: This plot shows a (numerical) solution of the scattering process eq. (5.35).

Fermi surfaces even in the presence of a gap. We found that such processes can indeed occur and conclude that the phase featuring ellipsoidal Fermi surfaces seems to be unstable.

5.3 Cooper Quartetting

When considering Cooper pair formation from a renormalization group point of view (see e.g. [164, 165, 166]), one finds that the operator corresponding to the two-fermion condensate is a marginal operator due to the kinematic restriction of the Cooper pair constituents having momenta which are equal in modulus and opposite in direction. Its coupling grows strong once the relevant scale – the distance to the Fermi surface – is driven towards zero. This corresponds to the picture of Cooper pairing formulated in the elegant language of the renormalization group. As we are considering systems of asymmetric quark matter here, the kinematical requirement directly affects the possibility of pair formation, as in a system with differing chemical potentials our original argument of costs and gain through pairing as presented in Section 5.1 applies. There are at least two possible ways out of this dilemma. On the one hand, one can give up on the idea of translational invariance by allowing the Cooper pairs to carry some net momentum (LOFF-phase). On the other hand, however, one can loosen the kinematic restriction by taking

two more fermions, considering quartetting rather than pairing[15]. There are many ways to arrange four momenta around the Fermi spheres such that the overall momentum vanishes, even if the difference of the Fermi surfaces is large. This is the idea of Cooper quartetting[16] for strongly coupled quark matter we investigate further in this chapter[17].

Clearly, the operator corresponding to a four fermion condensate is irrelevant, and no kinematical constraint will render it marginal. In a weakly coupled system we thus do not expect the four fermion condensate to play any role. However, dealing with QCD in a strongly coupled regime with two-particle condensation being suppressed opens the possibility that the four-fermion condensate might become a viable candidate. In the following we present this idea in more detail and investigate this possibility in a toy model.

5.3.1 A toy model

Our strategy is to use a spin-$\frac{1}{2}$ toy model with two flavors. Taking $SU(2)_s \times SU(2)_f$ as a toy model with a very particular eight-fermion interaction that allows for bosonization through sequentially performed Hubbard-Stratonovich transformations. Taking gauge interactions into account complicates the search for a viable condensate[18] considerably, so we are after a proof-of-principle calculation in this first exploratory study. The Lagrangian of our toy model is given by

$$\begin{aligned} \mathscr{L} &= \bar{\psi}^{\alpha}_{A}\left(\not{\partial}_{\mu} - (\mu + \delta\mu\sigma_3)\gamma^4 + m\right)^{\alpha\beta}_{AB}\psi^{\beta}_{B} \\ &\quad -g_4\left(\psi^{\alpha}_{A}\psi^{\beta}_{B}T^{\alpha\beta\gamma\delta}_{ABCD}\psi^{\gamma}_{C}\psi^{\delta}_{D}\right)\left(\bar{\psi}^{\epsilon}_{E}\bar{\psi}^{\eta}_{F}T^{\epsilon\eta\theta\zeta\dagger}_{EFGH}\bar{\psi}^{\theta}_{G}\bar{\psi}^{\zeta}_{H}\right) \end{aligned} \tag{5.36}$$

where greek indices label spin and latin indices label flavor. The tensor $T^{\alpha\beta\gamma\delta}_{ABCD}$ represents the four fermion interaction in our model and is given by

$$T^{\alpha\beta\gamma\delta}_{ABCD} = \varepsilon_{rstu}c^{r}_{A\alpha}c^{s}_{B\beta}c^{t}_{C\gamma}c^{u}_{D\delta}. \tag{5.37}$$

The quantities $c^{r}_{A\alpha}$ are tensor products of unit vectors in spin- and flavor-space, responsible for arranging the fermions in such a way that the overall

[15] In principle one could also consider three quarks, however, we are interested in the spin singlet case only.

[16] I am grateful to Mark Alford for suggesting this possibility.

[17] For a study of four fermion condensation in the context of homogeneous nuclear matter see [167].

[18] I want to thank Krishna Rajagopal for suggesting candidates for more realistic condensates.

wave function of the condensate is totally antisymmetric with respect to its indices, and ε_{rstu} is the 4-dimensional Levi-Civita tensor. Having the Lagrangian (5.36) at hand we will proceed by bosonizing the theory in two steps.

5.3.2 Bosonization of the toy model

With the first Hubbard-Stratonovich transformation we identify

$$\begin{aligned} & \exp\left\{\int d^4x\ g_4\left(\psi_i\psi_j T_{ijkl}\psi_k\psi_l\right)\left(\bar{\psi}_m\bar{\psi}_n T^{\dagger}_{mnop}\bar{\psi}_o\bar{\psi}_p\right)\right\} \\ \propto & \int \mathscr{D}\left[\Xi\right]\exp\left\{-\int dx\frac{m_\Xi^2}{2}|\Xi|^2\right\} \\ & \times\exp\left\{-\int d^4x\frac{g_4^Y}{2}\Xi^*\psi_i\psi_j T_{ijkl}\psi_k\psi_l\right\} \\ & \times\exp\left\{-\int d^4x\frac{g_4^Y}{2}\Xi\bar{\psi}_m\bar{\psi}_n T^{\dagger}_{mnop}\bar{\psi}_o\bar{\psi}_p\right\}. \end{aligned} \tag{5.38}$$

Up to this point, the path integral becomes

$$\begin{aligned} Z = & \int \mathscr{D}\left[\bar{\psi}\right]\mathscr{D}\left[\psi\right]\mathscr{D}\left[\Xi\right] \\ & \times\exp\left\{-\int d^4x\left(\mathscr{L}_{free}+\mathscr{L}_{gauge}\right)\right\} \\ & \times\exp\left\{-\int d^4x\frac{m_\Xi^2}{2}|\Xi|^2\right\} \\ & \times\exp\left\{-\int d^4x\frac{g_4^Y}{2}\Xi^*\psi_i\psi_j T_{ijkl}\psi_k\psi_l\right\} \\ & \times\exp\left\{-\int d^4x\frac{g_4^Y}{2}\Xi\bar{\psi}_m\bar{\psi}_n T^{\dagger}_{mnop}\bar{\psi}_o\bar{\psi}_p\right\}. \end{aligned} \tag{5.39}$$

Now we have to bosonize once more. In order to do so, the exponents of the exponentials have to be written in a bi-linear form with a real symmetric non-singular matrix connecting the fields, otherwise the integral would not be of the Gaussian type. In Appendix I we show that the four fermion interaction terms of equation (5.39) can indeed be brought to the desired

form. We can thus proceed by writing

$$\begin{aligned} & \exp\left\{\int d^4x\ \frac{\left(-g_4^Y\right)}{2}\left(\sqrt{\Xi^*}\right)^2\psi_i\psi_j T_{ijkl}\psi_k\psi_l\right\} \\ \propto\ & \int \mathscr{D}\left[\Theta\right]\exp\left\{-\int d^4x\frac{m_\Theta^2}{4}\Theta_{ij}T_{ijkl}\Theta_{kl}\right\} \\ & \times\exp\left\{\int d^4x\frac{g_\Theta^Y}{2}\sqrt{\Xi^*}T_{ijkl}\Theta_{ij}\psi_k\psi_l\right\}, \end{aligned} \tag{5.40}$$

where the couplings are related by

$$g_4^Y \stackrel{!}{=} \frac{\left(g_\Theta^Y\right)^2}{2m^2}. \tag{5.41}$$

In equation (5.40) we used the freedom to choose the relative sign in the binomial of the completed square of the Gaussian integral in order to produce a real-valued Yukawa coupling. Note further, that the fields Θ_{ij} are bosonic tensor fields with spinor indices. They do not carry baryon number and obey Fermi statistics, so they are ghost-like. Treating also the last term, we find

$$\begin{aligned} & \exp\left\{\int d^4x\ \frac{\left(-g_4^Y\right)}{2}\left(\sqrt{\Xi}\right)^2\bar{\psi}_m\bar{\psi}_n T^\dagger_{mnop}\bar{\psi}_o\bar{\psi}_p\right\} \\ \propto\ & \int \mathscr{D}\left[\Theta\right]\exp\left\{-\int d^4x\frac{m_\Theta^2}{4}\Theta^*_{ij}T^\dagger_{ijkl}\Theta^*_{kl}\right\} \\ & \times\exp\left\{\int d^4x\frac{g_\Theta^Y}{2}\sqrt{\Xi}T^\dagger_{ijkl}\Theta^*_{ij}\bar{\psi}_k\bar{\psi}_l\right\}, \end{aligned} \tag{5.42}$$

where the same relation for the coupling holds. The path integral of our theory after full bosonization becomes

$$
\begin{aligned}
Z &= \int \mathscr{D}\left[\bar{\psi}\right] \mathscr{D}\left[\psi\right] \mathscr{D}\left[\Xi\right] \mathscr{D}\left[\Theta_{mn}\right] \\
&\quad \exp\left\{ - \int d^4x \left(\mathscr{L}_{free} \right) \right\} \\
&\quad \times \exp\left\{ - \int d^4x \frac{m_\Xi^2}{2} |\Xi|^2 \right\} \\
&\quad \times \exp\left\{ - \int d^4x \frac{m_\Theta^2}{4} \Theta_{ij} T_{ijkl} \Theta_{kl} \right\} \\
&\quad \times \exp\left\{ \int d^4x \frac{g_\Theta^Y}{2} \sqrt{\Xi^*} T_{ijkl} \Theta_{ij} \psi_k \psi_l \right\} \\
&\quad \times \exp\left\{ - \int d^4x \frac{m_\Theta^2}{4} \Theta_{ij}^* T_{ijkl}^\dagger \Theta_{kl}^* \right\} \\
&\quad \times \exp\left\{ \int d^4x \frac{g_\Theta^Y}{2} \sqrt{\Xi} T_{ijkl}^\dagger \Theta_{ij}^* \bar{\psi}_k \bar{\psi}_l \right\} .
\end{aligned}
\tag{5.43}
$$

5.3.3 Towards the solution

Our intention is to study the possibility of the four-fermion condensation discussed above in the framework of exact renormalization group equations. Taking the bosonized theory (5.43) as a starting point, we write down an action that is appropriate for our study,

$$
\begin{aligned}
S &= \int d^4x \Big(\bar{\psi}_A^\alpha \left(\not{\partial}_\mu - \left(\mu + \delta\mu\sigma_3 \right) \gamma^4 + m \right)_{AB}^{\alpha\beta} \psi_B^\beta \\
&\quad + \frac{1}{2} \left(|\partial_\mu \Xi| \right)^2 + \frac{1}{2} \left(|\partial_\mu \Theta| \right)^2 \\
&\quad + \frac{m_\Theta^2}{2} \Theta_{AB}^{\alpha\beta} T_{ABCD}^{\alpha\beta\gamma\delta} \Theta_{CD}^{\gamma\delta} \\
&\quad - \frac{g_\Theta^Y}{2} \sqrt{\Xi^*} T_{EFGH}^{\epsilon\zeta\eta\theta} \Theta_{EF}^{\epsilon\zeta} \psi_G^\eta \psi_H^\theta \\
&\quad - \frac{g_\Theta^Y}{2} \sqrt{\Xi} T_{MNOP}^{\mu\nu\omega\rho} \Theta_{MN}^{\mu\nu} \bar{\psi}_O^\omega \bar{\psi}_P^\rho \\
&\quad + U\left(|\Xi| \right) + \tilde{g}_{IJKL}^{\iota\pi\tau\xi} \, |\Xi| \Theta_{IJ}^{\iota\pi} \Theta_{KL}^{\tau\xi} + m_\Theta \, |\Theta|^2 \Big) ,
\end{aligned}
\tag{5.44}
$$

It turned out to be sufficient to treat the Θ fields as real-valued. We furthermore add a term for the potential of the four-fermion condensate, as well as a vertex between two Θ-fields and a Ξ field. These terms are

allowed by symmetry and can be generated by the dynamics. They have to be included to allow for a formation of a four fermion condensate. The flow equation reads

$$\frac{\partial}{\partial k}\Gamma_k\left[\phi\right] = \frac{1}{2}\mathrm{Tr}\left\{\left[\Gamma_k^{(2)}\left[\phi\right]+R_k\right]^{-1}\frac{\partial}{\partial k}R_k\right\}, \tag{5.45}$$

with the regulators [69, 70]

$$R_k^{opt}\left(q^2\right) = Z_k\left(k^2-q^2\right)\Theta\left(k^2-q^2\right) \tag{5.46}$$

and

$$R_k^{f,opt}\left(q^2\right) = \not{q}\left(\sqrt{\frac{k^2}{q^2}}-1\right)\Theta\left(k^2-q^2\right) \tag{5.47}$$

for bosons and fermions respectively. Note that this system cannot be solved in a mean-field like approximation, as the two-fermion condensate does not acquire a non-zero expectation value in the regime we are interested in. In order to derive the flow equations we have to calculate

$$\left[\Gamma_k^{(2)}\left[\phi\right]+R_k\right]^{-1}\frac{\partial}{\partial k}R_k = M^{-1}\cdot\frac{\partial}{\partial k}R, \tag{5.48}$$

where $\Gamma_k^{(2)}$ is the second functional derivative with respect to the various fields. This yields a Hessian of the form

$$\mathscr{H} \sim \begin{array}{c|ccccc} & \psi & \bar{\psi} & \Xi & \Xi^* & \Theta \\ \hline \psi & \bullet & \bullet & 0 & 0 & 0 \\ \bar{\psi} & \bullet & \bullet & 0 & 0 & 0 \\ \Xi & 0 & 0 & \bullet & \bullet & \bullet \\ \Xi^* & 0 & 0 & \bullet & \bullet & \bullet \\ \Theta & 0 & 0 & \bullet & \bullet & \bullet \end{array}, \tag{5.49}$$

where the $\bullet$ stands for the non-vanishing entries to be derived below. In our truncation we thus exclude mixing among fermionic and bosonic fields, so they decouple and can be treated separately. Furthermore it turned out throughout the calculation that a $\sqrt{\Xi}$ -term always goes along with a $\sqrt{\Xi^*}$-term to form a modulus of Ξ, so we can also treat the Ξ-field as real-valued. The Hessian thus reduces to

$$\mathscr{H} \sim \begin{array}{c|cccc} & \psi & \bar{\psi} & \Xi & \Theta \\ \psi & \bullet & \bullet & 0 & 0 \\ \bar{\psi} & \bullet & \bullet & 0 & 0 \\ \Xi & 0 & 0 & \bullet & \bullet \\ \Theta & 0 & 0 & \bullet & \bullet \end{array} . \tag{5.50}$$

The fermionic block, for example, becomes

$$(M)_{11} = \frac{\delta^2 S}{\delta\psi_L^\lambda \delta\psi_K^\kappa}, \tag{5.51}$$

$$(M)_{12} = \frac{\delta^2 S}{\delta\bar{\psi}_L^\lambda \delta\psi_K^\kappa}, \tag{5.52}$$

$$(M)_{21} = \frac{\delta^2 S}{\delta\psi_L^\lambda \delta\bar{\psi}_K^\kappa}, \tag{5.53}$$

$$(M)_{22} = \frac{\delta^2 S}{\delta\bar{\psi}_L^\lambda \delta\bar{\psi}_K^\kappa}. \tag{5.54}$$

We are interested in the fermionic contribution to the coupling of the Θ-Θ-Ξ vertex, so let me briefly outline the procedure. In order to obtain the contribution, we have to perform functional derivatives with respect to Θ, Θ and Ξ, where we put all vacuum expectation values except the one for Ξ to zero in the end. Let us consider the derivative $\frac{\delta M^{-1}}{\delta\Theta\delta\Theta}$ first. The highest order of Θ appearing in M^{-1} is one, thus the second derivative with respect to Θ vanishes, such that we are left with

$$\begin{aligned} \frac{\delta^2 M}{\delta\Theta^{\chi\psi}_{ST}\delta\Theta^{\upsilon\phi}_{QR}} &= \\ &= M^{-1}\left(\frac{\delta M}{\delta\Theta^{\upsilon\phi}_{QR}}\right)M^{-1}\left(\frac{\delta M}{\delta\Theta^{\chi\psi}_{ST}}\right)M^{-1} \\ &+ M^{-1}\left(\frac{\delta M}{\delta\Theta^{\chi\psi}_{ST}}\right)M^{-1}\left(\frac{\delta M}{\delta\Theta^{\upsilon\phi}_{QR}}\right)M^{-1}, \end{aligned} \tag{5.55}$$

where we have exploited the fact that the derivative acting on the unit matrix vanishes to reshuffle the derivatives acting on an inverse matrix to act on non-inverted matrices only. The plan now is the following: first, we have to perform the derivatives as denoted in (5.55), then we will multiply the result with the field-independent off-diagonal regulator matrix R. The derivative with respect to Ξ will be performed afterwards. As we evaluate the

expression (5.55) at vanishing vacuum expectation values (except the one for Ξ), the matrix M^{-1} acquires an off-diagonal structure. This is because the Θ fields in the diagonal entries are set to 0, and only the (regulated) propagator terms in the off-diagonal entries remain. The matrices $\frac{\delta M}{\delta \Theta}$ acquire a diagonal form, as we will discuss now. The entries of the matrix M are of the form

$$M = \begin{pmatrix} A & S_1^{-1} \\ S_2^{-1} & B \end{pmatrix}, \tag{5.56}$$

which, upon matrix inversion turns into

$$\begin{aligned} M^{-1} &= \tfrac{1}{AB - S_1^{-1} S_2^{-1}} \begin{pmatrix} B & -S_1^{-1} \\ -S_2^{-1} & A \end{pmatrix}, \\ &= \Big| vev\ \Theta = 0 \Big| \\ &= \begin{pmatrix} 0 & S_2 \\ S_1 & 0 \end{pmatrix}, \end{aligned} \tag{5.57}$$

where the S_i correspond to the propagators. These terms are the only terms that survive, because the expressions for A and B contain one instance of Θ each, which we put to 0 as we evaluate the expression at its vacuum expectation value. Once the derivatives on M are performed, the off-diagonal structures of M equation (5.56) vanish, as they contain the propagator terms with no field content that might be hit by the derivatives. The overall structure is thus given by the matrix product

$$\begin{aligned} &\frac{\delta^2 M^{-1}}{\delta\Theta\delta\Theta} = \\ &= \begin{pmatrix} 0 & S_2 \\ S_1 & 0 \end{pmatrix} \cdot \begin{pmatrix} D_1 & 0 \\ 0 & E_1 \end{pmatrix} \cdot \begin{pmatrix} 0 & S_2 \\ S_1 & 0 \end{pmatrix} \cdot \\ &\quad \cdot \begin{pmatrix} D_2 & 0 \\ 0 & E_2 \end{pmatrix} \cdot \begin{pmatrix} 0 & S_2 \\ S_1 & 0 \end{pmatrix} \\ &+ \begin{pmatrix} 0 & S_2 \\ S_1 & 0 \end{pmatrix} \cdot \begin{pmatrix} D_2 & 0 \\ 0 & E_2 \end{pmatrix} \cdot \begin{pmatrix} 0 & S_2 \\ S_1 & 0 \end{pmatrix} \\ &\quad \cdot \begin{pmatrix} D_1 & 0 \\ 0 & E_1 \end{pmatrix} \cdot \begin{pmatrix} 0 & S_2 \\ S_1 & 0 \end{pmatrix} \\ &= \begin{pmatrix} 0 & S_2 E_1 S_1 D_2 S_2 \\ S_1 D_1 S_2 E_1 S_1 & 0 \end{pmatrix} \\ &\quad + \begin{pmatrix} 0 & S_2 E_2 S_1 D_1 S_2 \\ S_1 D_2 S_2 E_1 S_1 & 0 \end{pmatrix} \end{aligned} \tag{5.58}$$

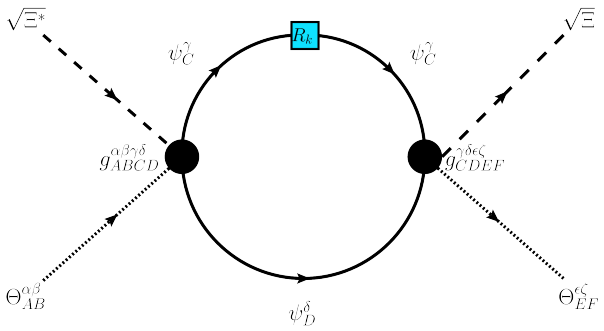

Figure 5.10: A sketch of the fermion loop that contributes to the coupling of two Θ-fields to the Ξ-field. This is just a sketch of the actual diagram, as in the derivation the square roots of Ξ and Ξ^* always go along to form a modulus of Ξ.

Hereby, S, D and E are the propagator as well as the functional derivative with respect to Θ on the upper and lower non-vanishing matrix entry respectively, the indices 1 and 2 refer to it being the derivative with respect to the first or the second Θ field in the term in the first line of equation (5.58). We will perform the derivative with respect to Ξ later. As a next step, we multiply the result of (5.58) with the off-diagonal regulator matrix R, which also has an additional sign because of the derivative,

$$\begin{aligned} &\left(\frac{\delta^2 M^{-1}}{\delta\Theta\delta\Theta}\right).\frac{\partial}{\partial k}R = \\ = &\begin{pmatrix} 0 & S_1 S_2^2 D_1 E_2 \\ S_1^2 S_2 D_2 E_1 & 0 \end{pmatrix}.\begin{pmatrix} 0 & \frac{\partial}{\partial k}R \\ \frac{\partial}{\partial k}R & 0 \end{pmatrix} \\ &= \frac{\partial}{\partial k}R\begin{pmatrix} S_1 S_2^2 D_1 E_2 & 0 \\ 0 & S_1^2 S_2 D_2 E_1 \end{pmatrix}. \end{aligned} \tag{5.59}$$

In order to obtain the flow equation one has to take the trace over all spaces, as well as the Matsubara sum, as we are working at non-vanishing temperature. From the fermionic block, we can thus derive a flow equation for the couplings $g^{\iota\pi\tau\xi}_{IJKL}$ by derivatives with respect to Θ, Θ and Ξ. This contribution is driven by a fermionic loop, see Figure 5.10 for a sketch.

Furthermore, we need a flow equation for the potential of Ξ, which receives contributions from the bosonic block only. The separately obtained equation for the coupling can then be plugged into the flow equation for the potential. We performed some preliminary calculations of the potential of Ξ, which indicate that condensation can indeed occur. The results are however too preliminary to be presented in this thesis.

5.3.4 Conclusions

In this study we investigate the possibility of four-fermion condensation in strongly coupled asymmetric matter. In our toy model we consider two flavors with spin. As a first step, we successfully bosonized the system. This step already turned out to be non-trivial, as we had to bring the four-fermion interactions arising from the first Hubbard-Stratonovich transformation to a form that allows for an application of further bosonization steps. We then provided a setting that is suitable for a treatment within the framework of renormalization group equations and presented a way of how the system can be solved.

Chapter 6

Conclusions and Outlook

The main subject of this thesis was to provide a full solution of the coupled system of the quark-gluon vertex and the quark propagator Dyson-Schwinger equation in the Landau gauge. We found a stable solution of the fully back-coupled system and compared the results of two independently implemented calculations. We have found perfect qualitative agreement in the behavior of all dressing functions. A subsequent qualitative analysis of the importance of the various tensor structures used to span the vertex revealed that two tensor structures can be neglected with almost no effect on the results. Another tensor structure can be removed while maintaining still good agreement with the full solution. The reduction of necessary components leads to a significant simplification of the system. There are many future task that can be addressed as a next step. Apart from investigating the possibility of a scaling solution, it would also be very interesting to study the effect of the three-gluon vertex on the quark-gluon vertex by solving them in a full self-consistent way. Also the inclusion of the abelian diagram that has been neglected in this first study would be a logical next step. One can also consider a reduced system and study the vertex for complex momenta or at non-vanishing temperature and/or density.

We furthermore started to investigate the analytic structure of the quark-propagator Dyson-Schwinger equation for arbitrary complex Euclidean momenta. In particular we are interested in a method that is capable of providing results in the deep time-like regime. We thus developed a novel numerical method to solve perturbative one-loop expressions for arbitrary Euclidean momenta. After a successful test of the method, we applied it to study a correlator of two Yang-Mills field-strength tensor squares at the Born level, using different gluonic input. We investigated two popular positivity violating gluon parametrizations and found that one leads to a positivity respecting analytic structure, while the other develops additional unphysical branch

cuts that spoil the validity of the parametrization. We then started to extend the method to apply it to the non-perturbative quark-propagator DSE. Having successfully constructed a numerical framework that allows for an adequate treatment of the equations we are very optimistic that first results will become available soon.

Another part of this thesis is dedicated to inhomogeneous phases in the context of strongly interacting flavor-asymmetric quark matter. We reviewed the Deformed Fermi surface phase and derived a parametrical expression for the benefit in free energy due to pairing in a rough approximation. We found that the DFS phase scales parametrically roughly like the LOFF phase, so the true ground state of the system cannot be determined from this naïve consideration. We then looked into scattering processes that are allowed by energy and momentum conservation in the DFS phase. We found that this phase might suffer from an instability induced by these scattering processes, as they allow for a rearrangement of the Fermi surfaces even in the presence of a gap.

Finally we looked into the possibility of four-quark condensation in the regime of large flavor asymmetry. In this regime, two-fermion condensation is suppressed. The hope is, that, while the two-quark condensate suppression results from a kinematic constraint imposed on the system, a four-quark condensate is not affected by this restriction and might become a viable candidate in this scenario. In the beginning it was unclear how one could study four fermion condensation in a reasonable approach. Now we have found and constructed a framework that allows us to study four-fermion condensation using ERGEs. To this end we constructed a toy model and successfully bosonized the corresponding eight-fermion interaction, by applying further Hubbard-Stratonovich transformations to deal with the resulting four-fermion interactions. We furthermore found a suitable truncation to employ ERGEs and we are now able to start employing them. The goal is to deliver a proof of principle that a phase with four-fermion condensation is possible in a strongly coupled system with large flavor-asymmetry.

Acknowledgements

Throughout the last years I met many people who contributed to this thesis in one way or another.

First of all I want to thank my advisor, Reinhard Alkofer, for offering so many interesting subjects to work on, for his continuous support and for many stimulating discussions.

I had the great pleasure to work with Mark Alford and Kai Schwenzer on very interesting problems throughout and beyond my stay at Washington University in Saint Louis. I highly enjoyed my time there, which was filled with most interesting discussions on many subjects.

I would like to thank Dirk Rischke for being an examiner of this work and for the hospitality, when I had the opportunity to visit Frankfurt.

Also for their hospitality, as well as for nice discussions I want to thank Will Detmold, Christian Fischer, Dirk Kreimer, Krishna Rajagopal, Adam Szczepaniak, Armen Sedrakian, Lorenz von Smekal and Dan Zwanziger.

Furthermore I am grateful to Gundolf Haase, Dalibor Kekez, Manfred Liebmann, Andreas Schmitt, Gernot Eichmann, Richard Williams, Markus Hopfer, Markus Q. Huber, Valentin Mader, Mario Mitter and Arno Tripolt for interesting discussions.

Finally I want to thank my friends and my family, in particular my wife Anita and our daughter Anna, as well as my parents for their continuous support. I also want to thank Helmut Gausterer and Natalia Alkofer for offering interesting topics for discussions, many of them related to non-relativistic velocities.

This work has been supported by the Doctoral Program "Hadrons in Vacuum, Nuclei and Stars", funded by the Austrian Science Fund, FWF, contract W1203-N16. I furthermore acknowledge support by the Research Core Area "Modeling and Simulation" of the University of Graz.

Appendix A

Conventions and notation

In this section we establish the notation and convention used throughout this thesis. Here and throughout this calculations we will use the standard representation for the Gamma matrices,

$$\gamma^k = \begin{pmatrix} 0 & -i\sigma^k \\ i\sigma^k & 0 \end{pmatrix}, \ \gamma^4 = \begin{pmatrix} \mathbb{1} & 0 \\ 0 & -\mathbb{1} \end{pmatrix}, \ \gamma^5 = \begin{pmatrix} 0 & \mathbb{1} \\ \mathbb{1} & 0 \end{pmatrix}, \tag{A.1}$$

with σ^k the Pauli matrices, such that

$$\gamma^\mu \ = \ (\gamma^\mu)^\dagger \,, \tag{A.2}$$

$$\gamma^5 \ = \ -\gamma^1\gamma^2\gamma^3\gamma^4, \tag{A.3}$$

and

$$\left(\gamma^1\right)^2 = \left(\gamma^2\right)^2 = \left(\gamma^3\right)^2 = \ \left(\gamma^4\right)^2 \ = \mathbb{1}. \tag{A.4}$$

Furthermore, the Clifford algebra

$$\{\gamma^\mu, \gamma^\nu\} = 2\delta^{\mu\nu} \tag{A.5}$$

is satisfied. The charge conjugation matrices are given by

$$C = \gamma^4\gamma^2, \quad C^T = C^\dagger = C^{-1} = -C. \tag{A.6}$$

As all investigations are performed in Euclidean space it is often convenient to express an integral over a four momentum k in hyper-spherical coordinates,

$$\begin{aligned}\int_{\mathbb{R}^4} d^4k \;&\rightarrow\; \int_0^{2\pi} d\phi \int_0^{\infty} dk\; k^3 \int_0^{\pi} d\theta_1 \sin^2\theta_1 \int_0^{\pi} d\theta_2 \sin\theta_2 \qquad \text{(A.7)}\\ &= \left| \begin{array}{c} y \equiv k^2 \rightarrow dy = 2kdk \\ \theta_1 \equiv \arccos z \rightarrow d\theta_1 = -\frac{dz}{\sqrt{1-z^2}} \\ \theta_2 \equiv \arccos w \rightarrow d\theta_2 = -\frac{dw}{\sqrt{1-w^2}} \end{array} \right| \\ &= \frac{1}{2}\int_0^{2\pi} d\phi \int_0^{\infty} dy\; y \int_{-1}^{1} dz\sqrt{1-z^2} \int_1^{1} dw.\end{aligned}$$

The definitions of the propagators and vertices needed for the quark-gluon vertex study are presented in Figures A.1 and A.2.

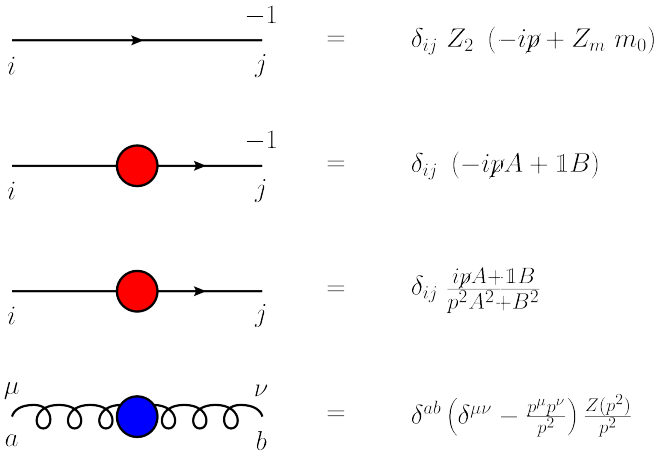

Figure A.1: The inverse bare, inverse dressed and dressed quark propagator, together with the gluon propagator.

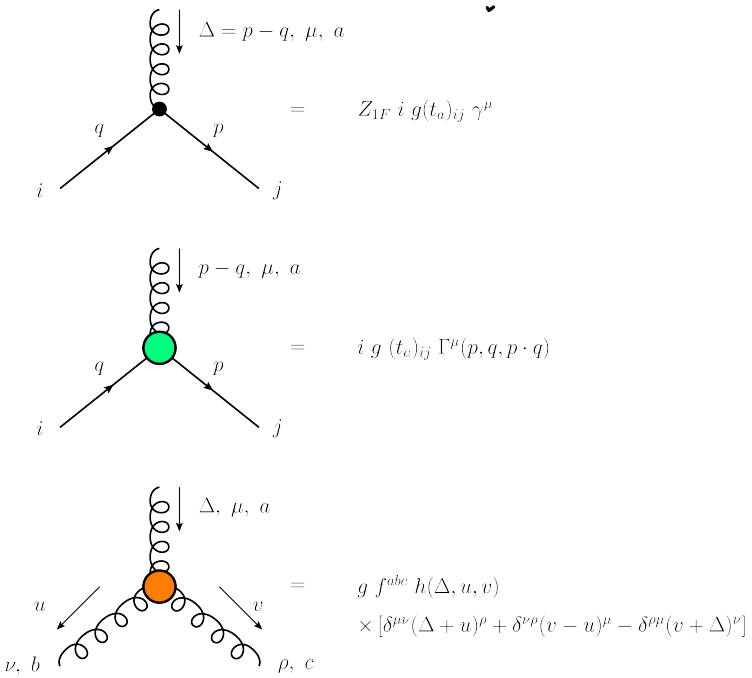

Figure A.2: The bare and dressed quark-gluon vertex and the model for the three-gluon vertex.

Appendix B

Solving the quark-gluon vertex DSE

In this Appendix we outline the steps that have to be performed to solve the coupled system of the quark-propagator and the quark-gluon vertex DSE.

B.1 Prerequisites

B.1.1 Coordinate frame and momentum routing

Contrary to the alternative approach discussed in Appendix C we use the quark momenta p^μ and q^μ explicitly here. The coordinates are chosen as shown in Figure B.1.

The momenta are routed such that a minimum effort on interpolation and extrapolation is necessary. This means in particular that we compute the vertex exactly as it is needed for the self-energy term of the quark propagator, see Figure B.2.

There are three momenta involved. According to our choice of coordinates they are

$$p = \begin{pmatrix} 0 \\ 0 \\ 0 \\ |p| \end{pmatrix}, \; q = \begin{pmatrix} 0 \\ 0 \\ |q|\sqrt{1-z_1^2} \\ |q| z_1 \end{pmatrix}, \tag{B.1}$$

$$w = \begin{pmatrix} 0 \\ |w|\sqrt{1-z_2^2}\sqrt{1-z_3^2} \\ |w|\sqrt{1-z_2^2} z_3 \\ |w| z_2 \end{pmatrix},$$

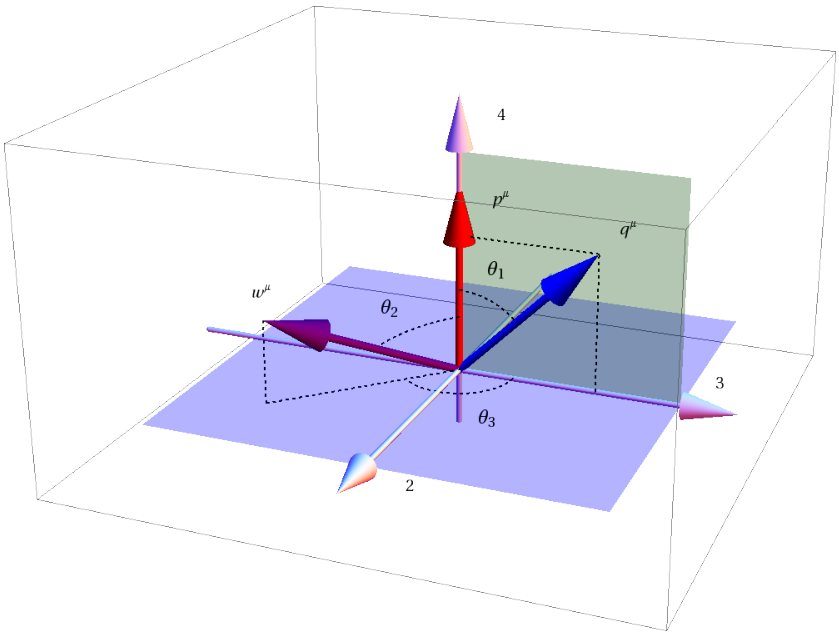

Figure B.1: The choice of coordinates.

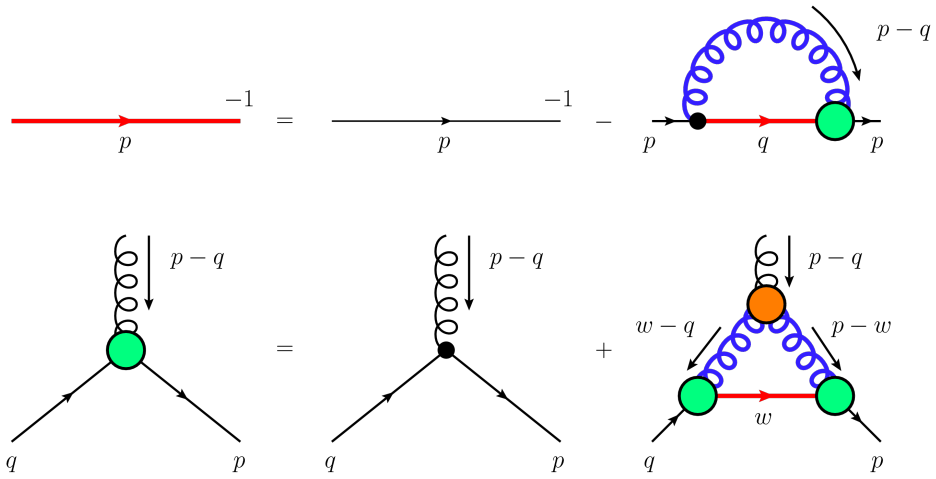

Figure B.2: Our choice of momentum routing .

where

$$z_i \;=\; \cos\theta_i,\; i \in \{1,2,3\}\,. \tag{B.2}$$

It is important to note the cosine of the angle between the momenta w and q is given by

$$\cos\angle_{w,q} \;=\; \sqrt{1-z_1^2}\sqrt{1-z_2^2}z_3 + z_1 z_2. \tag{B.3}$$

B.1.2 Expressing the basis elements

In the previous section we defined the momenta p, q and w. The vertex is computed for external momenta q and p, but is also needed for the momenta q and w (left vertex in the non-abelian diagram), as well as for the momenta w and p. For all these pairs of momenta we thus have to express the basis elements in terms of the Lorentz invariants $p^2,\ q^2,\ w^2,\ p\cdot q,\ p\cdot w$ and $q\cdot w$. For example, the normalized momentum d for the left quark-gluon vertex in the non-abelian diagram is given by (3.8)

$$\begin{aligned} d_l^\mu \;&=\; \frac{(w-q)^\mu}{||w^\mu - q^\mu||} = \frac{(w-q)^\mu}{\sqrt{q^2+w^2-2w\cdot q}} \\ &\overset{(B.3)}{=}\; \frac{(w-q)^\mu}{\sqrt{q^2+w^2-2\sqrt{w^2q^2}\left(\sqrt{1-z_1^2}\sqrt{1-z_2^2}z_3+z_1z_2\right)}}. \end{aligned} \tag{B.4}$$

The normalized vector s^μ for the left quark-gluon vertex in the non-abelian diagram is obtained by following the prescription of (3.9). The average quark momentum for the left vertex is

$$\Omega^\mu \;=\; \frac{1}{2}\left(q^\mu + w^\mu\right). \tag{B.5}$$

Taking the part that is transverse to the gluon momentum we have

$$\begin{aligned} & \left(\delta^{\mu\nu} - d^\mu d^\nu\right)\Omega^\nu \\ =\;& \Omega^\mu - d^\mu d\cdot\Omega \\ =\;& \frac{1}{2}\left(q^\mu + w^\mu\right) - \frac{1}{2}\frac{(w-q)^\mu\left(w^2-q^2\right)}{q^2+w^2-2w\cdot q}. \end{aligned} \tag{B.6}$$

This expression has to be normalized, so we take the square first, where we drop the factor of $\frac{1}{2}$ as it is canceled by the normalization anyway.

$$\begin{aligned} & \left((q^\mu + w^\mu) - \frac{(w-q)^\mu \left(w^2 - q^2\right)}{\left(q^2 + w^2 - 2w\cdot q\right)^2} \right)^2 \\ = \;& q^2 + w^2 + 2w\cdot q + \frac{\left(w^2-q^2\right)^2 \cancel{\left(w^\mu - q^\mu\right)^2}}{\left(w^\mu - q^\mu\right)^{\cancel{4}\;2}} \\ & -2\frac{\left(w^2-q^2\right)^2}{\left(w^\mu - q^\mu\right)^2} \\ = \;& q^2 + w^2 + 2w\cdot q - \frac{\left(w^2-q^2\right)^2}{\left(w^\mu - q^\mu\right)^2}, \end{aligned} \tag{B.7}$$

and we find that the vector s_l^μ is given by

$$\begin{aligned} s_l^\mu \;=\; & \frac{1}{\sqrt{q^2 + w^2 + 2w\cdot q - \frac{\left(w^2-q^2\right)^2}{q^2+w^2-2w\cdot q}}} \\ & \times \left((q^\mu + w^\mu) - \frac{(w-q)^\mu \left(w^2 - q^2\right)}{q^2 + w^2 - 2w\cdot q} \right), \end{aligned} \tag{B.8}$$

where $w \cdot q$ is

$$w\cdot q \;=\; \sqrt{w^2 q^2}\left(\sqrt{1-z_1^2}\sqrt{1-z_2^2}\, z_3 + z_1 z_2 \right). \tag{B.9}$$

Similar expressions have to be computed for the right quark-gluon vertex in the non-abelian diagram, as well as for the quark gluon vertex on the left hand side of the equation.

B.1.3 Color pre-factor of the vertex equation

The color factors of the vertex equation including the bare vertex and the non-abelian diagram on the right hand side become[1]

[1]The symbol $\overset{\circ}{=}$ is to remind the reader that this is not an equation, but just the left and right hand side in color space.

$$(t_a)_{ij} \overset{\circ}{=} (t_a)_{ij} + (t_m)_{ik}(t_l)_{k'j} f_{aml}\delta_{mm'}\delta_{ll'}\delta_{kk'} \tag{B.10}$$

$$(t_a)_{ij} \overset{\circ}{=} (t_a)_{ij} + \underbrace{(t_m)_{ik}(t_l)_{kj}}_{(t_m t_l)_{ij}} f_{aml} \tag{B.11}$$

$$(t_a)_{ij} \overset{\circ}{=} (t_a)_{ij} + (f_{aml} t_m t_l)_{ij} \tag{B.12}$$

$$\cancel{(t_a)_{ij}} \overset{\circ}{=} \cancel{(t_a)_{ij}} + \frac{iN_C}{2}\cancel{(t_a)_{ij}}, \tag{B.13}$$

thus only the non-abelian diagram obtains a non-trivial color factor of $\frac{i\ N_C}{2}$.

B.1.4 Reducing the number of terms

This step is crucial, as it reduces the number of terms, that have to be computed to obtain the vertex dressing functions, considerably. Here we particularly focus on the evaluation of the Lorentz contractions and Dirac traces using FORM [89]. In the non-abelian diagram we have three relative momenta, see Figure B.2. Even though these momenta have to be expressed in terms of the Lorentz invariants constructed from p, q and w, it is convenient to introduce the momenta

$$\Delta^\mu = p^\mu - q^\mu, \tag{B.14}$$

$$u^\mu = w^\mu - q^\mu, \tag{B.15}$$

$$v^\mu = p^\mu - w^\mu, \tag{B.16}$$

as in the definition depicted in Figure A.2. Apart from the pre-factors, the three-gluon vertex reads

$$\Gamma^{\mu\nu\rho}_{ggg} = \delta^{\mu\nu}(\Delta + u)^\rho + \delta^{\nu\rho}(v - u)^\mu - \delta^{\rho\mu}(v + \Delta)^\nu . \tag{B.17}$$

Exploiting transversality,

$$T^{\mu\nu}_x = \delta^{\mu\nu} - \frac{x^\mu x^\nu}{x^2}$$

for some momentum x, one can reduce (B.17) to

$$T^{\mu\mu'}_\Delta T^{\nu\nu'}_u T^{\rho\rho'}_v \Gamma^{\mu'\nu'\rho'}_{ggg} = 2\left(\delta^{\mu\nu}\Delta^\rho - \delta^{\nu\rho}u^\mu - \delta^{\rho\mu}\Delta^\nu\right), \tag{B.18}$$

where we used the projections

$$(\Delta + u)^{\rho'} = (p - 2q + w)^{\rho'}, \tag{B.19}$$
$$T_v^{\rho\rho'}\,(p - 2q + w - p + p)^{\rho'} = (2p - 2q)^{\rho} = 2\Delta^{\rho}, \tag{B.20}$$

and similarly

$$(v - u)^{\mu'} = (p - 2w + q)^{\mu'}, \tag{B.21}$$
$$T_\Delta^{\mu\mu'}\,(p - 2w + q - q + q)^{\mu'} = (2q - 2w)^{\mu} = -2u^{\mu}, \tag{B.22}$$

and

$$(v + \Delta)^{\nu'} = (2p - w - q)^{\nu'}, \tag{B.23}$$
$$T_u^{\nu\nu'}\,(2p - w - q - q + q)^{\nu'} = (2p - 2q)^{\nu} = 2\Delta^{\nu}. \tag{B.24}$$

The momenta Δ, u and v can then be expressed in terms of d, d_l and d_r, as they only differ by a normalization factor. This reduces the number of terms further, and one obtains scalar expressions with a reasonable number of terms. The orthonormality of the momenta s and d can be exploited for each set individually,

$$s \cdot s = d \cdot d = 1,\ s \cdot d = 0, \tag{B.25}$$
$$s_l \cdot s_l = d_l \cdot d_l = 1,\ s_l \cdot d_l = 0, \tag{B.26}$$
$$s_r \cdot s_r = d_r \cdot d_r = 1,\ s_r \cdot d_r = 0, \tag{B.27}$$

where the indices l and r label the left and right basis elements in the non-abelian diagram, and the momenta without a label belong to the outer basis. The output of FORM is processed using Linux shell-scripts together with `sed`-scripts. The shell-scripts manipulate the integration kernels in such a way that it can be interpreted by the compiler. This step is crucial, as it does not require any modifications of the output by hand, which would introduce a source of errors. The output is expressed in terms of scalar products among the momenta appearing in the diagrams. The scalar products were computed using Mathematica [168], where the output of Mathematica is also processed by the shell-script. The script merges the output of the two computer algebra systems and produces the compilable source code. This also allows for fast change of basis elements, as all necessary input is generated by just calling one script.

B.2 The structure of the program

In this section we give the details on how the system is solved. The structure of the program is shown in Figure B.3.

B.2.1 Initialization

In this section the grids are initialized as described in Section J.1 of Appendix J. The angular grid[2] is computed using Gauss-Chebyshev polynomials of the second kind. We employ the same grid for the angle θ_2 in equation (A.7) by modifying the weights for this angle accordingly. Using Gauss-Chebyshev quadrature for the angular integration proved to be very efficient[3]. The discrete solutions of the Yang-Mills system 3.2.1 are read and stored to an array, the second derivatives needed for the cubic spline interpolation are computed. The dressing functions of the quark propagator are initialized using the fit-functions (6.85) and (6.86) from [23]. All vertex dressing functions are initially zero, except the two structures of the outer basis that contribute to the tree-level structure, f_1 and f_6. They are put to $f_1 = \sqrt{2}$ and $f_6 = 1$ initially, such that $g_1 = 1$ after a change of basis has been performed. The parameters of the run are written to the standard stream and the system starts to iterate.

B.2.2 The iteration process

B.2.2.1 Vertex update

Each full iteration consists of two vertex iterations and as many propagator iterations as needed to achieve convergence. The two vertex updates are performed first. Equation (3.5) is evaluated for all eight dressings f_i, after each vertex iteration a change of basis is necessary to transfer the information from the f_i dressings of the outer basis to the g_i dressings of the inner basis. This step also involves spline interpolation as discussed in Section J.1, as the g_i dressings are tied to the internal grid, the f_i dressings to the external grid. For the first seven iterations we do not take the full information from the newly calculated vertex dressings, but only a certain percentage of the solution, where the complementary part that adds up to one is the fraction we take of the old solution from the previous update (or initialization if it

[2]We only use one angular grid for all angles arising throughout the calculation.

[3]We also used 12 angular nodes and found no significant deviation from the 8-node result. In principle one could also use sinh-tanh quadrature [170], but this rule is quite sensitive to the cut-off.

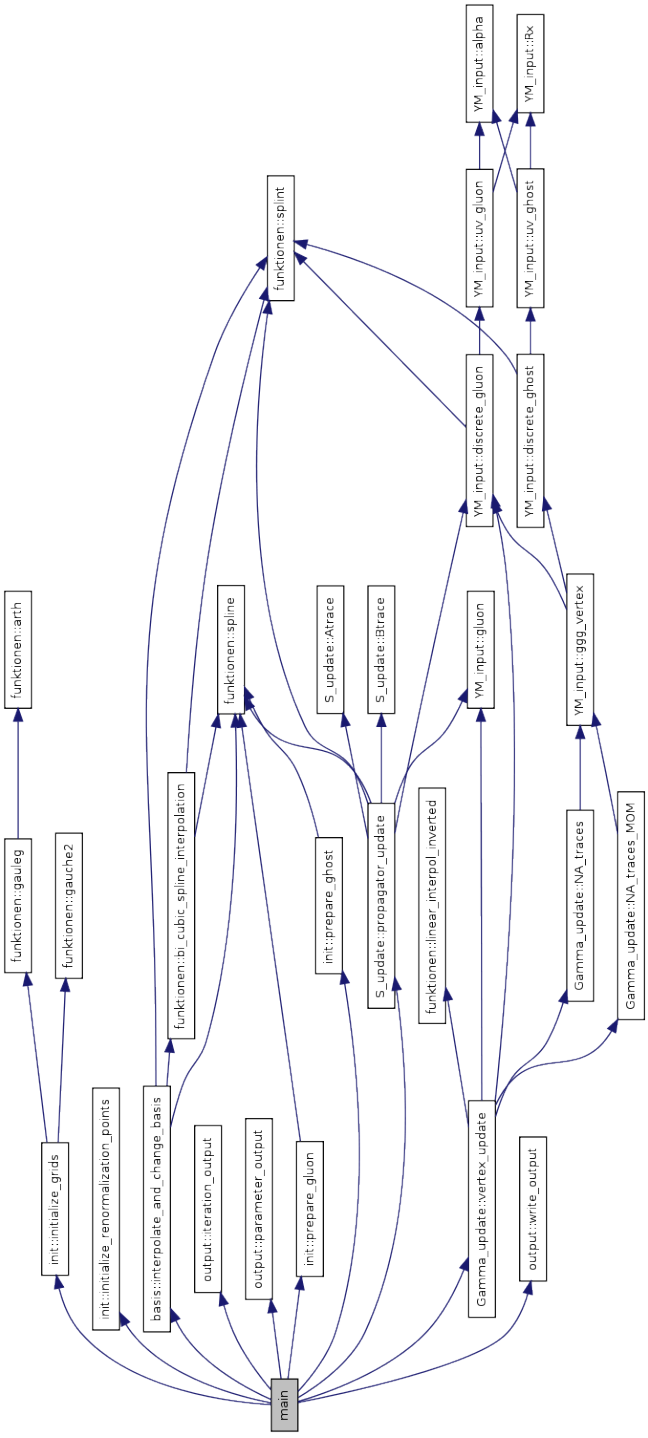

Figure B.3: The structure of the program. This plot has been generated automatically using doxygen [169].

is the first update). This stabilizes the first iterations and allows the system to adjust itself to the iteration. The ratio of the percentage of the old and new solution is gradually driven towards one, such that after 7 iterations[4] the system runs at full updates.

B.2.2.2 Propagator update

After two vertex updates, the propagator is iterated till it converges[5]. After each update of the propagator, the propagator dressings have to be spline interpolated again to transfer the information from the externally calculated propagator dressings A and B to the internally required fine grained dressing functions Ai an Bi. As in the vertex case, we switch on the iteration process gradually by taking more and more information from the newly updated dressing functions into account.

B.2.2.3 Iteration output

After each iteration consisting of the two steps described above we compute a control-output that shows the maximum value of the deviation between the old and the new solution, as well as the maximum and minimum value of each dressing function. We furthermore compute a rough ASCII plot of the propagator dressing functions $1/A$ and M (see Listing B.1 for the iteration output). The ASCII plot is very convenient because one can read off tendencies of the iteration procedure just by looking at the standard stream throughout the calculation. The information is also stored to a log-file separately. The ASCII plot has been computed by allocating a character array and initializing it with white spaces. We then computed a mapping of the external grid to the width of the character array, the 'y-axis' of the character array has been mapped from 0 to 1. Each letter in the ASCII diagram is a point of the external grid and has been mapped to the region covered by the character array. Each letter 'A' corresponds to a point of the function $\frac{1}{A}$, and each letter 'M' to a point of the mass function.

```
1 ----------------------------------------------------
2 -dressing--max.deviation------min-------------max----
3 ----------------------------------------------------
4 A  :        0.00E+00        1.00E+00        1.26E+00
5 B  :        8.67E-19        3.84E-07        3.54E-01
6 f1 :        4.19E-03        1.42E+00        3.92E+00
7 f2 :        5.14E-05       -5.70E-01        2.52E-05
8 f3 :        1.23E-03        5.92E-10        1.25E+00
```

[4]These iterations are full iterations of the whole system, consisting of two vertex updates and a converged propagator.

[5]In fact we did not apply a criterion of convergence, but rather implemented a fixed number of iterations. Usually we run 100 propagator iterations and consider the system as converged.

```
f4 :        8.17E-05       -1.15E-01        1.17E-01
f5 :        1.82E-04       -6.40E-02        6.28E-02
f6 :        2.91E-03        9.93E-01        2.72E+00
f7 :        2.32E-04       -2.81E-03        7.54E-01
f8 :        3.67E-04       -8.88E-01       -4.83E-10
g1 :        2.97E-03        1.00E+00        2.77E+00
g2 :        7.83E-05       -5.92E-01        3.43E-03
g3 :        8.69E-04       -6.64E-06        8.97E-01
g4 :        1.77E-04       -2.43E-02        5.95E-01
g5 :        1.36E-04       -4.60E-02        4.52E-02
g6 :        2.22E-05       -2.56E-01       -2.11E-04
g7 :        1.66E-04       -2.02E-03        5.34E-01
g8 :        1.00E-04       -3.30E-02        6.14E-04
-----------------------------------------------------
------------- min ------------ max ---------- avg ---
-----------------------------------------------------
Z1F:        1.00E+00        1.00E+00        1.00E+00
-----------------------------------------------------
----------- checking propagator integrity -----------
-----------------------------------------------------
------------------- propagator OK -------------------
-----------------------------------------------------
1                     AAAAAAAAAAA
|                  AAA
|                 A
|               AA
|AAAAAAAAAAAAA
|
|
|
|
|
|
|
|
|
|
|
|
|MMMMMMMMMM
|            M
|             M
|              M
|               M
|                M
0                 MMMMMMMMMMMMMMM
IR-------------------------------------------------UV
-----------------------------------------------------
```

Listing B.1: It is convenient to write an ASCII-plot of the quark-propagator dressings to the standard stream after each iteration step of the system vertex-propagator.

B.2.2.4 Finalization

Depending on the Yang-Mills input, the system converges to a reasonable amount of precision within roughly 10-12 iterations. The information of the vertex and propagator dressings are written to files, which are then processed further by `awk`-based Linux shell-scripts.

Appendix C

An alternative approach to the quark-gluon vertex DSE

Here we present an interesting alternative to the approach we employed in the main text[1]. The truncation is the same as the one presented in the main text 3.2, however, here we use a different momentum routing in the vertex equation. The idea is to use a tensor decomposition for a sub-diagram[2] contained in the non-abelian contribution. This vertex consists of the two quark-gluon vertices, connected by one dressed quark propagator. In Figure C.1 we show the momentum routing for the vertex equation employed in this study. We use the average fermion momentum p,

$$p = \frac{1}{2}\left(p_i + p_f\right), \tag{C.1}$$

the average gluon momentum Σ,

$$\Sigma = \frac{1}{2}\left(Q + Q'\right), \tag{C.2}$$

and the momentum Δ,

$$\Delta + Q' - Q = 0 \quad \Rightarrow \quad \Delta = Q - Q', \tag{C.3}$$

$$p_i + \Delta - p_f = 0 \quad \Rightarrow \quad \Delta = p_f - p_i. \tag{C.4}$$

[1]This procedure has been suggested by Gernot Eichmann, who successfully employed a similar construction for a study involving the fermion Compton vertex [171].

[2]The sub-diagram consists of two fully dressed quark-gluon vertices, connected by a dressed quark propagator. It thus corresponds to a non-1PI four-point function, see Figure C.2.

With (C.2) and (C.3) it follows that

$$\Sigma = \frac{1}{2}\left(Q + Q - \Delta\right) \;\Rightarrow\; Q = \Sigma + \frac{\Delta}{2}, \tag{C.5}$$

$$\Sigma = \frac{1}{2}\left(\Delta + Q' + Q'\right) \;\Rightarrow\; Q' = \Sigma - \frac{\Delta}{2}. \tag{C.6}$$

Furthermore, for the average momentum p_i^+ we have

$$p_i^+ = \frac{1}{2}\left(p_i + p + \Sigma\right), \tag{C.7}$$

and together with

$$p_i - p - \Sigma + 1 = 0 \Rightarrow p_i + Q = p + \Sigma \tag{C.8}$$

it follows that

$$p_i^+ = \frac{1}{2}\left(p_i + p_i + Q\right) = p_i + \frac{Q}{2}. \tag{C.9}$$

On the other hand, $p = \frac{1}{2}\left(p_i + p_f\right)$, such that through adding and subtracting a term we get

$$p_i^+ = \underbrace{\frac{1}{2}p_i + \frac{1}{2}p_f}_{=p} \underbrace{\underbrace{-\frac{1}{2}p_f + \frac{1}{2}p_i}_{=-\frac{\Delta}{2}} + \frac{Q}{2}}_{=+\frac{Q'}{2}} = p + \frac{Q'}{2}, \tag{C.10}$$

where we also used (C.3) and (C.4). Similarly we find

$$p_f^+ = \frac{1}{2}\left(p + \Sigma + p_f\right), \tag{C.11}$$

and with

$$p + \Sigma - Q' - p_f = 0 \Rightarrow p + \Sigma = Q' + p_f \tag{C.12}$$

we have

$$p_f^+ = \frac{1}{2}\left(Q' + p_f + p_f\right) = p_f + \frac{1}{2}Q'. \tag{C.13}$$

Using $p = \frac{1}{2}\left(p_i + p_f\right)$ again we finally get

$$p_f^+ = \underbrace{\frac{1}{2}p_i + \frac{1}{2}p_f}_{=p} + \underbrace{\underbrace{\frac{1}{2}p_f - \frac{1}{2}p_i}_{=\frac{\Delta}{2}} + \frac{1}{2}Q'}_{=+\frac{Q}{2}} = p + \frac{Q}{2}, \tag{C.14}$$

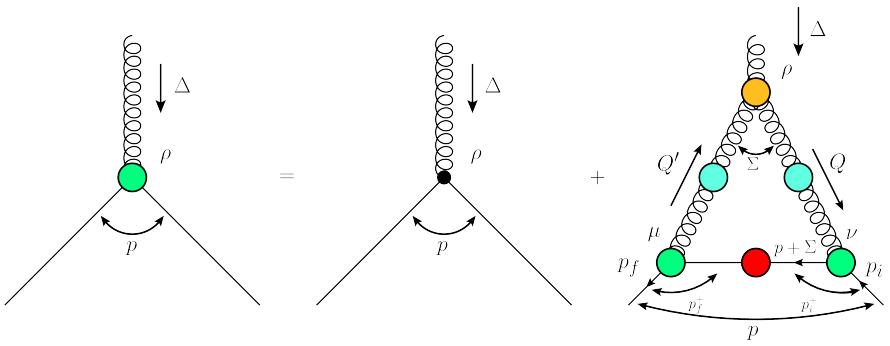

Figure C.1: The momentum routing for the vertex equation.

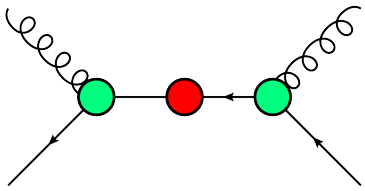

Figure C.2: This four point function is contained in the non-abelian diagram. It is spanned by 128 basis elements, see text.

where we used (C.3) and (C.4) as before. The three momenta p, Σ and Δ produce 6 Lorentz invariants,

$$\left\{p^2, \Sigma^2, \Delta^2, p.\Sigma, p.\Delta, \Sigma.\Delta\right\}. \tag{C.15}$$

We rename these invariants as follows:

$$\left.\begin{array}{rcl} p^2 & \to & p^2 \\ p.\Delta & \to & z \\ \Sigma^2 & \to & \sigma \\ \Delta^2 & \to & t \\ \Sigma.\Delta & \to & Z \\ p.\Sigma & \to & y \end{array}\right\} \Rightarrow \{\overbrace{p^2, z, y}^{fermion}, \overbrace{t, \sigma, Z}^{gluon}\}. \tag{C.16}$$

C.1 A basis for the lower quark line

The coordinates are chosen as shown in Fig. C.3.

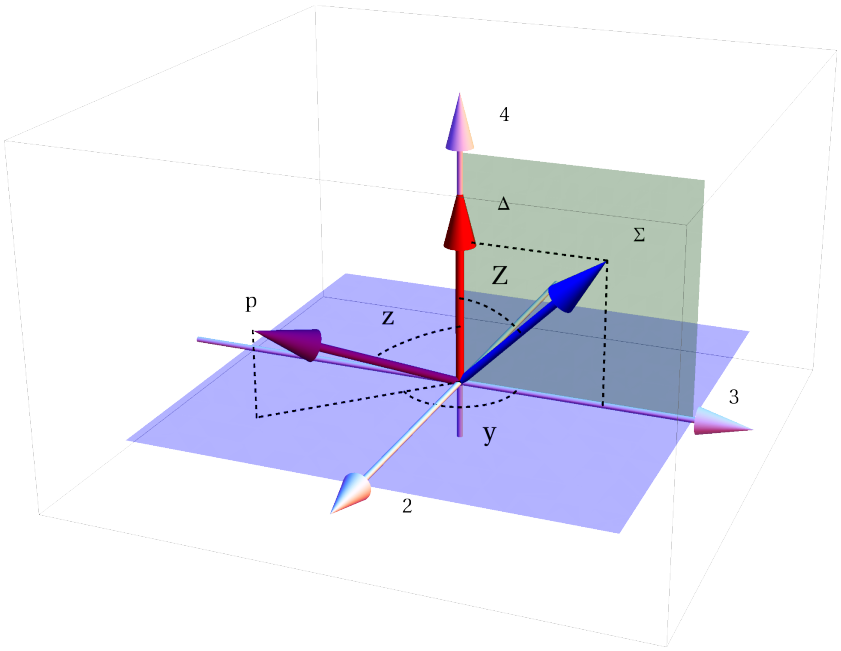

Figure C.3: The choice of coordinates.

The vectors Δ, Σ and p are then

$$\Delta = 2\sqrt{t}\begin{pmatrix} 0 \\ 0 \\ 0 \\ 1 \end{pmatrix}, \; \Sigma = \sqrt{\sigma}\begin{pmatrix} 0 \\ 0 \\ \sqrt{1-Z^2} \\ Z \end{pmatrix}, \; p = \sqrt{p^2}\begin{pmatrix} 0 \\ \sqrt{1-z^2}\sqrt{1-y^2} \\ \sqrt{1-z^2}y \\ z \end{pmatrix}. \tag{C.17}$$

Next we will use transversality with respect to the external momentum Δ, which we denote by a subscript T, as well as transversality with respect to both, Δ and Σ_T, denoted by a subscript t:

$$\Sigma_T^\mu = T_\Delta^{\mu\nu}\Sigma^\nu = \left(\delta^{\mu\nu} - \hat{\Delta}^\mu\hat{\Delta}^\nu\right)\Sigma^\nu, \tag{C.18}$$

where the $\hat{}$ indicates normalization. For the double-transverse p we have

$$p_t^\mu = p_T^\mu - \frac{p_T.\Sigma_T}{\Sigma_T^2}\Sigma_T^\mu. \tag{C.19}$$

Let us introduce the normalized external, transverse and double-transverse momenta d, s and r,

$$d^\mu = \hat{\Delta}^\mu, \tag{C.20}$$
$$s^\mu = \hat{\Sigma}_T^\mu, \tag{C.21}$$
$$r^\mu = \hat{p}_t^\mu. \tag{C.22}$$

The vectors $d,\ s$ and r are orthonormal:

$$d^2 = s^2 = r^2 = 1, \quad d.s = d.r = s.r = 0. \tag{C.23}$$

Together with the totally antisymmetric Levi-Civita symbol $\varepsilon^{\mu\alpha\beta\gamma}$ a fourth orthonormal (pseudo-)vector can be constructed,

$$v^\mu = \varepsilon^{\mu\alpha\beta\gamma} r^\alpha s^\beta d^\gamma, \tag{C.24}$$

where an additional γ_5 is needed to make v^μ transform as a vector under parity. Taking this into account we can form a complete and orthonormal tensor basis by appropriate combinations of the following elements:

$$\left\{\mathbb{1}, \not{r}, \not{s}, \not{d}, \gamma_5 v^\mu, r^\mu, s^\mu, d^\mu\right\}. \tag{C.25}$$

The vectors $v,\ r,\ s$ and d are just the Euclidean unit vectors in 4 dimensions:

$$v = \begin{pmatrix} 1 \\ 0 \\ 0 \\ 0 \end{pmatrix}, \quad r = \begin{pmatrix} 0 \\ 1 \\ 0 \\ 0 \end{pmatrix}, \quad s = \begin{pmatrix} 0 \\ 0 \\ 1 \\ 0 \end{pmatrix}, \quad d = \begin{pmatrix} 0 \\ 0 \\ 0 \\ 1 \end{pmatrix}. \tag{C.26}$$

The aim is to span the lower line of the non-abelian diagram by the orthonormal basis. We define the lower line of the non-abelian diagram as

$$\Gamma_B^{\mu\nu} := \Gamma^\mu(p_f^+, -Q') S(p+\Sigma) \Gamma^\nu(p_i^+, Q), \tag{C.27}$$

i.e. it consists of two full vertices connected by a full quark-propagator. This object can then be spanned by the basis

$$\left\{ \begin{array}{c} \gamma_5 v^\mu \\ r^\mu \\ s^\mu \\ d^\mu \end{array} \right\} \otimes \left\{ \begin{array}{c} \gamma_5 v^\nu \\ r^\nu \\ s^\nu \\ d^\nu \end{array} \right\} \otimes \left\{ \begin{array}{c} \mathbb{1} \\ \not{r} \\ \not{s} \\ \not{d} \\ \not{r}\not{s} \\ \not{r}\not{d} \\ \not{s}\not{d} \\ \not{r}\not{s}\not{d} \end{array} \right\}, \tag{C.28}$$

$$\tau_{i,a}^{\mu\nu} = X_i^{\mu\nu}(r,s,d) \left[\begin{array}{c} \mathbb{1} \\ \gamma_5 \end{array} \right]_i \tau_a(r,s,d), \tag{C.29}$$

where the γ_5 has to be chosen if the corresponding X_i contains one quantity of v^μ. Thus we can write

$$\Gamma_B^{\mu\nu}(p,\Sigma,\Delta) = \tag{C.30}$$
$$\sum_{i=1}^{16} \sum_{a=1}^{8} f_{i,a}(p^2, z, y, t, \sigma, Z) \underbrace{X_i^{\mu\nu}(r,s,d)}_{Lorentz} \left[\begin{array}{c} \mathbb{1} \\ \gamma_5 \end{array} \right]_i \underbrace{\tau_a(r,s,d).}_{Dirac}$$

$X_1^{\mu\nu} = \frac{1}{\sqrt{2}}(v^\mu v^\nu + r^\mu r^\nu)$	$X_9^{\mu\nu} = \frac{1}{\sqrt{2}}(r^\mu s^\nu + s^\mu r^\nu)$	$\tau_1 = \mathbb{1}$
$X_2^{\mu\nu} = \frac{1}{\sqrt{2}}(v^\mu v^\nu - r^\mu r^\nu)$	$X_{10}^{\mu\nu} = \frac{1}{\sqrt{2}}(v^\mu s^\nu + s^\mu v^\nu)$	$\tau_2 = \not{r}$
$X_3^{\mu\nu} = \frac{1}{\sqrt{2}}(v^\mu r^\nu + r^\mu v^\nu)$	$X_{11}^{\mu\nu} = \frac{1}{\sqrt{2}}(r^\mu s^\nu - s^\mu r^\nu)$	$\tau_3 = \not{s}$
$X_4^{\mu\nu} = \frac{1}{\sqrt{2}}(v^\mu r^\nu - r^\mu v^\nu)$	$X_{12}^{\mu\nu} = \frac{1}{\sqrt{2}}(v^\mu s^\nu - s^\mu v^\nu)$	$\tau_4 = \not{d}$
$X_5^{\mu\nu} = \frac{1}{\sqrt{2}}(s^\mu s^\nu + d^\mu d^\nu)$	$X_{13}^{\mu\nu} = \frac{1}{\sqrt{2}}(r^\mu d^\nu + d^\mu r^\nu)$	$\tau_5 = \not{r}\not{s}$
$X_6^{\mu\nu} = \frac{1}{\sqrt{2}}(s^\mu s^\nu - d^\mu d^\nu)$	$X_{14}^{\mu\nu} = \frac{1}{\sqrt{2}}(v^\mu d^\nu + d^\mu v^\nu)$	$\tau_6 = \not{r}\not{d}$
$X_7^{\mu\nu} = \frac{1}{\sqrt{2}}(s^\mu d^\nu + d^\mu s^\nu)$	$X_{15}^{\mu\nu} = \frac{1}{\sqrt{2}}(r^\mu d^\nu - d^\mu r^\nu)$	$\tau_7 = \not{s}\not{d}$
$X_8^{\mu\nu} = \frac{1}{\sqrt{2}}(s^\mu d^\nu - d^\mu s^\nu)$	$X_{16}^{\mu\nu} = \frac{1}{\sqrt{2}}(v^\mu d^\nu - d^\mu v^\nu)$	$\tau_8 = \not{r}\not{s}\not{d}$

Table C.1: The basis elements as presented in [171].

The basis elements summarized in Table C.1 obey an orthonormality relation,

$$\frac{1}{4}\mathrm{Tr}\left\{\bar{\tau}_{i,a}^{\nu\mu}\tau_{j,b}^{\mu\nu}\right\} = X_i^{\mu\nu}X_j^{\mu\nu}\frac{1}{4}\mathrm{Tr}\{\bar{\tau}_a\tau_b\} = \delta_{ij}\delta_{ab}, \tag{C.31}$$

where $\bar{\tau}$ means

$$\bar{\tau}_{i,a}^{\nu\mu}(r,s,d) = C\tau_{i,a}^{\mu\nu}(-r,-s,-d)^T C^T. \tag{C.32}$$

C.2 Outer quark-gluon vertex basis (orthonormal)

We will employ two different basis sets to span the quark-gluon vertex in this calculation. For the actual evaluation of the quark-gluon vertex dressing functions we use an orthonormal basis, while for the evaluation of all vertices appearing internally we will use a non-orthonormal basis. For the orthonormal basis we use another frame, where we exploit the Lorentz invariance of the equation. There we use the momenta as depicted in Figure C.4.

The momenta p and Σ are redefined,

$$p = \sqrt{p^2}\begin{pmatrix} 0 \\ 0 \\ \sqrt{1-z^2} \\ z \end{pmatrix},\ \Sigma = \sqrt{\sigma}\begin{pmatrix} 0 \\ \sqrt{1-Z^2}\sqrt{1-y^2} \\ \sqrt{1-Z^2}y \\ Z \end{pmatrix}, \tag{C.33}$$

and Δ is defined as before. The transverse part of the quark-gluon vertex is then given by

$$\Gamma^\rho(p,\Delta) = \sum_{i=1}^{8} f_i(p,\Delta)\tau_i^\rho(R,d), \tag{C.34}$$

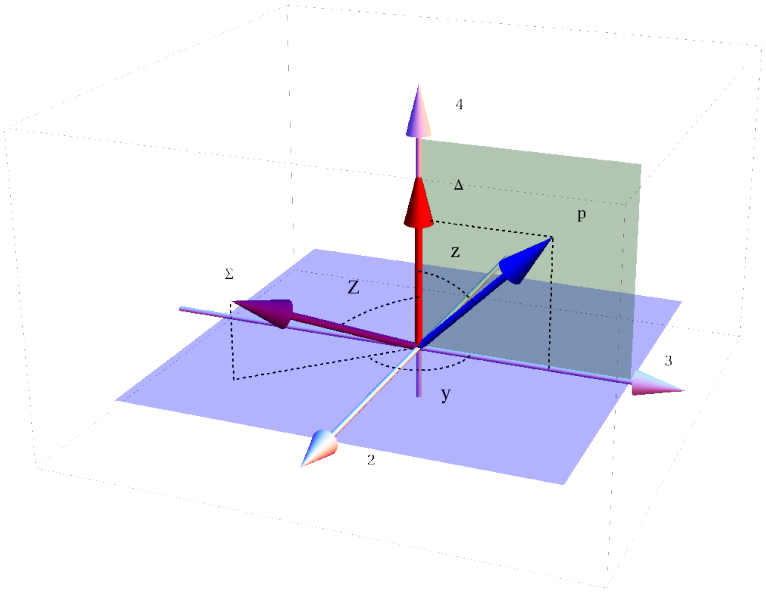

Figure C.4: The choice of coordinates for the orthonormal basis.

The orthonormal basis elements read (equation (D22) of [88])

$$\left\{ \begin{array}{c} \frac{1}{\sqrt{2}}\gamma_t^\mu \\ R^\mu \\ d^\mu \end{array} \right\} \otimes \left\{ \begin{array}{c} \mathbb{1} \\ \not{d} \\ \not{R} \\ \not{R}\not{d} \end{array} \right\}, \tag{C.35}$$

where we used the normalized gluon momentum

$$d^\mu := \hat{\Delta}^\mu = \begin{pmatrix} 0 \\ 0 \\ 0 \\ 1 \end{pmatrix}, \tag{C.36}$$

and introduced the normalized average momentum transverse to the gluon momentum,

$$R^\mu := \hat{p}_T^\mu = \begin{pmatrix} 0 \\ 0 \\ 1 \\ 0 \end{pmatrix}. \tag{C.37}$$

Note that the element γ_t^μ is transverse to d and R, i.e.

$$\gamma_T^\mu = \left(\delta^{\mu\nu} - d^\mu d^\nu\right)\gamma^\nu, \tag{C.38}$$

$$\gamma_t^\mu = \gamma_T^\mu - (\gamma_T.R)R^\mu. \tag{C.39}$$

This gives 12 tensor structures in total. We use the 8 transverse structures to span the vertex, i.e. the ones obeying

$$d.\tau_i = 0, \tag{C.40}$$

see Table C.2.

$\tau_1^\mu = \frac{1}{\sqrt{2}}\gamma_t^\mu \mathbb{1}$	$\tau_5^\mu = R^\mu \mathbb{1}$
$\tau_2^\mu = \frac{1}{\sqrt{2}}\gamma_t^\mu \not{d}$	$\tau_6^\mu = R^\mu \not{d}$
$\tau_3^\mu = \frac{1}{\sqrt{2}}\gamma_t^\mu \not{R}$	$\tau_7^\mu = R^\mu \not{R}$
$\tau_4^\mu = \frac{1}{\sqrt{2}}\gamma_t^\mu \not{R}\not{d}$	$\tau_8^\mu = R^\mu \not{R}\not{d}$

Table C.2: The orthonormal basis of the quark gluon vertex, [88].

Again the basis elements fulfill an orthonormality relation,

$$\frac{1}{4}\mathrm{Tr}\{\bar{\tau}_i^\mu \tau_j^\mu\} = \delta_{ij}, \tag{C.41}$$

where $\bar{\tau}_i^\mu = (\tau_i^\mu)^\dagger$ is the hermitean conjugate of the basis element.

C.3 Inner quark-gluon vertex basis

The dressed quark-gluon vertex also appears in the lower quark-line of the non-abelian diagram. There we employ a different basis to span the two dressed vertices, as there is no benefit from the basis elements being orthonormal there. The basis is taken from [171], equation (89). Its elements are shown in Table C.3 and we choose the coordinates as depicted in Figure C.5.

In this frame, the momenta are

$$Q^\mu = Q\begin{pmatrix}0\\0\\0\\1\end{pmatrix},\ k^\mu = k\begin{pmatrix}0\\0\\\sqrt{1-\xi^2}\\\xi\end{pmatrix}, \tag{C.42}$$

where Q^μ is the gluon momentum and k^μ the average quark momentum.

Hereby, $t_{ab}^{\mu\nu}$ reads

$$t_{ab}^{\mu\nu} = a \cdot b\delta^{\mu\nu} - b^\mu a^\nu, \tag{C.43}$$

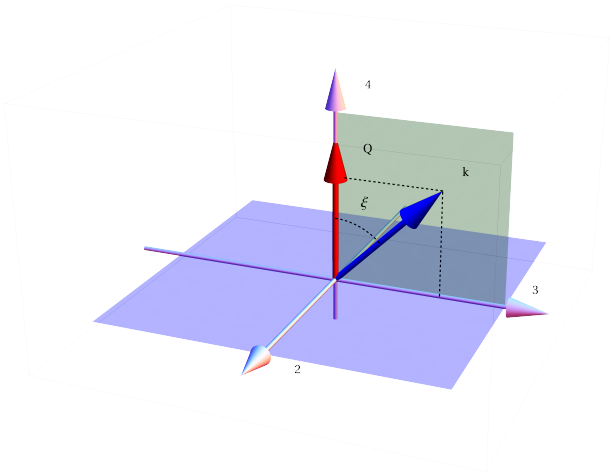

Figure C.5: The choice of coordinates for the inner basis.

$\rho_1^\mu = t_{QQ}^{\mu\nu}\gamma^\nu$	$\rho_5^\mu = t_{QQ}^{\mu\nu} i k^\nu$
$\rho_2^\mu = t_{QQ}^{\mu\nu} k\cdot Q \frac{i}{2}[\gamma^\nu, \not{K}]$	$\rho_6^\mu = t_{QQ}^{\mu\nu} k^\nu \not{K}$
$\rho_3^\mu = \frac{i}{2}[\gamma^\mu, \not{Q}]$	$\rho_7^\mu = t_{Qk}^{\mu\nu} k\cdot Q\gamma^\nu$
$\rho_4^\mu = \frac{1}{6}[\gamma^\mu, \not{K}, \not{Q}]$	$\rho_8^\mu = t_{Qk}^{\mu\nu} \frac{i}{2}[\gamma^\nu, \not{K}]$

Table C.3: The inner basis of the quark-gluon vertex, [171]. The momenta are shown in Figure C.5.

and the triple-commutator is

$$[a,b,c] = [a,b]c + [b,c]a + [c,a]b. \tag{C.44}$$

The transverse parts of the quark-gluon vertex are then spanned by

$$\Gamma_T^\mu(k,Q) = \sum_{i=1}^{8} g_i(k^2, Q^2, k\cdot Q)\rho_i^\mu(k,Q). \tag{C.45}$$

C.4 Change of basis

The quark-gluon vertex dressings are evaluated in an orthonormal basis, but for the determination of the dressing functions of the four point function and the quark propagator a different basis is employed. Therefore we have to calculate the projections of the orthonormal outer onto the inner basis. This gives the desired dressing functions in the inner basis in terms of linear combinations of the dressing functions of the orthonormal basis. Suppressing

momentum dependence, the vertex reads

$$\Gamma^{\mu}_{\tau} = \sum_{i=1}^{8} f_i \tau_i^{\mu}, \tag{C.46}$$

$$\Gamma^{\mu}_{\rho} = \sum_{i=1}^{8} g_i \rho_i^{\mu}, \tag{C.47}$$

such that the relations between the dressing functions g_i and f_i are obtained by

$$\sum_{j=1}^{8} g_j(\bar{\rho}_i^{\mu}, \rho_j^{\mu}) = \sum_{k=1}^{8} f_k(\bar{\rho}_i^{\mu}, \tau_k^{\mu}). \tag{C.48}$$

The scalar product $(\cdot,\cdot)$ means Lorentz contraction and Dirac tracing,

$$l_i := \sum_{j=1}^{8} g_j \frac{1}{4}\mathrm{Tr}\{\bar{\rho}_i^{\mu}\rho_j^{\mu}\} = \sum_{k=1}^{8} f_k \frac{1}{4}\mathrm{Tr}\{\bar{\rho}_i^{\mu}\tau_k^{\mu}\} =: r_i. \tag{C.49}$$

The projections on the left hand side, l_i, result in linear combinations of the inner quark-gluon vertex dressings $g_i,\ i \in [1,8]$, while the right hand side projections, r_i, hold linear combinations of the orthonormal quark-gluon vertex dressings $f_i,\ i \in [1,8]$. This system of linear equations can then be solved to obtain the desired dressing functions.

C.5 Analysis of the vertex equation

Here we study the structure of the vertex equation by employing the basis sets defined in the preceding sections. We want to span the four-point function as follows,

$$\Gamma_B^{\mu\nu}(p,\Sigma,\Delta) = \tag{C.50}$$
$$\sum_{i=1}^{16}\sum_{a=1}^{8} f_{i,a}(p^2,z,y,t,\sigma,Z) X_i^{\mu\nu}(r,s,d) \begin{bmatrix} \mathbb{1} \\ \gamma_5 \end{bmatrix}_i \tau_a(r,s,d),$$

where we can use the orthonormality relation

$$\frac{1}{4}\mathrm{Tr}\left\{\bar{\tau}_{i,a}^{\nu\mu}\tau_{j,b}^{\mu\nu}\right\} = X_i^{\mu\nu}X_j^{\mu\nu}\mathrm{Tr}\{\bar{\tau}_a\tau_b\} = \delta_{ij}\delta_{ab} \tag{C.51}$$

to obtain the dressing functions $f_{i,a}$. Considering the Lorentz and Dirac structure only, we have

$$
\begin{aligned}
& f_{i,a}(p^2, z, y, t, \sigma, Z) \qquad\qquad (C.52)\\
&= \frac{1}{4}\mathrm{Tr}\left\{ X_i^{\mu\nu}\bar{\tau}_a(r,s,d) \left[\begin{array}{c} \mathbb{1} \\ \gamma_5 \end{array} \right]_i \Gamma_B^{\mu\nu} \right\} \\
&= \sum_{k=1}^{8}\sum_{l=1}^{8} g_k(p_f^+, -Q') g_l(p_i^+, Q) X_i^{\mu\nu}(r,s,d) \times \frac{1}{4} \\
&\mathrm{Tr}\left\{ \bar{\tau}_a(r,s,d) \left[\begin{array}{c} \mathbb{1} \\ \gamma_5 \end{array} \right]_i \rho_k^{\mu}(p_f^+, -Q') S(p+\Sigma) \rho_l^{\nu}(p_i^+, Q) \right\}.
\end{aligned}
$$

Note that the quark-gluon vertices in this expression are spanned by the inner basis (C.47). The angular dependence of the dressing functions (variables y, z and Z) will be expanded in Chebyshev polynomials. For the evaluation of the vertex equation we plug the expansion of the four point function into the non-abelian diagram. Now we use the orthonormal basis (C.46), which allows for easy disentanglement of the dressing functions. The vertex equation reads

$$
\begin{aligned}
& \sum_{j=1}^{8} f_j(p^2, z, t)\tau_j^{\rho}(p, \Delta) = \qquad\qquad (C.53)\\
& Z_{1F}\gamma^{\rho} + ig^2 \frac{N_C}{2} \int_{\Sigma} \sum_{i=1}^{16}\sum_{a=1}^{8} f_{i,a}(p^2, z, y, t, \sigma, Z) \\
& \times X_i^{\mu\nu}(r,s,d) \left[\begin{array}{c} \mathbb{1} \\ \gamma_5 \end{array} \right]_i \tau_a(r,s,d) \\
& \times \Gamma^{\rho\mu'\nu'}(\Sigma, \Delta) D^{\mu\mu'}(Q') D^{\nu'\nu}(Q),
\end{aligned}
$$

where $\Gamma^{\rho\mu'\nu'}$ and $D^{\mu\mu'}$ are the 3-gluon vertex and the gluon-propagator respectively, Z_{1F} is the renormalization constant. The factor of i and the sign has already been chose in a consistent way, also color space has been taken into account (see Section B.1.3 for the computation of the color factor). The integration is performed over the loop momentum Σ. In hyper-spherical coordinates this corresponds to a radial component σ, as well as to the two angles y and Z. Exploiting the orthonormality of the outer quark gluon

vertex basis we find

$$\begin{aligned} f_k(p^2,z,t) &= Z_{1F}\frac{1}{4}\mathrm{Tr}\{\bar{\tau}_k^\rho(p,\Delta)\gamma^\rho\} \\ &-ig^2\frac{N_C}{2}\int_\Sigma \sum_{i=1}^{16}\sum_{a=1}^{8} f_{i,a}(p^2,z,y,t,\sigma,Z) \\ &\times\frac{1}{4}\mathrm{Tr}\{\bar{\tau}_k^\rho(p,\Delta)X_i^{\mu\nu}(r,s,d)\left[\begin{array}{c}\mathbb{1}\\ \gamma_5\end{array}\right]_i\tau_a(r,s,d) \\ &\times\Gamma^{\rho\mu'\nu'}(\Sigma,\Delta)D^{\mu\mu'}(Q')D^{\nu'\nu}(Q)\}. \end{aligned} \tag{C.54}$$

The pure Lorentz part of the right hand side of this expression can be dragged out of the trace, such that the summand factorizes. Considering the integrand of the right hand side only, we thus have

$$\begin{aligned} & f_{i,a}(p^2,z,y,t,\sigma,Z)\frac{1}{4}\mathrm{Tr}\{\bar{\tau}_k^\rho(p,\Delta) \\ & \times X_i^{\mu\nu}(r,s,d)\left[\begin{array}{c}\mathbb{1}\\ \gamma_5\end{array}\right]_i\tau_a(r,s,d) \\ & \times\Gamma^{\rho\mu'\nu'}(\Sigma,\Delta)D^{\mu\mu'}(Q')D^{\nu'\nu}(Q)\} \\ = \quad & f_{i,a}(p^2,z,y,t,\sigma,Z) \\ & \times\underbrace{X_i^{\mu\nu}(r,s,d)\Gamma^{\rho\mu'\nu'}(\Sigma,\Delta)D^{\mu\mu'}(Q')D^{\nu'\nu}(Q)}_{=:M_i^\rho(y,t,\sigma,Z)} \\ & \times\underbrace{\frac{1}{4}\mathrm{Tr}\{\bar{\tau}_k^\rho(p,\Delta)\left[\begin{array}{c}\mathbb{1}\\ \gamma_5\end{array}\right]_i\tau_a(r,s,d)\}}_{=:M_{k,i,a}^\rho}. \end{aligned} \tag{C.55}$$

Using these pre-calculable structures, equation (C.54) becomes

$$\begin{aligned} f_k(p^2,z,t) &= Z_{1F}\underbrace{\frac{1}{4}\mathrm{Tr}\{\bar{\tau}_k^\rho(p,\Delta)\gamma^\rho\}}_{=:M_k} -ig^2\frac{N_C}{2} \\ &\times\int_\Sigma\sum_{i=1}^{16}\sum_{a=1}^{8} f_{i,a}(p^2,z,y,t,\sigma,Z)\underbrace{M_i^\rho(y,t,\sigma,Z)M_{k,i,a}^\rho}_{=:M_{k,i,a}(y,t,\sigma,Z)} \\ = \quad & Z_{1F}M_k - ig^2\frac{N_C}{2} \\ & \times\int_\Sigma\sum_{i=1}^{16}\sum_{a=1}^{8} f_{i,a}(p^2,z,y,t,\sigma,Z)M_{k,i,a}(y,t,\sigma,Z). \end{aligned} \tag{C.56}$$

The M_k and $M_{k,i,a}(y,t,\sigma,Z)$ can be calculated in advance, using a computer algebra system[3].

C.6 The structure of the elements $M_{k,i,a}$

Besides the dressing functions of the four point function, the only input to the vertex equation are the elements of $M_{k,i,a}$, which hold the information of the contracted Lorentz- and traced Dirac space, where

$$M_{k,i,a}(y,t,\sigma,Z) = M_i^\rho(y,t,\sigma,Z)M_{k,i,a}^\rho. \tag{C.57}$$

With the quark-gluon vertex dressing label $k \in [1,8]$, the four point function Lorentz-part label $i \in [1,16]$ and the four-point function Dirac-part label $a \in [1,8]$, the cardinality of the set of $\{k,i,a\}$ 3-tuples of indices is $k \cdot i \cdot a = 8 \cdot 16 \cdot 8 = 1024$. However, we are fortunate here, because many of the $M_{k,i,a}$ turn out to be zero. While in the most general case one would have to sum up $i \cdot a = 16 \cdot 8 = 128$ products of the four-point dressings times $M_{k,i,a}$ elements for every of the 8 ks, here their number is reduced significantly, as for each of the 8 ks at most 16 elements have to be summed up. The cardinality of the set of relevant$\{k,i,a\}$ 3-tuples drops from 1024 to 104, meaning that only 104 out of 128 vertex dressings have to be evaluated. Let us work this out to see which of the 4-point function dressing are needed.

Once the $M_{k,i,a}$ are known, the structure of the non-vanishing elements can be studied. For a given $k \in [1,8]$, the i and a indices of the nonzero elements come in two classes of symmetry. The first symmetry for the indices i and a is established for the elements $k \in [1,4]$, the second symmetry class for the i and a indices is realized for $k \in [5,8]$. Let us start with $k \in [1,4]$. Here all indices of $i \in [1,16]$ appear, but for each of the 16 is only one a leads to a nonzero element $M_{k,i,a}$. For a given value of i, the corresponding values of a follow a pattern, see Tables C.4 and C.5.

i	1	2	3	4	5	6	7	8	9	10	11	12	13	14	15	16
a	X	X	Y	Y	X	X	X	X	X	Y	X	Y	X	Y	X	Y

Table C.4: The symmetry pattern for nonzero elements of $M_{k\in[1,4],i,a}$.

This accounts for $k \cdot i = 4 \cdot 16 = 64$ nonzero elements, because each i is only paired with just one a. The second symmetry class is realized for values of $k \in [5,8]$, see Table C.6 and C.7.

[3]Here we used FORM [89] and Mathematica [168] to have two independent calculations for comparison.

k	X	Y
1	2	8
2	6	5
3	5	6
4	8	2

Table C.5: The as belonging to k and i are obtained by plugging the values of X and Y into Table C.4.

i	1	2	5	6	7	8	9	11	13	15
a	Z	Z	Z	Z	Z	Z	Z	Z	Z	Z

Table C.6: The symmetry pattern for nonzero elements of $M_{k\in[5,8],i,a}$.

This accounts for $k \cdot i = 4 \cdot 10 = 40$ nonzero elements. Thus, in total we have the $64 + 40 = 104$ nonzero elements, which are summarized in Table C.8.

Using the symmetry, equation (C.56) becomes

$$f_k(p^2, z, t) = Z_{1F} M_k - \\ ig^2 \frac{N_C}{2} \int_\Sigma \sum_{l \in \mathcal{P}_k} f_l(p^2, z, y, t, \sigma, Z) M_{k,l}(y, t, \sigma, Z), \tag{C.58}$$

where the index l runs through the 104 nonzero elements in partitions $\mathcal{P}_k$ of 16 for $k \in [1, 4]$, and in partitions $\mathcal{P}_k$ of 10 for $k \in [5, 8]$. The dressing functions of the four point function have to be stored in the l-indexed array according to the order of their appearance in the $M_{k,l}$ elements. Note that each of the 104 dressing functions appears exactly one time for all ks, i.e. the set of the four point function dressings contributing to a particular quark-gluon vertex dressing labeled by k is disjoint from all sets contributing to the other 7 quark-gluon vertex dressing functions labeled by $[1, 8] \setminus \{k\}$.

C.7 Relation between the dressing functions

In general, the four-point function is spanned by 128 basis elements, dressed with 128 functions, see equation (C.50). There are 16 Lorentz- and 8 Dirac-parts, giving rise to the $16 \times 8 = 128$ elements. The quark-gluon vertex equation takes 128 dressing functions as an input, see equation (C.54). Above we have shown, that equation (C.54) reduces to equation (C.56), where the $M_{k,i,a}$ elements are the pre-calculated trace of equation (C.54). The indices k, i and a label the quark-gluon vertex dressing, the Lorentz-part and the

k	Z
5	1
6	4
7	3
8	7

Table C.7: The as belonging to k and i are obtained by pairing the is of Table C.6 with the Z as given here.

k	X	Y	Z
1	2	8	0
2	6	5	0
3	5	6	0
4	8	2	0
5	0	0	1
6	0	0	4
7	0	0	3
8	0	0	7

Table C.8: Summary of nonzero elements. For a given k, take the non-zero values of X, Y and Z and plug them into the Tables C.4 and C.6 to obtain the corresponding a for a given i. The resulting 104 3-tuples of {k,i,a} are the non-zero elements of $M_{k,i,a}$.

Dirac-part respectively. In the most general case, for each of the eight quark-gluon vertex dressings the full double sum would have to be carried out, i.e. a sum over 128 elements. However, here the symmetry of the construction can be exploited. In fact, most of the 1024 $M_{k,i,a}$ are zero, and the terms appearing in the k sums are also mutually exclusive, which reduces the 8 double sums from 128 terms down to 16 or even 10 terms each (see Section C.6 for a discussion). The 104 non-zero elements summarized in Table C.8 have thus been labeled by a multi index l, see equation (C.58). The fact that the terms in the eight sums are mutually exclusive, plus the fact that there are 104 non-zero elements leads to the conclusion, that 24 combinations {i,a} need not to be evaluated. The 104 remaining dressing functions are either imaginary or real. Table C.9 summarizes the dependence of the quark-gluon vertex dressings on the four point function dressings.

All traces needed for this calculation have been performed using FORM [89]. The FORM output is then processed employing `sed` and bash shell

scripts.

C.8 Solving the system

One iteration consists of several steps:

1. Four-point function trace evaluation
2. Vertex update
3. Change of basis
4. Propagator update

The system has been parallelized and designed to run on a CPU cluster using MPI. Here we have chosen a simple way of parallelization, where 104 threads evaluate one four-point function dressing each. This is the computationally most expensive part. The results of the dressings are broadcasted to all threads once the calculation has been performed and the vertex and propagator can be evaluated. One problem of this approach is that one has to store a four-point function depending on 6 Lorentz invariants times 104, as we have 104 dressing functions. This might become a problem on smaller clusters, where RAM capacity per thread is not big. In order to reduce the memory consumption we thus used a Chebyshev expansion for the three angular variables of the four point function. Even though the system iterates stable by now and converges, the dynamically generated mass is too low. This issue is currently under investigation.

f_i	proportional to $f_{i,a}$															
f_1	$\underline{12}$	$\underline{22}$	$\underline{38}$	$\underline{48}$	$\underline{52}$	$\underline{62}$	$\underline{72}$	$\underline{82}$	$\underline{92}$	$\underline{108}$	$\underline{112}$	$\underline{128}$	$\underline{132}$	$\underline{148}$	$\underline{152}$	$\underline{168}$
$\underline{f_2}$	16	26	35	45	56	66	76	86	96	105	116	125	136	145	156	165
$\underline{f_3}$	15	25	36	46	55	65	75	85	95	106	115	126	135	146	155	166
f_4	$\underline{18}$	$\underline{28}$	$\underline{32}$	$\underline{42}$	$\underline{58}$	$\underline{68}$	$\underline{78}$	$\underline{88}$	$\underline{98}$	$\underline{102}$	$\underline{118}$	$\underline{122}$	$\underline{138}$	$\underline{142}$	$\underline{158}$	$\underline{162}$
$\underline{f_5}$	11	21	51	61	71	81	91	111	131	151	—	—	—	—	—	—
f_6	$\underline{14}$	$\underline{24}$	$\underline{54}$	$\underline{64}$	$\underline{74}$	$\underline{84}$	$\underline{94}$	$\underline{114}$	$\underline{134}$	$\underline{154}$	—	—	—	—	—	—
f_7	$\underline{13}$	$\underline{23}$	$\underline{53}$	$\underline{63}$	$\underline{73}$	$\underline{83}$	$\underline{93}$	$\underline{113}$	$\underline{133}$	$\underline{153}$	—	—	—	—	—	—
$\underline{f_8}$	17	27	57	67	77	87	97	117	137	157	—	—	—	—	—	—

Table C.9: Summary of nonzero dressing functions. The f_i in the column on the left are the quark-gluon vertex dressing functions given in equation (C.34), appearing on the left-hand side of equation (C.56). The $f_{i,a}$ elements whose indices i and a are shown in a concatenated way in the following cells are the four-point function dressing functions appearing on the right-hand side of equation (C.56). Elements marked with an under-bar are imaginary. The table shows the dependence of the quark-gluon vertex dressings on the dressings of the four point function which are labeled by the indices i and a, where $i \in [1, 16]$ and $a \in [1, 8]$. For example, in the first line, i.e. for f_1 the first entry reads $\underline{12}$, meaning the first dressing contributing to f_1 is $f_{i,a} = \underline{\mathrm{f}}_{1,2}$, which is an imaginary quantity. The 8^{th} entry of $\underline{\mathrm{f}}_5$ on the other hand reads 111, meaning $f_{i,a} = f_{11,1}$. For a given quark-gluon vertex dressing f_i, only the elements shown in the corresponding line have to be taken into account by summing them up after multiplication with the corresponding M_{kia} element. The quark-gluon vertex dressings f_2, f_3, f_5, and f_8 inherit the imaginary nature from the multiplication of the four-point function dressings with the purely imaginary $M_{k,i,a}$ elements. The elements in the various basis systems are chosen such that the dressing functions going with the inner basis are real-valued quantities.

Appendix D

Induced branch cuts in the radial integration-plane

As induced branch cuts are a major obstacle when extending one-loop expressions to the complex plane, we briefly discuss how they come about and how they can be dealt with. To this end consider a (Euclidean) two-point function of the form

$$\mathscr{M}(x) = \langle \mathscr{O}(p)\, \mathscr{O}(-p) \rangle = \int \frac{d^4k}{(2\pi)^4} \frac{f(p, k, \cos\theta_1)}{g(p, k, \cos\theta_1)}. \tag{D.1}$$

The fact that the integrand is expressed as a fraction of two functions allows us to access the non-analyticities of the integrand via the zeros of g (where we assume that zeros in g give rise to integrable singularities, f is assumed to be analytic and non-zero everywhere). Depending on the superficial degree of divergence it might be necessary to regularize such integrals, e.g. by employing a BPHZ procedure. Using the relation (A.7) to switch to hyper-sphericals, as well as performing the trivial angular integration, one is left with

$$\mathscr{M}(x) = \int_0^{\Lambda^2} dy\; y \int_{-1}^{1} dz \sqrt{1-z^2} \frac{\tilde{f}(x, y, z)}{g(x, y, z)}, \tag{D.2}$$

where, as usual, we use the abbreviations $p^2 = x,\ q^2 = y$ and $\cos \angle_{p,q} = z$. The $\tilde{f}$ is to signal that we absorbed the trivial constants from the integral measure and the angular integrations into f, Λ^2 is the UV cut-off. As long as $x \in \mathbb{R}_0^+$, the integration can be performed in a straight-forward manner. However, we are interested in the case where this is not the case. The problem that might arise here is that the angular integral can induce branch cuts in the complex plane of the radial integration variable for a given $x \in \mathbb{C}$, such that

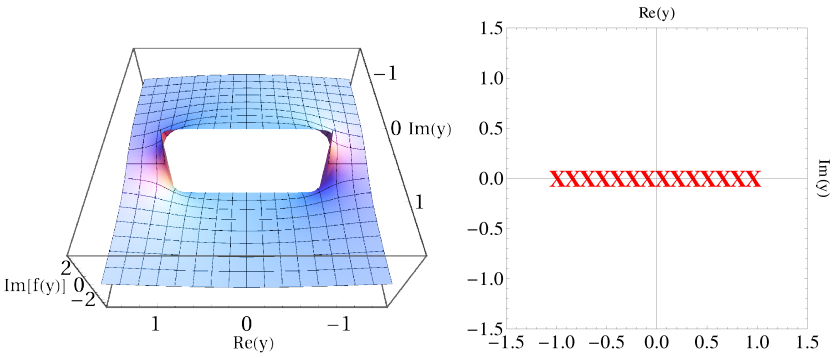

Figure D.1: The branch cut arising form equation $(D.3)$ for $y \in [-1,1]$.

the contour has to be deformed in order to avoid the branch cut. Consider for example the integral

$$f(y) = \int_a^b \frac{dz}{y+z} = \log z \Big|_{y+a}^{y+b} = \log\left(\frac{y+b}{y+a}\right). \tag{D.3}$$

With the arbitrary choice of $a = -1$ and $b = +1$ one finds a branch cut along the interval $y \in [-1,1]$, see Figure D.1.

The branch cut shows up in the complex y-plane because the angular variable z picks up singular values. This can be already read off the integrand without solving the angular integral. One only has to find all values of $y \in \mathbb{C}$ (for a given $x \in \mathbb{C}$) for which the z-integrand becomes singular. For equation $(D.3)$ with integral boundaries ± 1 this is trivial, as all values of y for which the integrand can become singular are obviously given by $y \in [-1,1]$ (if z runs from -1 to $+1$, let y run from $+1$ to -1). In the more general case $(D.2)$ one can parametrize the branch cut using the angular variable z, while there is some extra dependence on the square of the external momentum x that remains,

$$c(x) \;=\; y_0(x,z)\Big|_{z=-1}^{z=+1}, \tag{D.4}$$

and $y_0(x,z)$ is a solution of

$$g(x,y,z) = 0, \;\; x \in \mathbb{C}, \;\; x \; const., \;\; z \in [-1,1]. \tag{D.5}$$

It is important to note that this provides all branch cuts parametrized by the angular variable and all non-analyticities that are purely y-dependent[1].

[1]Note that 2d and 3d animations of branch-cuts induced by angular integration can be found on the DVD enclosed to this thesis, see Appendix K for details.

Appendix E

Predicting the branch point locations of the solution

The branch point locations in the solution of a one-loop expression in the complex plane can be predicted easily once the analytic structure in the complex plane of the radial integration variable has been obtained, see equation (D.5). In this analysis we re-obtained the long known results published in [172, 173, 107].

The calculation is formulated in a language suitable for the problems we are dealing with, further details can be found here [174]. This analysis serves as guideline for the validity of the result of the numerical complex one-loop integration. As can be seen in the main text, sometimes there are more than just one branch-cut showing up in the result. Resolving the branch points numerically can be very hard because the numerics becomes dominated by noise present through the non-analyticities of the result in the vicinity of the cut. For the perturbative case one can however easily predict the exact locations of the branch-point(s) in the result. This is an obvious statement, as a non-analytic point in the result has to originate somehow from the one-loop integral that represents the correlator. From this point of view it is clear that one has to look for situations in the complex plane of the radial integration variable that do not allow for the existence of an arbitrarily deformed contour. These points can be extracted analytically, providing a valuable check for the result of the numerics. There are three simple analytic steps that have to be performed.

- STEP 1: (*Integrand analysis*) In this step one has to perform a thorough analysis of the analytic properties of the y-integral after the z-integral has been performed. This yields all poles and cuts in the y-plane.

- STEP 2: (*Identify candidates*) Candidates for possible branch-point locations can be found by putting the end-points of the x-dependent branch-cuts to values where only y-dependent poles are located.
- STEP 3: (*Check contours*) Now one only has to check the validity of the contour for the situations resulting from STEP 2

Let us discuss the procedure by considering a generic Euclidean correlator with masses $m_1 \in \mathbb{R}^+$ and $m_2 \in \mathbb{R}^+$,

$$\mathscr{M}(x) = \langle \mathscr{O}(p)\, \mathscr{O}(-p) \rangle_{d=4} = \int \frac{d^4k}{(2\pi)^4} \frac{f(k, p-k)}{\left((p-k)^2 + m_1^2\right)\left(k^2 + m_2^2\right)}, \quad \text{(E.1)}$$

with $f(k, p-k)$ being a function built from the Lorentz invariants. Using hyper-sphericals (A.7) again, we get

$$\mathscr{M}(x) = \int_0^\infty dy\; y \int_{-1}^1 dz \sqrt{1-z^2} \frac{\tilde{f}(x, y, z)}{\left(x + y - 2\sqrt{x}\sqrt{y}z + m_1^2\right)\left(y + m_2^2\right)}, \quad \text{(E.2)}$$

where we used the identifications $x = p^2$, $y = k^2$ and $z = \cos\theta_1$ as usual. Trivial constants have been absorbed into $\tilde{f}$.

- STEP 1: Using the procedure outlined in Appendix D we find one pole and a branch cut,

$$\begin{aligned} y_1 &= -m_2^2, \quad \text{(E.3)} \\ y_2(x,z) &= -m_1^2 - x + 2xz^2 - 2\sqrt{-m_1^2 x z^2 - x^2 z^2 + x^2 z^4}, \\ y_3(x,z) &= -m_1^2 - x + 2xz^2 + 2\sqrt{-m_1^2 x z^2 - x^2 z^2 + x^2 z^4}. \end{aligned}$$

- STEP 2: Here we have to solve the equations $y_2(x,z) = y_1$ and $y_3(x,z) = y_1$ (where $z = \pm 1$) with respect to x. This yields

$$x = -(m_1 \pm m_2)^2. \quad \text{(E.4)}$$

- STEP 3: An analysis of the two solutions show that only the solution with the '+' sign gives rise to a branch-point in the solution, see Figure E.1.

From the procedure we conclude that the only branch-point in the complex x-plane of the correlator (E.1) is located at

$$x = -(m_1 + m_2)^2. \quad \text{(E.5)}$$

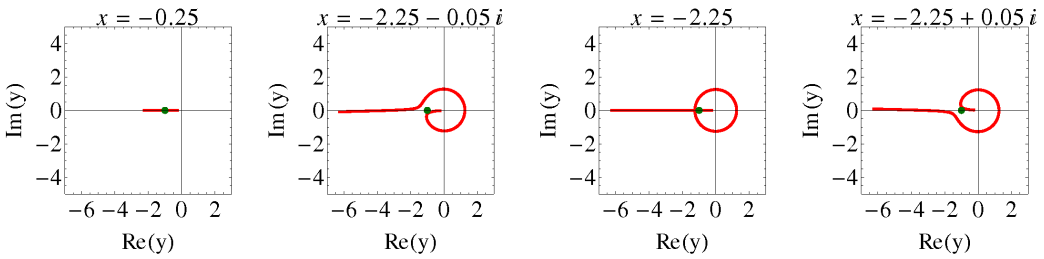

Figure E.1: The plot to the very left shows the analytic structure in the y-plane for $x = -(m_1 - m_2)^2$, $m_1 = 0.5$ au, $m_2 = 1.0$ au. This point x is no branch point, as the contour is not affected by the structure in the y-plane. The remaining plots show the analytic properties of the y-plane slightly below, at, and slightly above the point $x = -(m_1 + m_2)^2$, $m_1 = 0.5$ au, $m_2 = 1.0$ au. This point is a branch point, as the contour cannot connect the origin with the UV cut-off without hitting the cut and picking up its discontinuity.

This is in agreement with the solutions provided by [172, 173, 107] if applied to the Euclidean case, that is, using negative mass squares:

$$x = -(m_1 + m_2)^2 = \left(i\sqrt{m_1^2} + i\sqrt{m_2^2}\right)^2 = \left(\sqrt{-m_1^2} + \sqrt{-m_2^2}\right)^2 . \quad \text{(E.6)}$$

Appendix F

Numerical evaluation of 1-loop terms in the complex plane

Working in four Euclidean dimensions, a one-loop expression might be written as

$$\mathscr{G}\left(p^2\right) = \int_{\mathbb{R}^4} \frac{d^4k}{\left(2\pi\right)^4} \mathscr{F}\left(p^2, k^2, p\cdot k\right), \tag{F.1}$$

with $\mathscr{F}\left(p^2, k^2, p\cdot k\right)$ the integrand as a function of the external and loop momentum squared, p^2 and k^2, and their scalar product $p\cdot k$. Formulating the task is simple: evaluate expression (F.1) for $p^2 \in \mathbb{C}$ numerically. Here we provide the procedure we developed to evaluate expressions of that type. Each of the steps in this procedure bears a label marking it as being a task to be either performed analytically 'A' or numerically 'N'.

- STEP 1 (A) : (*Hyper-spherical coordinates*) As we are seeking a solution for a one-loop integral in four Euclidean dimensions we can employ hyper-spherical coordinates and remove the two trivial angles,

$$\begin{aligned}\int_{\mathbb{R}^4} \frac{d^4k}{\left(2\pi\right)^4} &\overset{(A.7)}{\rightarrow} \frac{1}{2\left(2\pi\right)^4}\int_0^{2\pi} d\phi \int_0^{\infty} dy\; y \int_{-1}^{1} dz\sqrt{1-z^2}\int_1^1 dw \\ &= \frac{1}{\left(2\pi\right)^3}\int_0^{\infty} dy\; y \int_{-1}^{1} dz\sqrt{1-z^2},\end{aligned} \tag{F.2}$$

  which we can apply to expression (F.1) to find

$$\mathscr{G}\left(x\right) = \frac{1}{\left(2\pi\right)^3}\int_0^{\infty} dy\; y \int_{-1}^{1} dz\sqrt{1-z^2}\mathscr{F}\left(x, y, \sqrt{x}\sqrt{y}z\right), \tag{F.3}$$

  where we have used the abbreviations $p^2 = x,\ k^2 = y$ and $\cos\measuredangle_{p,k} = z$.

- STEP 2 (A): (*Regularization*) The one-loop integral (F.1) might be a divergent quantity (otherwise one can proceed with STEP 3). Power-counting reveals the superficial degree of divergence, that might be removed in the spirit of BPHZ [40, 41, 42]. Let the superficial degree of divergence be n. The regularized expression is then obtained by employing a Taylor subtraction operator t^n to the integrand $\mathscr{F}$ of the divergent integral, where t^n is given by

$$t^n = \sum_{i=0}^{n} \frac{x^i}{i!} \left[\frac{\partial_i}{\partial x^{\hat{i}}} \right]_{x=0} . \tag{F.4}$$

  The regularized integrand can be written as

$$\mathscr{F}_{sub}\left(x, y, \sqrt{x}\sqrt{y}z\right) = \left(1 - t^n\right) \mathscr{F}\left(x, y, \sqrt{x}\sqrt{y}z\right) . \tag{F.5}$$

  After this step has been performed, we are left with

$$\mathscr{G}_{sub}\left(x\right) = \frac{1}{\left(2\pi\right)^3} \int_0^{\Lambda^2} dy\ y \int_{-1}^{1} dz \sqrt{1-z^2} \mathscr{F}_{sub}\left(x, y, \sqrt{x}\sqrt{y}z\right) , \tag{F.6}$$

  where we also replaced the upper integration boundary by some finite cut-off Λ^2. This is legitimate, as the BPHZ procedure removes any cut-off dependence from the regularized expression.

- STEP 3 (A,N): (*Analysis of the integrand*) In this step one has to analyze the analytic structure in the complex plane of the radial integration variable. Usually, a non-trivial (obstructive) structure arises through the angular integration in the variable z. For a given $x \in \mathbb{C}$, a branch cut might show up in the complex plane of the radial integration variable (see Appendix D to learn how this comes about). This branch cuts change their shape, size and orientation with varying external momentum square x, so eventually they spoil the validity of an undeformed contour along the real axis that connects the origin with the UV cut-off. A parametrization of the branch cut can be obtained by following the procedure outlined in Appendix D, but one can also perform this step numerically. In the main text we show results obtained by both procedures. After identification of regions in the complex plane where the radial contour has to be modified, this step leaves us with

$$\mathscr{G}_{sub}\left(x\right) = \frac{1}{\left(2\pi\right)^3} \int_{\mathscr{C}} dy\ y \int_{-1}^{1} dz \sqrt{1-z^2} \mathscr{F}_{sub}\left(x, y, \sqrt{x}\sqrt{y}z\right) , \tag{F.7}$$

  with $\mathscr{C}$ an appropriate contour.

- STEP 4 (N): (*Initialization*) Following the previous steps we are finally left with equation (F.7). In this step we have to initialize the grid of external nodes stored in an $L = (M \times N, \mathbb{C})$ matrix, where M and N are the number of grid points in the real and imaginary direction respectively. In our approach this step is performed on a GPU [98]. Furthermore one has to define and initialize all contour deformations resulting from the previous step.

- STEP 5 (N): (*Evaluation*) In this final step the integrations are performed using a GPU. For every given grid point $x \in L$ we evaluate equation (F.7) by using non-adaptive quadrature rules for the integrals. Subsets of the matrix L are evaluated in parallel on the GPU, where the architecture of the GPU determines the maximal size of the subset.

The tremendous level of parallelization provided by the GPU allowed us to sample the integrand with a very high level of accuracy, which becomes important if one wants to resolve a branch point (see example in main text).

Appendix G

Constructing the $\mathbf{F^2}$ correlator

In this section we construct an expression for $\langle F^2(x)F^2(0)\rangle$, which corresponds to a scalar glueball (0^{++}). The expression we are after can be found in [100], however, we derive it here and find agreement with their result. To this end we are solely operating at the Born level, that is, we turn off the non-Abelian term by putting the coupling to zero. The field strength tensor becomes

$$F^a_{\mu\nu} = \partial\mu A^a\nu - \partial\nu A^a\mu, \tag{G.1}$$

such that the correlator of F^2 reads

$$\langle F^2(x)F^2(0)\rangle_d = \langle \left(\partial\mu A^a\nu - \partial\nu A^a\mu\right)^2(x)\left(\partial\mu A^a\nu - \partial\nu A^a\mu\right)^2(0)\rangle_d. \tag{G.2}$$

As we are working in Euclidean momentum space, we are looking for a momentum space operator $\mathscr{O}_d\left(p^2\right)$ that corresponds to (G.2) ,

$$\langle F^2(x)F^2(0)\rangle_d = \int \frac{d^dp}{(2\pi)^4}\exp\left\{i\ p\cdot x\right\}\mathscr{O}_d\left(p^2\right). \tag{G.3}$$

Omitting the space and color labels, as well as considering only one of the two squares on the left hand side of (G.3), we have

$$\begin{aligned} F^2 &= \left(\partial\mu A\nu - \partial\nu A\mu\right)\left(\partial\mu A\nu - \partial\nu A\mu\right) \qquad (G.4)\\ &= \left(\partial_\mu A_\nu\right)\left(\partial_\mu A_\nu\right) - \left(\partial_\mu A_\nu\right)\left(\partial_\nu A_\mu\right) - \left(\partial_\nu A_\mu\right)\left(\partial_\mu A_\nu\right) + \left(\partial_\nu A_\mu\right)\left(\partial_\nu A_\mu\right)\\ &= 2\left(\partial_\mu A_\nu\right)\left(\partial_\mu A_\nu\right) - 2\left(\partial_\mu A_\nu\right)\left(\partial_\nu A_\mu\right), \end{aligned}$$

where the Einstein sum convention applies. Diagonal terms ($\mu = \nu$) vanish because of the $'-'$ sign, so we only have to consider terms where $\mu \neq \nu$.

Reintroducing the space and color dependence we take two squares appearing in expression (G.2), where each square is expressed as in the last line of (G.4), we have

$$\begin{aligned}
&\lim_{y\to 0}\Big\langle \left[2\left(\partial_{\mu,x}A^a_\nu(x)\right)\left(\partial_{\mu,x}A^a_\nu(x)\right)-2\left(\partial_{\mu,x}A^a_\nu(x)\right)\left(\partial_{\nu,x}A^a_\mu(x)\right)\right] \\
&\quad\times\left[2\left(\partial_{\rho,y}A^b_\sigma(y)\right)\left(\partial_{\rho,y}A^b_\sigma(y)\right)-2\left(\partial_{\rho,y}A^b_\sigma(y)\right)\left(\partial_{\sigma,y}A^b_\rho(y)\right)\right]\Big\rangle \\
=\;&\lim_{y\to 0}\Big(4\Big\langle\left(\partial_{\mu,x}A^a_\nu(x)\right)\left(\partial_{\mu,x}A^a_\nu(x)\right)\left(\partial_{\rho,y}A^b_\sigma(y)\right)\left(\partial_{\rho,y}A^b_\sigma(y)\right)\Big\rangle \\
&\quad-4\Big\langle\left(\partial_{\mu,x}A^a_\nu(x)\right)\left(\partial_{\mu,x}A^a_\nu(x)\right)\left(\partial_{\rho,y}A^b_\sigma(y)\right)\left(\partial_{\sigma,y}A^b_\rho(y)\right)\Big\rangle \\
&\quad-4\Big\langle\left(\partial_{\mu,x}A^a_\nu(x)\right)\left(\partial_{\nu,x}A^a_\mu(x)\right)\left(\partial_{\rho,y}A^b_\sigma(y)\right)\left(\partial_{\rho,y}A^b_\sigma(y)\right)\Big\rangle \\
&\quad+4\Big\langle\left(\partial_{\mu,x}A^a_\nu(x)\right)\left(\partial_{\nu,x}A^a_\mu(x)\right)\left(\partial_{\rho,y}A^b_\sigma(y)\right)\left(\partial_{\sigma,y}A^b_\rho(y)\right)\Big\rangle\Big).
\end{aligned} \tag{G.5}$$

The overall structure of terms appearing in (G.5) can be described in a general way by writing

$$\begin{aligned}
\mathscr{T}^{ab}_{\alpha\beta\gamma\delta\epsilon\zeta\eta\theta}(x,y) &= \\
&= \Big\langle\left(\partial_{\alpha,x}A^a_\beta(x)\right)\left(\partial_{\gamma,x}A^a_\delta(x)\right)\left(\partial_{\epsilon,y}A^b_\zeta(y)\right)\left(\partial_{\eta,y}A^b_\theta(y)\right)\Big\rangle,
\end{aligned} \tag{G.6}$$

which will become useful later. Expanding a 4-point function to zeroth order in the coupling g yields

$$\begin{aligned}
\langle\phi(x_1)\,\phi(x_2)\,\phi(x_3)\,\phi(x_4)\rangle &= \langle\phi(x_1)\,\phi(x_2)\rangle\langle\phi(x_3)\,\phi(x_4)\rangle \\
&+ \langle\phi(x_1)\,\phi(x_3)\rangle\langle\phi(x_2)\,\phi(x_4)\rangle \\
&+ \langle\phi(x_1)\,\phi(x_4)\rangle\langle\phi(x_2)\,\phi(x_3)\rangle \\
&+ \mathcal{O}(g).
\end{aligned} \tag{G.7}$$

Using this expansions and taking only connected terms in x into account, we find

$$\begin{aligned}
\mathscr{T}^{ab}_{\alpha\beta\gamma\delta\epsilon\zeta\eta\theta}(x,y) &= \\
&= \Big\langle\left(\partial_{\alpha,x}A^a_\beta(x)\right)\left(\partial_{\epsilon,y}A^b_\zeta(y)\right)\Big\rangle\Big\langle\left(\partial_{\gamma,x}A^a_\delta(x)\right)\left(\partial_{\eta,y}A^b_\theta(y)\right)\Big\rangle \\
&+ \Big\langle\left(\partial_{\alpha,x}A^a_\beta(x)\right)\left(\partial_{\eta,y}A^b_\theta(y)\right)\Big\rangle\Big\langle\left(\partial_{\gamma,x}A^a_\delta(x)\right)\left(\partial_{\epsilon,y}A^b_\zeta(y)\right)\Big\rangle.
\end{aligned} \tag{G.8}$$

According to this prescription we can now decompose the terms of equation (G.5), such that each of the 4-point functions making their appearance

there is written in terms of two products of two-point functions. This allows us to insert a transverse gluon propagator $D^{ab}_{\mu\nu}(x-y)$ for the two point functions. Following this procedure, we get

$$\begin{aligned}
\partial_{\alpha,x}\partial_{\beta,y}\underbrace{\left\langle A^a_\gamma(x)\,A^b_\delta(y)\right\rangle}_{D^{ab}_{\gamma\delta}(x-y)} &= \qquad\qquad (G.9)\\
&= \partial_{\alpha,x}\partial_{\beta,y}\int\frac{d^Dk}{(2\pi)^D}\exp\left\{i\,(x-y)\cdot k\right\}D^{ab}_{\gamma\delta}(k)\\
&= \int\frac{d^Dk}{(2\pi)^D}\exp\left\{i\,(x-y)\cdot k\right\}\underbrace{(ik_\alpha)\,(-ik_\beta)}_{k_\alpha k_\beta}D^{ab}_{\gamma\delta}(k)\\
&= \int\frac{d^Dk}{(2\pi)^D}\exp\left\{i\,(x-y)\cdot k\right\}k_\alpha k_\beta\\
&\quad\times\delta^{ab}\left(\delta^{\gamma\delta}-\frac{k_\gamma k_\delta}{k^2}\right)\mathscr{G}(k)
\end{aligned}$$

where we introduced the transverse projector and the scalar part of the gluon propagator, which is denoted by $\mathscr{G}(k)$. In each of the two terms of the building block (G.8) we have a product of two terms of the form (G.9), thus we have to introduce two integrations. The integrand (without the integral kernels of the Fourier transforms) $\tilde{I}^{ab}_{\alpha\beta\gamma\delta\epsilon\zeta\eta\theta}(x,y,k,q)$ of this most general building block is then given by

$$\begin{aligned}
\tilde{I}^{ab}_{\alpha\beta\gamma\delta\epsilon\zeta\eta\theta}(k,q) &= \qquad\qquad (G.10)\\
&= \left(\partial_{\alpha,x}\partial_{\epsilon,y}D^{ab}_{\beta\zeta}(x-y)\right)\left(\partial_{\gamma,x}\partial_{\eta,y}D^{ab}_{\delta\theta}(x-y)\right)\\
&\quad+\left(\partial_{\alpha,x}\partial_{\eta,y}D^{ab}_{\beta\theta}(x-y)\right)\left(\partial_{\gamma,x}\partial_{\epsilon,y}D^{ab}_{\delta\zeta}(x-y)\right)\\
&= \delta^{ab}\mathscr{G}\left(k^2\right)\mathscr{G}\left(q^2\right)\left[\left(k_\alpha k_\epsilon\left(\delta^{\beta\zeta}-\frac{k_\beta k_\zeta}{k^2}\right)\right)\right.\\
&\quad\times\left(q_\gamma q_\eta\left(\delta^{\delta\theta}-\frac{q_\delta q_\theta}{q^2}\right)\right)\\
&\quad+\left.\left(k_\alpha k_\eta\left(\delta^{\beta\theta}-\frac{k_\beta k_\theta}{k^2}\right)\right)\left(q_\gamma q_\epsilon\left(\delta^{\delta\zeta}-\frac{q_\delta q_\zeta}{q^2}\right)\right)\right].
\end{aligned}$$

Now we rewrite (G.10) by introducing an auxiliary tensor $\mathscr{A}$ that expresses the most general building block (G.8) of equation (G.5) by making use of expression (G.10). Note that the order of the indices is crucial here, as it determines whether an index goes with k or q. We get

$$
\begin{aligned}
&\mathscr{A}^{ab}_{\alpha\beta\gamma\delta\epsilon\zeta\eta\theta}(k,q) = \qquad\qquad (G.11)\\
&= \delta^{ab}\mathscr{G}(k)\mathscr{G}(q)k_\alpha q_\gamma\left[k_\epsilon q_\eta\delta^{\beta\zeta}\delta^{\delta\theta}+k_\eta q_\epsilon\delta^{\beta\theta}\delta^{\delta\zeta}\right.\\
&- \frac{1}{q^2}\left(k_\epsilon q_\eta q_\delta q_\theta\delta^{\beta\zeta}+k_\eta q_\epsilon q_\delta q_\zeta\delta^{\beta\theta}\right)\\
&- \left.\frac{1}{k^2}\left(k_\epsilon k_\beta k_\zeta q_\eta\delta^{\delta\theta}+k_\eta k_\beta k_\theta q_\epsilon\delta^{\delta\zeta}\right)+\frac{1}{k^2q^2}\left(k_\epsilon k_\beta k_\zeta q_\eta q_\delta q_\theta+k_\eta k_\beta k_\theta q_\epsilon q_\delta q_\zeta\right)\right].
\end{aligned}
$$

Expression (G.11) can now be used to write down the integrand (without the integral kernels of the Fourier transform) in d Euclidean dimensions,where we make the summation of indices explicit,

$$
\begin{aligned}
I^d(x,y,k,q) &= 4\sum_{\mu=1}^{d}\sum_{\nu=1}^{d}\sum_{\rho=1}^{d}\sum_{\sigma=1}^{d}\left(\mathscr{A}^{ab}_{\mu\nu\mu\nu\rho\sigma\rho\sigma}(k,q)\right. \qquad (G.12)\\
&\quad -\mathscr{A}^{ab}_{\mu\nu\mu\nu\rho\sigma\sigma\rho}(k,q)\\
&\quad \left.-\mathscr{A}^{ab}_{\mu\nu\nu\mu\rho\sigma\rho\sigma}(k,q)+\mathscr{A}^{ab}_{\mu\nu\nu\mu\rho\sigma\sigma\rho}(k,q)\right).
\end{aligned}
$$

Because of symmetries among the indices appearing in this expression one can easily work out the combinations to find that the expression for $\mathscr{A}$ reduces to

$$
\begin{aligned}
&\mathscr{A}^{ab,sym}_{\alpha\beta\gamma\delta\epsilon\zeta\eta\theta}(k,q) = \qquad\qquad (G.13)\\
&= \delta^{ab}\mathscr{G}(k)\mathscr{G}(q)k_\alpha q_\gamma\left[k_\epsilon q_\eta\delta^{\beta\zeta}\delta^{\delta\theta}+k_\eta q_\epsilon\delta^{\beta\theta}\delta^{\delta\zeta}\right].
\end{aligned}
$$

This step can be verified either by hand or by using a computer algebra system. For example, using FORM [89] one only needs a few lines to show that the expressions (G.11) and (G.13) for the indices appearing in (G.12) give the same result, see Listings G.1 and G.2 for the FORM code and the result respectively.

```
1 Dimension 10;
2 On statistics;
3 Vector k,q;
4 Indices alpha,beta,gamma,delta,eps,zeta,eta,theta,mu,nu,rho,
     sigma;
5 Symbols ook2,ooq2,ookpq2,Gk2,Gq2;
6 Local masterterm1 = 4*Gk2*Gq2*k(alpha)*q(gamma)*(k(eta)*q(eps
     )*d_(beta,theta)*d_(delta,zeta)+k(eps)*q(eta)*d_(beta,zeta
     )*d_(delta,theta)-ooq2*(k(eta)*q(delta)*q(zeta)*q(eps)*d_(
```

```
    beta,theta)+k(eps)*q(delta)*q(eta)*q(theta)*d_(beta,zeta))
    -ook2*(k(beta)*k(eta)*k(theta)*q(eps)*d_(delta,zeta)+k(
    beta)*k(zeta)*k(eps)*q(eta)*d_(delta,theta))+ookpq2*(k(
    beta)*k(eta)*k(theta)*q(delta)*q(zeta)*q(eps) +k(beta)*k(
    zeta)*k(eps)*q(delta)*q(eta)*q(theta)));
Local masterterm2 = 4*Gk2*Gq2*k(alpha)*q(gamma)*(k(eta)*q(eps
    )*d_(beta,theta)*d_(delta,zeta)+k(eps)*q(eta)*d_(beta,zeta
    )*d_(delta,theta));
Local term11 = (d_(alpha,mu)*d_(beta,nu)*d_(gamma,mu)*d_(
    delta,nu)*d_(eps,rho)*d_(zeta,sigma)*d_(eta,rho)*d_(theta,
    sigma))*masterterm1; Local term12 = (d_(alpha,mu)*d_(beta,
    nu)*d_(gamma,mu)*d_(delta,nu)*d_(eps,rho)*d_(zeta,sigma)*
    d_(eta,sigma)*d_(theta,rho))*masterterm1; Local term13 = (
    d_(alpha,mu)*d_(beta,nu)*d_(gamma,nu)*d_(delta,mu)*d_(eps,
    rho)*d_(zeta,sigma)*d_(eta,rho)*d_(theta,sigma))*
    masterterm1; Local term14 = (d_(alpha,mu)*d_(beta,nu)*d_(
    gamma,nu)*d_(delta,mu)*d_(eps,rho)*d_(zeta,sigma)*d_(eta,
    sigma)*d_(theta,rho))*masterterm1;
Local term21 = (d_(alpha,mu)*d_(beta,nu)*d_(gamma,mu)*d_(
    delta,nu)*d_(eps,rho)*d_(zeta,sigma)*d_(eta,rho)*d_(theta,
    sigma))*masterterm2; Local term22 = (d_(alpha,mu)*d_(beta,
    nu)*d_(gamma,mu)*d_(delta,nu)*d_(eps,rho)*d_(zeta,sigma)*
    d_(eta,sigma)*d_(theta,rho))*masterterm2; Local term23 = (
    d_(alpha,mu)*d_(beta,nu)*d_(gamma,nu)*d_(delta,mu)*d_(eps,
    rho)*d_(zeta,sigma)*d_(eta,rho)*d_(theta,sigma))*
    masterterm2; Local term24 = (d_(alpha,mu)*d_(beta,nu)*d_(
    gamma,nu)*d_(delta,mu)*d_(eps,rho)*d_(zeta,sigma)*d_(eta,
    sigma)*d_(theta,rho))*masterterm2;
Local total1 = (term11 - term12 - term13 + term14);
Local total2 = (term21 - term22 - term23 + term24);
Print +s, total1,total2;
.end
```

Listing G.1: A simple FORM code that shows the reduction from (G.11) to (G.13), here for 10 dimensions.

The result of the simple program shown in Listing G.1 is given in Listing G.2.

```
   total1 =         + 8*k.k*q.q*Gk2*Gq2         + 64*k.q^2*Gk2*
      Gq2       ;
   total2 =         + 8*k.k*q.q*Gk2*Gq2         + 64*k.q^2*Gk2*
      Gq2       ;
```

Listing G.2: The result of the code in Listing G.1.

Here we made an arbitrary choice of the Euclidean space-time dimension by putting it to 10. Using the simplified expression (G.13), one can immediately calculate the d-dimensional integrand of the Fourier transform. To this

end it is convenient to introduce a table showing the relation of the indices, see Table G.1.

term	sign	α	β	γ	δ	ϵ	ζ	η	θ
1	+	μ	ν	μ	ν	ρ	σ	ρ	σ
2	-	μ	ν	μ	ν	ρ	σ	σ	ρ
3	-	μ	ν	ν	μ	ρ	σ	ρ	σ
4	+	μ	ν	ν	μ	ρ	σ	σ	ρ

Table G.1: Indices to insert in equation (G.13) to obtain the d-dimensional integrand (G.12).

The integrand becomes

$$
\begin{aligned}
I^d(k,q) &= 4\sum_{\mu=1}^{d}\sum_{\nu=1}^{d}\sum_{\rho=1}^{d}\sum_{\sigma=1}^{d}\big(A^{ab,sym}_{\mu\nu\mu\nu\rho\sigma\rho\sigma}(k,q) \\
&\quad -A^{ab,sym}_{\mu\nu\mu\nu\rho\sigma\sigma\rho}(k,q) - A^{ab,sym}_{\mu\nu\nu\mu\rho\sigma\rho\sigma}(k,q) + A^{ab,sym}_{\mu\nu\nu\mu\rho\sigma\sigma\rho}(k,q)\big) \\
&= 4\delta^{ab}\mathscr{G}(k)\mathscr{G}(q)\sum_{\mu=1}^{d}\sum_{\nu=1}^{d}\sum_{\rho=1}^{d}\sum_{\sigma=1}^{d}[k_\mu q_\mu(k_\rho q_\rho\delta^{\nu\sigma}\delta^{\nu\sigma} + k_\rho q_\rho\delta^{\nu\sigma}\delta^{\nu\sigma}) \\
&\quad -k_\mu q_\mu(k_\rho q_\sigma\delta^{\nu\sigma}\delta^{\nu\rho} + k_\sigma q_\rho\delta^{\nu\rho}\delta^{\nu\sigma}) \\
&\quad -k_\mu q_\nu(k_\rho q_\rho\delta^{\nu\sigma}\delta^{\mu\sigma} + k_\rho q_\rho\delta^{\nu\sigma}\delta^{\mu\sigma}) \\
&\quad +k_\mu q_\nu(k_\rho q_\sigma\delta^{\nu\sigma}\delta^{\mu\rho} + k_\sigma q_\rho\delta^{\nu\rho}\delta^{\mu\sigma})] \\
&= 4\delta^{ab}\mathscr{G}(k)\mathscr{G}(q)\left[2(k\cdot q)^2 d - 2(k\cdot q)^2 - 2(k\cdot q)^2 + 2k^2q^2\right] \\
&= 8\delta^{ab}\mathscr{G}(k)\mathscr{G}(q)\left[k^2q^2 + (d-2)(k\cdot q)^2\right],
\end{aligned}
\tag{G.14}
$$

which is the final result that holds for arbitrary Euclidean dimensions $d \geq 2$. With the trace in color space N_C we can finally obtain the desired

integral corresponding to the momentum space operator $\mathscr{O}(p)$,

$$\begin{aligned}
&\left\langle F^2(x)F^2(0)\right\rangle = \qquad\qquad (G.15)\\
= \;& 8N_C \int \frac{d^dk}{(2\pi)^d} \int \frac{d^dq}{(2\pi)^d} \exp\left\{i\left(k+q\right)\cdot x\right\}\\
= \;& \times \mathscr{G}\left(k\right)\mathscr{G}\left(q\right)\left(k^2q^2 + \left(d-2\right)\left(k\cdot q\right)^2\right)\\
= \;& \Big| q = p-k \Big|\\
= \;& 8N_C \int \frac{d^dp}{(2\pi)^d} \exp\left\{ip\cdot x\right\}\\
& \underbrace{\times \int \frac{d^dk}{(2\pi)^d} \mathscr{G}\left(k\right)\mathscr{G}\left(p-k\right)\left(k^2\left(p-k\right)^2 + \left(d-2\right)\left(k\cdot\left(p-k\right)\right)^2\right)}_{=\mathscr{O}(p^2)},
\end{aligned}$$

such that the final expression is

$$\mathscr{O}\left(p^2\right) = \int \frac{d^dk}{(2\pi)^d} \mathscr{G}\left(k^2\right)\mathscr{G}\left(\left(p-k\right)^2\right)\left(k^2\left(p-k\right)^2 + \left(d-2\right)\left(k\cdot\left(p-k\right)\right)^2\right), \tag{G.16}$$

where we expressed the momentum dependence of the scalar parts of the gluons ($\mathscr{G}$) in terms of momentum squares.

Appendix H

Calculations in the DFS phase

Here we present the details of the calculation discussed in Section 5.2 of Chapter 5. Let us start by showing that equation (5.1) indeed follows with the definitions (5.3) and (5.4).

$$
\begin{aligned}
\mu_f &= \bar{\mu}_f \left[1 + (\varepsilon_S \pm \varepsilon_A)\cos^2\vartheta\right] \qquad \text{(H.1)}\\
&= \left(\mu_{f,0} - \frac{1}{2}\mu_{f,2}\right)\\
&\quad \times \left[1 + \left(\frac{3}{4}\left(\frac{\mu_{d,2}}{\bar{\mu}_d} + \frac{\mu_{u,2}}{\bar{\mu}_u}\right)\right.\right.\\
&\quad \left.\left. \pm \frac{3}{4}\left(\frac{\mu_{d,2}}{\bar{\mu}_d} - \frac{\mu_{u,2}}{\bar{\mu}_u}\right)\right)\cos^2\vartheta\right]\\
&= \left(\mu_{f,0} - \frac{1}{2}\mu_{f,2}\right)\left[1 + \frac{3}{2}\left(\frac{\mu_{f,2}}{\bar{\mu}_f}\right)\cos^2\vartheta\right]\\
&= \left(\mu_{f,0} - \frac{1}{2}\mu_{f,2}\right)\left[1 + \frac{3}{2}\left(\frac{\mu_{f,2}}{\mu_{f,0} - \frac{1}{2}\mu_{f,2}}\right)\cos^2\vartheta\right]\\
&= \mu_{f,0} - \frac{1}{2}\mu_{f,2} + \frac{3}{2}\left(\frac{\mu_{f,0}\mu_{f,2}}{\mu_{f,0} - \frac{1}{2}\mu_{f,2}}\right)\cos^2\vartheta\\
&\quad -\frac{3}{4}\left(\frac{\mu_{f,2}^2}{\mu_{f,0} - \frac{1}{2}\mu_{f,2}}\right)\cos^2\vartheta\\
&= \mu_{f,0} + \frac{1}{2}\mu_{f,2}\left[-1 + 3\left(\frac{\mu_{f,0} - \frac{1}{2}\mu_{f,2}}{\mu_{f,0} - \frac{1}{2}\mu_{f,2}}\right)\cos^2\vartheta\right]\\
&= \mu_{f,0} + \frac{1}{2}\mu_{f,2}\left[3\cos^2\vartheta - 1\right],
\end{aligned}
$$

which shows that the definitions are consistent. The particle number density of the ellipsoidal Fermi surfaces is given in (5.7). Performing two of the three integrals we get

$$
\begin{aligned}
n_f &= \frac{C\ k_{F,f}^3}{(2\pi)^2 3}\int_0^\pi d\vartheta\left[\left(1+(\varepsilon_S\pm\varepsilon_A)\sin^2\vartheta\right)^3\sin\vartheta\right] \qquad \text{(H.2)}\\
&= \frac{C\ k_{F,f}^3}{(2\pi)^2 3}\int_0^\pi d\vartheta\sin\vartheta\left[\sum_{k=0}^{3}\left(\begin{array}{c}3\\k\end{array}\right)\right.\\
&\quad \left.\times(\varepsilon_S\pm\varepsilon_A)^{3-k}\sin^{2k}\vartheta\right]\\
&= \frac{C\ k_{F,f}^3}{(2\pi)^2 3}\int_0^\pi d\vartheta\sin\vartheta\left[1+3(\varepsilon_S\pm\varepsilon_A)\sin^2\vartheta\right.\\
&\quad \left.+3(\varepsilon_S\pm\varepsilon_A)^2\sin^4\vartheta+(\varepsilon_S\pm\varepsilon_A)^3\sin^6\vartheta\right]\\
&= \frac{C\ k_{F,f}^3}{(2\pi)^2 3}\int_0^\pi d\vartheta\left[\sin\vartheta+3(\varepsilon_S\pm\varepsilon_A)\sin^3\vartheta\right.\\
&\quad \left.+3(\varepsilon_S\pm\varepsilon_A)^2\sin^5\vartheta+(\varepsilon_S\pm\varepsilon_A)^3\sin^7\vartheta\right]
\end{aligned}
$$

Integrating the remaining term finally yields

$$
\begin{aligned}
n_f &= \frac{C\ k_{F,f}^3}{(2\pi)^2 3}\left[2+4(\varepsilon_S\pm\varepsilon_A)\right. \qquad \text{(H.3)}\\
&\quad \left.+\frac{16}{5}(\varepsilon_S\pm\varepsilon_A)^2+\frac{32}{35}(\varepsilon_S\pm\varepsilon_A)^3\right]\\
&= \frac{C\ k_{F,f}^3}{6\pi^2}\left[1+2(\varepsilon_S\pm\varepsilon_A)\right.\\
&\quad \left.+\frac{8}{5}(\varepsilon_S\pm\varepsilon_A)^2+\frac{16}{35}(\varepsilon_S\pm\varepsilon_A)^3\right].
\end{aligned}
$$

Next, let us calculate the energy density of the deformed case. The linear dispersion relation enters the integral together with the Jacobian. The momentum reads

$$
\begin{aligned}
|k| &= k_f\left(1+(\varepsilon_S\pm\varepsilon_A)\sin^2\vartheta\right) \qquad \text{(H.4)}\\
&\quad \times\left[\sin^2\vartheta\cos^2\varphi+\sin^2\vartheta\sin^2\varphi+\cos^2\vartheta\right]^{\frac{1}{2}}\\
&= k_f\left(1+(\varepsilon_S\pm\varepsilon_A)\sin^2\vartheta\right).,
\end{aligned}
$$

and the energy density becomes

$$
\begin{aligned}
u_f &= C \int \frac{d^3k_f}{(2\pi)^3} k_f^3 \left(1 + (\varepsilon_S \pm \varepsilon_A)\sin^2\vartheta\right)^4 \qquad \text{(H.5)} \\
&= \frac{C}{(2\pi)^3} \int_0^{k_{F,f}} dk_f \int_0^{\pi} d\vartheta \int_0^{2\pi} d\varphi k_f^3 \\
&\quad \times \sin\vartheta \left(1 + (\varepsilon_S \pm \varepsilon_A)\sin^2\vartheta\right)^4 \\
&= \frac{C}{(2\pi)^2} \frac{k_{F,f}^4}{4} \\
&\quad \times \int_0^{\pi} d\vartheta \sum_{k=0}^{4} \left(\begin{array}{c} 4 \\ k \end{array} \right) 1^{4-k} (\varepsilon_S \pm \varepsilon_A)^k \sin^{2k+1}\vartheta \\
&= \frac{C}{(2\pi)^2} \frac{k_{F,f}^4}{4} \int_0^{\pi} d\vartheta \left[\sin\vartheta + 4(\varepsilon_S \pm \varepsilon_A)\sin^3\vartheta \right. \\
&\quad +6(\varepsilon_S \pm \varepsilon_A)^2 \sin^5\vartheta + 4(\varepsilon_S \pm \varepsilon_A)^3 \sin^7\vartheta \\
&\quad \left. +(\varepsilon_S \pm \varepsilon_A)^4 \sin^9\vartheta\right] .
\end{aligned}
$$

Performing the integral we get

$$
\begin{aligned}
u_f &= \frac{C}{(2\pi)^2} \frac{k_{F,f}^4}{4} \left[2 + \frac{16}{3}(\varepsilon_S \pm \varepsilon_A) + \frac{96}{15}(\varepsilon_S \pm \varepsilon_A)^2 \right. \qquad \text{(H.6)} \\
&\quad \left. +\frac{128}{35}(\varepsilon_S \pm \varepsilon_A)^3 + \frac{256}{315}(\varepsilon_S \pm \varepsilon_A)^4\right] \\
&= \frac{C\ k_{F,f}^4}{8\pi^2} \left[1 + \frac{8}{3}(\varepsilon_S \pm \varepsilon_A) + \frac{48}{15}(\varepsilon_S \pm \varepsilon_A)^2 \right. \\
&\quad \left. +\frac{64}{35}(\varepsilon_S \pm \varepsilon_A)^3 + \frac{128}{315}(\varepsilon_S \pm \varepsilon_A)^4\right] .
\end{aligned}
$$

The 'costs' for the deformation in terms of the energy density reads

$$
\begin{aligned}
u_{deform} &= \frac{C\ k_{F,u}^4}{8\pi^2}\left[1+\frac{8}{3}(\varepsilon_S+\varepsilon_A)+\frac{48}{15}(\varepsilon_S+\varepsilon_A)^2\right. \\
&\quad \left.+\frac{64}{35}(\varepsilon_S+\varepsilon_A)^3+\frac{128}{315}(\varepsilon_S+\varepsilon_A)^4\right] \\
&\quad -\frac{C\ \left(k_{F,u}^{sph.}\right)^4}{8\pi^2} \\
&+ \frac{C\ k_{F,d}^4}{8\pi^2}\left[1+\frac{8}{3}(\varepsilon_S-\varepsilon_A)+\frac{48}{15}(\varepsilon_S-\varepsilon_A)^2\right. \\
&\quad \left.+\frac{64}{35}(\varepsilon_S-\varepsilon_A)^3+\frac{128}{315}(\varepsilon_S-\varepsilon_A)^4\right] \\
&\quad -\frac{C\ \left(k_{F,u}^{sph.}\right)^4}{8\pi^2}.
\end{aligned}
\tag{H.7}
$$

Next we have to re-adjust the optimal deformation parameter ε_A^{opt}.

$$
k_{F,u}\left(1+\varepsilon_A^{opt}\right) \stackrel{!}{=} k_{F,d}\left(1-\varepsilon_A^{opt}\right) \tag{H.8}
$$

$$
\begin{aligned}
\Rightarrow\ & \frac{k_{F,u,s}}{\left[1+2\varepsilon_A^{opt}+\frac{8}{5}\left(\varepsilon_A^{opt}\right)^2+\frac{16}{35}\left(\varepsilon_A^{opt}\right)^3\right]^{\frac{1}{3}}}\left(1+\varepsilon_A^{opt}\right) \\
\stackrel{!}{=}\ & \frac{k_{F,d,s}}{\left[1-2\varepsilon_A^{opt}+\frac{8}{5}\left(\varepsilon_A^{opt}\right)^2-\frac{16}{35}\left(\varepsilon_A^{opt}\right)^3\right]^{\frac{1}{3}}}\left(1-\varepsilon_A^{opt}\right)
\end{aligned}
\tag{H.9}
$$

$$
\begin{aligned}
\Leftrightarrow\ & \frac{k_{F,u,s}^3}{\left[1+2\varepsilon_A^{opt}+\frac{8}{5}\left(\varepsilon_A^{opt}\right)^2+\frac{16}{35}\left(\varepsilon_A^{opt}\right)^3\right]} \\
& \times\left(1+\left(\varepsilon_A^{opt}\right)^3+3\left(\varepsilon_A^{opt}\right)^2+3\varepsilon_A^{opt}\right) \\
\stackrel{!}{=}\ & \frac{k_{F,d,s}^3}{\left[1-2\varepsilon_A^{opt}+\frac{8}{5}\left(\varepsilon_A^{opt}\right)^2-\frac{16}{35}\left(\varepsilon_A^{opt}\right)^3\right]} \\
& \times\left(1-\left(\varepsilon_A^{opt}\right)^3+3\left(\varepsilon_A^{opt}\right)^2-3\varepsilon_A^{opt}\right)
\end{aligned}
\tag{H.10}
$$

$$
\begin{aligned}
\Leftrightarrow\quad & k_{F,u,s}^3 \left(1 - 2\varepsilon_A^{opt} + \frac{8}{5}\left(\varepsilon_A^{opt}\right)^2 - \frac{16}{35}\left(\varepsilon_A^{opt}\right)^3\right) \\
& \times \left(1 + \left(\varepsilon_A^{opt}\right)^3 + 3\left(\varepsilon_A^{opt}\right)^2 + 3\varepsilon_A^{opt}\right) \\
\stackrel{!}{=}\quad & k_{F,d,s}^3 \left(1 + 2\varepsilon_A^{opt} + \frac{8}{5}\left(\varepsilon_A^{opt}\right)^2 + \frac{16}{35}\left(\varepsilon_A^{opt}\right)^3\right) \\
& \times \left(1 - \left(\varepsilon_A^{opt}\right)^3 + 3\left(\varepsilon_A^{opt}\right)^2 - 3\varepsilon_A^{opt}\right)
\end{aligned}
\tag{H.11}
$$

$$
\begin{aligned}
\Leftrightarrow\quad & k_{F,u,s}^3 \left(1 - 2\varepsilon_A^{opt} + \frac{8}{5}\left(\varepsilon_A^{opt}\right)^2 - \frac{16}{35}\left(\varepsilon_A^{opt}\right)^3\right. \\
& +3\varepsilon_A^{opt} - 6\left(\varepsilon_A^{opt}\right)^2 + \frac{24}{5}\left(\varepsilon_A^{opt}\right)^3 - \frac{48}{35}\left(\varepsilon_A^{opt}\right)^4 \\
& +3\left(\varepsilon_A^{opt}\right)^2 - 6\left(\varepsilon_A^{opt}\right)^3 + \frac{24}{5}\left(\varepsilon_A^{opt}\right)^4 - \frac{48}{35}\left(\varepsilon_A^{opt}\right)^5 \\
& \left. + \left(\varepsilon_A^{opt}\right)^3 - 2\left(\varepsilon_A^{opt}\right)^4 + \frac{8}{5}\left(\varepsilon_A^{opt}\right)^5 - \frac{16}{35}\left(\varepsilon_A^{opt}\right)^6\right)
\end{aligned}
\tag{H.12}
$$

$$
\begin{aligned}
\Leftrightarrow\quad & k_{F,u,s}^3 \left(1 + \varepsilon_A^{opt} - \frac{7}{5}\left(\varepsilon_A^{opt}\right)^2 - \frac{23}{35}\left(\varepsilon_A^{opt}\right)^3\right. \\
& \left. + \frac{50}{35}\left(\varepsilon_A^{opt}\right)^4 + \frac{8}{35}\left(\varepsilon_A^{opt}\right)^5 - \frac{16}{35}\left(\varepsilon_A^{opt}\right)^6\right) \\
\stackrel{!}{=}\quad & k_{F,d,s}^3 \left(1 - \varepsilon_A^{opt} - \frac{7}{5}\left(\varepsilon_A^{opt}\right)^2 + \frac{23}{35}\left(\varepsilon_A^{opt}\right)^3\right. \\
& \left. + \frac{50}{35}\left(\varepsilon_A^{opt}\right)^4 - \frac{8}{35}\left(\varepsilon_A^{opt}\right)^5 - \frac{16}{35}\left(\varepsilon_A^{opt}\right)^6\right).
\end{aligned}
\tag{H.13}
$$

The optimal deformation parameter ε_A has to satisfy H.13, where we can safely neglect orders higher than linear in ε_A. As the expansion parameter for the squared term has the same sign on both sides, the next contribution depends on the (small) difference of the Fermi momenta cubed. The suppression of terms of order of 3 or higher due to the small parameter ε_A is obvious, such that we can safely neglect higher orders form here on. The modified condition for the optimal deformation parameter ε_A is then

$$
\begin{aligned}
k_{F,u,s}^3\left(1+\varepsilon_A^{opt}\right) &= k_{F,d,s}^3\left(1-\varepsilon_A^{opt}\right) && \text{(H.14)}\\
&\Rightarrow & \\
\varepsilon_A^{opt} &= \frac{k_{F,d,s}^3 - k_{F,u,s}^3}{k_{F,d,s}^3 + k_{F,u,s}^3} && \text{(H.15)}\\
&= \frac{(\mu+\delta\mu)^3 - (\mu-\delta\mu)^3}{(\mu+\delta\mu)^3 + (\mu-\delta\mu)^3} & \\
&= \frac{6\mu^2(\delta\mu) + 2(\delta\mu)^3}{2\mu^3 + 6\mu(\delta\mu)^2} & \\
&\approx 3\frac{\delta\mu}{\mu} &
\end{aligned}
$$

We also confirmed this result by solving the system numerically in a self-consistent way.

Appendix I

Details of the bosonization

In this Appendix we show that the four fermion interaction c_4 can be written as a bi-linear of two tensor fields,

$$\begin{aligned} c_4 &= \varepsilon_{ijkl}\psi_i\psi_j\psi_k\psi_l \\ &= \chi_i M_{ij}\chi_j, \end{aligned} \tag{I.1}$$

where M is a real symmetric non-singular matrix and χ are vectors storing the tensor fields ϕ_{ij} composed of two fermionic fields ψ_i and ψ_j. To this end consider the Levi-Civita tensor in the multi-index notation involving i, j, k and l. In total there are $4! = 24$ non-trivial contributions. The idea is to use the anti-symmetry of the Levi-Civita-symbol to re-arrange the terms in such a way that they can be reduced to multiples of the 6 non-vanishing combinations in the Levi-Civita tensor, see Table I.1.

	Θ_{12}	Θ_{13}	Θ_{14}	Θ_{23}	Θ_{24}	Θ_{34}	permutation
Θ_{12}	0	0	0	0	0	1	$sgn\,(1234) = +1$
Θ_{13}	0	0	0	0	-1	0	$sgn\,(1324) = -1$
Θ_{14}	0	0	0	1	0	0	$sgn\,(1423) = +1$
Θ_{23}	0	0	1	0	0	0	$sgn\,(2314) = +1$
Θ_{24}	0	-1	0	0	0	0	$sgn\,(2413) = -1$
Θ_{34}	1	0	0	0	0	0	$sgn\,(3412) = +1$

Table I.1: Non-vanishing pairing patterns after bosonization are used as a basis, see text.

The desired bi-linear form is then given by

$$\begin{aligned} &\tilde{\chi}.\tilde{M}.\tilde{\chi} = \\ &= \begin{pmatrix} \Theta_{12} \\ \Theta_{13} \\ \Theta_{14} \\ \Theta_{23} \\ \Theta_{24} \\ \Theta_{34} \end{pmatrix}^T \cdot \begin{pmatrix} 0 & 0 & 0 & 0 & 0 & 1 \\ 0 & 0 & 0 & 0 & -1 & 0 \\ 0 & 0 & 0 & 1 & 0 & 0 \\ 0 & 0 & 1 & 0 & 0 & 0 \\ 0 & -1 & 0 & 0 & 0 & 0 \\ 1 & 0 & 0 & 0 & 0 & 0 \end{pmatrix} \cdot \begin{pmatrix} \Theta_{12} \\ \Theta_{13} \\ \Theta_{14} \\ \Theta_{23} \\ \Theta_{24} \\ \Theta_{34} \end{pmatrix}, \end{aligned} \tag{I.2}$$

where $\tilde{M}$ is a real symmetric non-singular matrix. In order to cover all combinations occurring in the Levi-Civita tensor we make use of the anti-symmetry of the fermionic fields under exchange. The term $\varepsilon_{ijkl}\psi_i\psi_j\psi_k\psi_l$ can then be written in a bi-linear form of tensor fields ϕ_{ij},

$$\begin{aligned} &\begin{pmatrix} \tilde{\chi} \\ -\tilde{\chi} \end{pmatrix}^T \cdot \begin{pmatrix} \tilde{M} & -\tilde{M} \\ -\tilde{M} & \tilde{M} \end{pmatrix} \cdot \begin{pmatrix} \tilde{\chi} \\ -\tilde{\chi} \end{pmatrix} \\ = &\begin{pmatrix} \tilde{\chi} \\ -\tilde{\chi} \end{pmatrix}^T \cdot \begin{pmatrix} 2M.\tilde{\chi} \\ -2M.\tilde{\chi} \end{pmatrix} \\ = &\ \tilde{\chi}^T.4\tilde{M}.\tilde{\chi}, \end{aligned} \tag{I.3}$$

where the lower entry of the vector corresponds to the basis elements shown in Table I.1 with their indices flipped, hence the '-' sign. Let us discuss the bosonization in greater detail. The interaction we want to bosonize after the first Hubbard-Stratonovich transformation reads

$$\begin{aligned} &\exp\left\{-\int d^4x \mathscr{L}_{int}\right\} \\ = &\ \exp\left\{-\int d^4x \tilde{g}_4 \psi_i\psi_j T_{ijkl}\psi_k\psi_l\right\}. \end{aligned} \tag{I.4}$$

In order to use the bi linear form constructed above, the interaction term in the exponential on the right hand side of (I.4) has to be re-written in a suitable form. As the tensor T is totally antisymmetric, we may write

$$
\begin{aligned}
& \psi_i\psi_j T_{ijkl}\psi_k\psi_l \qquad\qquad (I.5)\\
= \quad & \varepsilon_{ijkl}\psi_i\psi_j\psi_k\psi_l \\
= \quad & \psi_1\psi_2\psi_3\psi_4 - \psi_1\psi_2\psi_4\psi_3 - \psi_1\psi_3\psi_2\psi_4 + \psi_1\psi_3\psi_4\psi_2 \\
+ \quad & \psi_1\psi_4\psi_2\psi_3 - \psi_1\psi_4\psi_3\psi_2 - \psi_2\psi_1\psi_3\psi_4 + \psi_2\psi_1\psi_4\psi_3 \\
+ \quad & \psi_2\psi_3\psi_1\psi_4 - \psi_2\psi_3\psi_4\psi_1 - \psi_2\psi_4\psi_1\psi_3 + \psi_2\psi_4\psi_3\psi_1 \\
+ \quad & \psi_3\psi_1\psi_2\psi_4 - \psi_3\psi_1\psi_4\psi_2 - \psi_3\psi_2\psi_1\psi_4 + \psi_3\psi_2\psi_4\psi_1 \\
+ \quad & \psi_3\psi_4\psi_1\psi_2 - \psi_3\psi_4\psi_2\psi_1 - \psi_4\psi_1\psi_2\psi_3 + \psi_4\psi_1\psi_3\psi_2 \\
+ \quad & \psi_4\psi_2\psi_1\psi_3 - \psi_4\psi_2\psi_3\psi_1 - \psi_4\psi_3\psi_1\psi_2 + \psi_4\psi_3\psi_2\psi_1.
\end{aligned}
$$

We want to express the interaction (I.5) in the basis shown in Table I.1, where the basis elements correspond to the six combinations

$$
\begin{aligned}
\mathcal{B}_1 &= +\psi_1\psi_2\psi_3\psi_4, \qquad (I.6)\\
\mathcal{B}_2 &= -\psi_1\psi_3\psi_2\psi_4, \\
\mathcal{B}_3 &= +\psi_1\psi_4\psi_2\psi_3, \\
\mathcal{B}_4 &= +\psi_2\psi_3\psi_1\psi_4, \\
\mathcal{B}_5 &= -\psi_2\psi_4\psi_1\psi_3, \\
\mathcal{B}_6 &= +\psi_3\psi_4\psi_1\psi_2.
\end{aligned}
$$

Permuting the terms of (I.5) by shuffling each line to a certain basis element we get

$$
\begin{aligned}
& \psi_1\psi_2\psi_3\psi_4 + \psi_1\psi_2\psi_3\psi_4 + \psi_1\psi_2\psi_3\psi_4 + \psi_1\psi_2\psi_3\psi_4 \\
+ \quad & \psi_1\psi_4\psi_2\psi_3 + \psi_1\psi_4\psi_2\psi_3 + \psi_1\psi_4\psi_2\psi_3 + \psi_1\psi_4\psi_2\psi_3 \\
+ \quad & \psi_2\psi_3\psi_1\psi_4 + \psi_2\psi_3\psi_4\psi_1 + \psi_2\psi_3\psi_1\psi_4 + \psi_2\psi_3\psi_1\psi_4 \\
- \quad & \psi_1\psi_3\psi_2\psi_4 - \psi_1\psi_3\psi_2\psi_4 - \psi_1\psi_3\psi_2\psi_4 - \psi_1\psi_3\psi_2\psi_4 \\
+ \quad & \psi_3\psi_4\psi_1\psi_2 + \psi_3\psi_4\psi_1\psi_2 + \psi_3\psi_4\psi_1\psi_2 + \psi_3\psi_4\psi_1\psi_2 \\
- \quad & \psi_2\psi_4\psi_1\psi_3 - \psi_2\psi_4\psi_1\psi_3 - \psi_2\psi_4\psi_1\psi_3 - \psi_2\psi_4\psi_1\psi_3 \\
= \quad & 4\mathcal{B}_1 + 4\mathcal{B}_3 + 4\mathcal{B}_4 + 4\mathcal{B}_2 + 4\mathcal{B}_6 + 4\mathcal{B}_5 \qquad (I.7)\\
= \quad & 4\sum_{i=1}^{6}\mathcal{B}_i.
\end{aligned}
$$

For the interaction (I.4) we can now write

$$\begin{aligned} & \exp\left\{-\int d^4x \mathscr{L}_{int}\right\} \\ = \quad & \exp\left\{-\int d^4x \tilde{g}_4 4 \sum_{i=1}^{6} \mathcal{B}_i\right\}. \end{aligned} \tag{I.8}$$

This, in turn, allows us to perform the bosonization in a straight-forward way,

$$\begin{aligned} & \exp\left\{\int d^4x \left(-\tilde{g}_4\right) 4 \sum_{i=1}^{6} \mathcal{B}_i\right\} \\ \propto \quad & \int \prod_{\substack{m,n=1 \\ m<n}}^{6} \mathscr{D}\left[\Theta_{mn}\right] \exp\left\{-\int d^4x \frac{m_\Theta^2}{2} 4 \tilde{\chi}_i \tilde{M}_{ij} \tilde{\chi}_j\right\} \\ & \times \exp\left\{-\int d^4x g_\Theta^Y 4 \tilde{M}_{ij} \tilde{\chi}_i \psi_{j_1} \psi_{j_2}\right\}, \end{aligned} \tag{I.9}$$

where we used an implicit way to write down the bi-linear form and the Yukawa term for the new fields. However, now that we have the desired bosonic fields Θ_{ij} (in fact they are tensor fields carrying baryon number 0 and they obey Fermi statistics) we convert them back to an expression involving the Levi-Civita tensor. Making the last expression explicit in the indices of the bosonic fields, as well as using their antisymmetry under exchange of their indices, we have

$$
\begin{aligned}
& 4\tilde{\chi}_i \tilde{M}_{ij} \tilde{\chi}_j \qquad\qquad (\text{I.10}) \\
= \;& 4\,(\Theta_{12}\Theta_{34} - \Theta_{13}\Theta_{24} + \Theta_{14}\Theta_{23} \\
& + \Theta_{23}\Theta_{14} - \Theta_{24}\Theta_{13} + \Theta_{34}\Theta_{12}) \\
= \;& \Theta_{12}\Theta_{34} + \Theta_{12}\Theta_{34} + \Theta_{12}\Theta_{34} + \Theta_{12}\Theta_{34} \\
& - \Theta_{13}\Theta_{24} - \Theta_{13}\Theta_{24} - \Theta_{13}\Theta_{24} - \Theta_{13}\Theta_{24} \\
& + \Theta_{14}\Theta_{23} + \Theta_{14}\Theta_{23} + \Theta_{14}\Theta_{23} + \Theta_{14}\Theta_{23} \\
& + \Theta_{23}\Theta_{14} + \Theta_{23}\Theta_{14} + \Theta_{23}\Theta_{14} + \Theta_{23}\Theta_{14} \\
& - \Theta_{24}\Theta_{13} - \Theta_{24}\Theta_{13} - \Theta_{24}\Theta_{13} - \Theta_{24}\Theta_{13} \\
& + \Theta_{34}\Theta_{12} + \Theta_{34}\Theta_{12} + \Theta_{34}\Theta_{12} + \Theta_{34}\Theta_{12} \\
= \;& \Theta_{12}\Theta_{34} - \Theta_{21}\Theta_{34} - \Theta_{12}\Theta_{43} + \Theta_{21}\Theta_{43} \\
& - \Theta_{13}\Theta_{24} + \Theta_{31}\Theta_{24} + \Theta_{13}\Theta_{42} - \Theta_{31}\Theta_{42} \\
& + \Theta_{14}\Theta_{23} - \Theta_{41}\Theta_{23} - \Theta_{14}\Theta_{32} + \Theta_{41}\Theta_{32} \\
& + \Theta_{23}\Theta_{14} - \Theta_{32}\Theta_{14} - \Theta_{23}\Theta_{41} + \Theta_{32}\Theta_{41} \\
& - \Theta_{24}\Theta_{13} + \Theta_{42}\Theta_{13} + \Theta_{24}\Theta_{31} - \Theta_{42}\Theta_{31} \\
& + \Theta_{34}\Theta_{12} - \Theta_{43}\Theta_{12} - \Theta_{34}\Theta_{21} + \Theta_{43}\Theta_{21} \\
= \;& \Theta_{12}\Theta_{34} - \Theta_{12}\Theta_{43} - \Theta_{13}\Theta_{24} + \Theta_{13}\Theta_{42} \\
& + \Theta_{14}\Theta_{23} - \Theta_{14}\Theta_{32} - \Theta_{21}\Theta_{34} + \Theta_{21}\Theta_{43} \\
& + \Theta_{23}\Theta_{14} - \Theta_{23}\Theta_{41} - \Theta_{24}\Theta_{13} + \Theta_{24}\Theta_{31} \\
& + \Theta_{31}\Theta_{24} - \Theta_{31}\Theta_{42} - \Theta_{32}\Theta_{14} + \Theta_{32}\Theta_{41} \\
& + \Theta_{34}\Theta_{12} - \Theta_{34}\Theta_{21} - \Theta_{41}\Theta_{23} + \Theta_{41}\Theta_{32} \\
& + \Theta_{42}\Theta_{13} - \Theta_{42}\Theta_{31} - \Theta_{43}\Theta_{12} + \Theta_{43}\Theta_{21} \\
= \;& \varepsilon_{ijkl}\Theta_{ij}\Theta_{kl},
\end{aligned}
$$

where we just rearranged the terms in the same way as we got them when evaluating equation (I.5). Making also the last term in (I.9) explicit, we find

$$
\begin{aligned}
& 4\tilde{M}_{ij}\tilde{\chi}_i\psi_{j_1}\psi_{j_2} \qquad\qquad (\text{I.11}) \\
= \;& 4\,(\Theta_{12}\psi_3\psi_4 - \Theta_{13}\psi_3\psi_4 + \Theta_{14}\psi_3\psi_4 \\
& + \Theta_{23}\psi_3\psi_4 - \Theta_{24}\psi_3\psi_4 + \Theta_{34}\psi_3\psi_4) \\
= \;& \Big|\text{same calculation as (I.10)}\Big| \\
= \;& \varepsilon_{ijkl}\Theta_{ij}\psi_k\psi_l.
\end{aligned}
$$

From equations (I.10) and (I.11) we thus infer that the bosonization steps (5.40) and (5.42) are justified as long as T_{ijkl} is the Levi-Civita tensor, that is, $\varepsilon_{ijkl}\psi_i\psi_j\psi_k\psi_l$ can indeed be written as a bi-linear form.

Appendix J

Algebraic and numerical techniques

In this section we introduce some techniques that we employed to perform algebraic and numerical calculations.

J.1 Radial grids for the quark-gluon vertex

Throughout the computation of the quark-gluon vertex we employ two different grids for the radial[1] components of the momenta. This procedure has been suggested by Richard Williams. Taking points on the external grid slightly different from internal points excludes nodes that might become numerically troublesome. This procedure still places points very close to the external nodes. First, the external grid is constructed. It spans the distance from the IR-cut-off to the UV-cut-off and features nodes which are distributed according to the prescription

$$x_i \;=\; x_{ir}\left(\frac{x_{uv}}{x_{ir}}\right)^{\frac{i-q}{n-q}}\;,\; i\in[1,n], \tag{J.1}$$

where x_{ir} and x_{uv} are the IR and UV cut-off respectively, and n is the number of external nodes. On a $\log_{10}$ scale, the nodes obtained by this prescription appear equidistant. For our calculation we considered $x_{ir} = 10^{-4}$ GeV^2, $x_{uv} = 5\times 10^4$ GeV^2 and $n = 32$. The external grid is employed for the left hand side of equations (3.4) and (3.5), that is, the propagator and vertex dressings are evaluated at these nodes for all their radial variables. For

[1] Radial with respect to hyper-spherical coordinates, see (A.7).

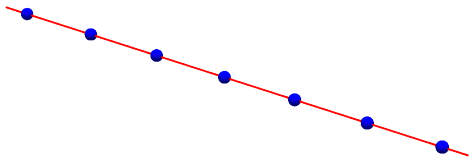

Figure J.1: A sketch of the external momentum grid as obtained from equation (J.1).

the propagator there is only p^2, while in case of the vertex the grid is used for p^2 and q^2. Internally, for the loop integrals in the quark self-energy and in the non-abelian diagram, we use a different grid. The internal grid is obtained from the external grid as follows. For all neighboring nodes on the external grid, compute n_s abscissas and weights according to the Gauss-Legendre quadrature rule [90], using the neighboring external nodes as boundaries for the Gauss-Legendre rule. The external grid has n nodes, thus there are $n-1$ such intervals. Starting in the IR and working towards the UV one can then store the nodes and weights obtained through that procedure to arrays of dimensionality $n_s\,(n-1)$, which hold the full internal grid-points and their weights after this step. The external nodes are then automatically removed from the internal grid, as they serve as end-points for the Gauss-Legendre quadrature rule and are as such not roots of the Gauss-Legendre polynomials that are used to construct the abscissas. In Figures J.1, J.2 and J.3 we show the procedure graphically.

J.2 Treating systems with broken Lorentz invariance using FORM

In the following we briefly summarize how to treat systems with broken Lorentz invariance using the computer algebra system FORM [89]. In such systems, usually one encounters scalar products of different dimensionality, which requires slight modifications of FORM code written for the Lorentz symmetric case.

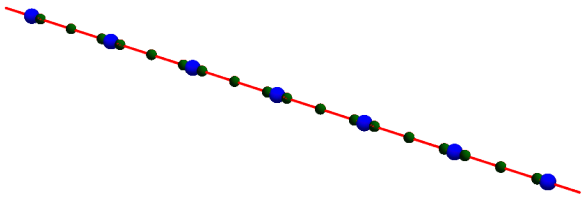

Figure J.2: The internal grid points are distributed between the external nodes according to the Gauss-Legendre quadrature rule, applied for $n_s = 3$ points for every interval with neighboring external grid points.

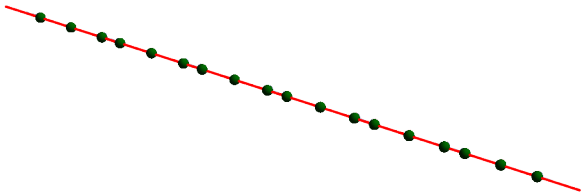

Figure J.3: The actual internal grid consists of $n_s\,(n-1)$ nodes resulting from the Gauss-Legendre quadrature rule. The external nodes are not part of this grid.

When evaluating the tensor algebra of systems at non-vanishing temperature and/or density with computer algebra systems (CAS), the broken Lorentz invariance requires that the CAS is capable of treating the different types of scalar products arising from three and four-dimensional contractions. The computer algebra system FORM [89] has been specifically developed to perform algebraic manipulations arising in the evaluation of Feynman diagrams very efficiently, but it assumes Lorentz symmetry to be maintained, at least as far as any straight-forward application of the routines provided by FORM is concerned. FORM is however a quite powerful tool, so it is quite easy to exploit the native features of FORM to make it suitable for non Lorentz invariant systems.

In FORM one can define the space-time dimension using the `Dimension` statement in the preamble of the FORM code, for example

```
1 On Statistics;
2 Dimension 3;
3 Symbol x,y,z;
4 ...
```

Listing J.1: Defining the dimension.

The `Dimension` declaration statement determines the dimension of all indices that have been defined *without giving an explicit number for their dimension*. As FORM uses Einstein's sum convention, the number given here directly affects the results of contractions of various quantities. Our goal is to treat three and four dimensional quantities in one FORM code at the same time. This is very convenient when performing computations at non-vanishing temperature and/or density, as can be seen when e.g. looking at the photon polarization tensor at non-vanishing temperature [175],

$$\Pi_{\mu\nu} = F\ P^L_{\mu\nu} + G\ P^T_{\mu\nu}, \tag{J.2}$$

$$P^T_{44} = P^T_{4i} = 0, \qquad P^T_{ij} = \delta_{ij} - \frac{q_i q_j}{\vec{q}^2}, \tag{J.3}$$

$$P^L_{\mu\nu} = \delta_{\mu\nu} - \frac{q_\mu q_\nu}{q^2} - P^T_{\mu\nu}, \tag{J.4}$$

where F and G are some dressing functions. Note that Latin indices run from 1 to 3, Greek indices from 1 to 4, which makes it clear that once this propagator is connected to other ingredients of some Feynman diagram, mixed scalar products of different dimensionality will occur after the contractions of all indices have been performed. One can achieve this with FORM quite easily.

FORM comes with the feature that, despite the overall dimension determined by the `Dimension` statement, one can define indices of different dimensionality. In particular one can assign a dimensionality of 0 to a particular set of indices, which suppresses the sum convention. The actual dimensionality of these indices is inherited from the `Dimension` statement.

```
1 On Statistics;
2 Dimension 3;
3 Indices i=0,j=0,k=0,l=0;
4 Indices mu=4,nu=4,rho=4,sigma=4;
```

Listing J.2: Indices of different dimensions. If the value 0 is assigned to an index, Einstein's sum convention is *not* implied for that particular index.

In Listing J.2 we have defined a dimension of 3, which means that all sum convention based contractions involving indices with no dimension assignment are performed with respect to three dimensions. Furthermore we declared Greek indices to be four-dimensional, while the 0 going with Latin indices prevents the sum convention from being executed for these indices. In principle one could also put the value for the Latin indices to 3 at this point,

which would result in the correct expressions coming from e.g. δ_{ii}, which would simply yield 3. However, this would spoil the possibility of identifying three and four dimensional scalar products as distinct quantities, as both expressions `p(i)·k(i)` and `p(mu)·k(mu)` would yield p.k. Thus we perform the computation in two sequential steps. In Listing J.3 we show examples of several scalar products and Kronecker-delta contractions.

```
1  On Statistics;
2  Dimension 3;                    * contratctions wrt dim=3 (
       despite the fact
3  *                               * that we want to perform 4-
       dim Euclidean
4  ********************            * computations we put the
       internal dim to 3)
5  *** DEFINITIONS  ***
6  ********************
7  Symbol k3,k4,p3,p4,pk3,pk4;     * 3 and 4 dim scalar products
8  Vector p,k;                     * two momenta
9  Indices mu=4, nu=4;             * greek indices run over 4
       dim
10 Indices i=0, j=0;               * latin indices are not
       summed over
11 ********************
12 *** TEST  CASES  ***
13 ********************
14 Local test1 = d_(i,i);            * should give 3
15 Local test2 = d_(mu,mu);          * should give 4
16 Local test3 = p.k;                * should give pk4
17 Local test4 = p(i)*k(i);          * should give pk3
18 Local test5 = p(mu)*k(mu);        * should give pk4
19 ********************
20 * STEP ONE :       *
21 * contract 4-dim   *
22 * indices first    *
23 * and identify     *
24 * the resulting 4d *
25 * quantities.     *
26 ********************
27 repeat;
28 id p.p = p4^2;
29 id p.k = pk4;
30 id k.k = k4^2;
31 endrepeat;
32 ********************
33 * STEP TWO :       *
34 * Sum over the     *
35 * 3-dim indices    *
36 * and identify the *
```

```
37 * remaining        *
38 * quantities as    *
39 * three dimensional*
40 ********************
41 sum i,j;
42 repeat;
43 id p.p = p3^2;
44 id p.k = pk3;
45 id k.k = k3^2;
46 endrepeat;
47 ********************
48 ***PRINT RESULTS ***
49 ********************
50 Print +s test1;
51 Print +s test2;
52 Print +s test3;
53 Print +s test4;
54 Print +s test5;
55 .end
```

Listing J.3: FORM code giving some examples of 3 and 4-dimensional contractions.

In the first step of the computation we perform all 4-dimensional contractions. The index dimension of 4 of the Greek indices ensures that expressions like the Kronecker delta yield the correct number of Euclidean space time. All Latin indices remain untouched at this point, and we can use the `repeat` and `id` statements to assign the final 4-dim expressions to the intermediate results. The following `sum i,j;` command performs the remaining contractions, which are performed with respect to 3 dimensions, as this is the standard dimension defined above. We successfully applied this procedure to derive the gluon DSE at non-vanishing chemical potential (a project that is not part of this thesis), where we confirmed the result by cross-checking with an independent (much slower) Mathematica computation. However, one should always be careful and check the correct behavior of the code by evaluating test-cases suitable for the particular problem.

J.3 Bi-cubic spline interpolation in the complex plane

Interpolation of two-dimensional complex data is a crucial aspect of the analytic structure calculations, as the integration contours are deformed to arbitrary shapes in the complex plane. The data however is discrete and

only accessible via tabulated functions. As the result in the end should be a smooth function (apart from non-analyticities, in that regions we will apply bi-linear interpolation), we use a complex bi-cubic spline interpolation to obtain information at arbitrary points in the complex plane. If the function that is to be interpolated is known to be a smooth differentiable continuous function, cubic spline interpolation can be used to obtain function values at arbitrary points in good approximation, as long as the point lies within the boundaries of the region that is to be interpolated and the resolution of this area is sufficiently high to capture local variations of the function. The spline interpolation is performed in two steps.

Consider a complex tabulated function $f(X)$ whose values are known on a $N_{real} \times N_{imag}$ rectangular grid (parallel to the axes), where N_{real} and N_{imag} denotes the extent of the grid in real and imaginary direction and $X \in \mathscr{M}(N_{real} \times N_{imag}, \mathbb{C})$ is a complex matrix holding the values of the independent variable (boundaries $x_{r,l} = \min \Re X$, $x_{r,u} = \max \Re X$, $x_{i,l} = \min \Im X$, $x_{i,u} = \max \Im X$) respectively. Our goal is to interpolate the function $f(x_0)$ at some value $x_0 \in \mathbb{C}$, where $x_{r,l} < \Re x_0 < x_{r,u}$ and $x_{i,l} < \Im x_0 < x_{i,u}$. We will use the routines `spline` and `splint` of [176]. Note that the values of X have to be strictly increasing in real and imaginary direction in order to apply these interpolation routines.

- **STEP I:** For every $y_i \in \Im X$, spline along the corresponding real values of X for this given imaginary number y_i and interpolate the real part of the function $f(x)$ at the real part of the interpolation value $\Re x_0$, which gives a one dimensional grid $I_{\mathfrak{R}}(y_i)$ of length N_{imag}, as there are N_{imag} different imaginary numbers y_i in the rectangular grid. Spline once more along the real values of X belonging to any given imaginary number y_i and interpolate the imaginary part of the function $f(x)$ at the point $\Re x_0$ again, storing the results to $I_{\mathfrak{C}}(y_i)$. After performing this step we have two one-dimensional grids $I_{\mathfrak{R}}$ and $I_{\mathfrak{C}}$ of length N_{imag} that hold the real part-interpolated real and imaginary part of the function for all discrete imaginary values. See Figures J.4 and J.5 for this step, where only one situation (real or imaginary part) is shown.

- **STEP 2:** To obtain the real part of the function at the interpolation value, $\Re f(x_0)$, we have to spline the previously obtained set $I_{\mathfrak{R}}$ and interpolate at the imaginary part of $\Im x_0$. To obtain the imaginary part of the function at the interpolation value, $\Im f(x_0)$, we have to spline the previously obtained set $I_{\mathfrak{C}}$ and interpolate at the imaginary part of $\Im x_0$. This step is depicted in Figure J.6.

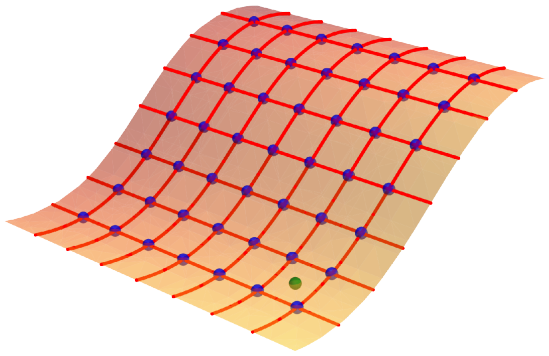

Figure J.4: Bi-cubic spline interpolation. The (smooth) function is known on a discrete lattice, the point to be interpolated is depicted by the green dot.

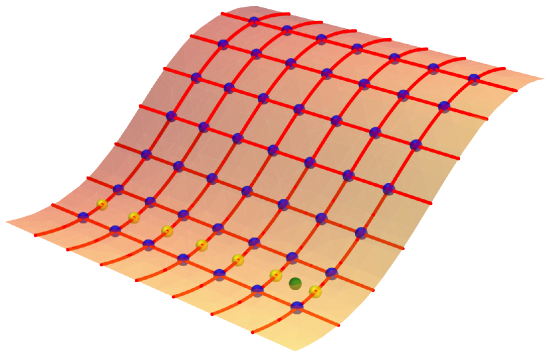

Figure J.5: In STEP 1 one has to spline interpolate at all discrete imaginary numbers along the real direction and store the result to an array (yellow dots).

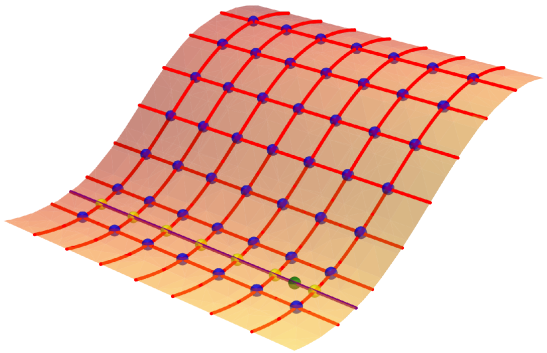

Figure J.6: In the second step, the array obtained in the previous step has to be spline interpolated at the value of the imaginary part.

To test the routine we set up a complex tabulated function on a regular 12×12 grid, $\Re x \in [-5, 5]$, $\Im x \in [-5, 5]$. The function is constructed in such a way that it features a Gaussian centered around $\Re x = 1$ in the real part, and a Gaussian centered around $\Re x = -1$ in the imaginary part. The function is then interpolated using the routine described above, where a regular 128×128 grid, $\Re x \in [-5, 5]$, $\Im x \in [-5, 5]$, is used. While the tabulated function is only known on 144 discrete points, after interpolation we have an approximation of the function on 16384 points. As the Gaussians are very smooth functions, the interpolated values give nice results. The results of this test-run are summarized in Figures J.7 to J.10.

For this particular run we mapped the complex plane to the matrix X in such a way that the imaginary part of the values stored in X decrease with increasing index of the matrix. As the interpolation routine requires strictly increasing behavior, the corresponding arrays have to be reversed before they are passed to the routine.

In our study of the complex quark propagator this routine is also a good tool for calculating a grid needed for generating plots, because the internal grid features a high density of nodes close to the axes and the origin. The grid points have been mapped logarithmically to resolve that region, which is a bad setting for 3d plotting routines which try to interpolate the data in order to generate a smooth surface. Here we use the spline interpolation routine to go back to a equally-distanced grid which can then be used conveniently to plot the result.

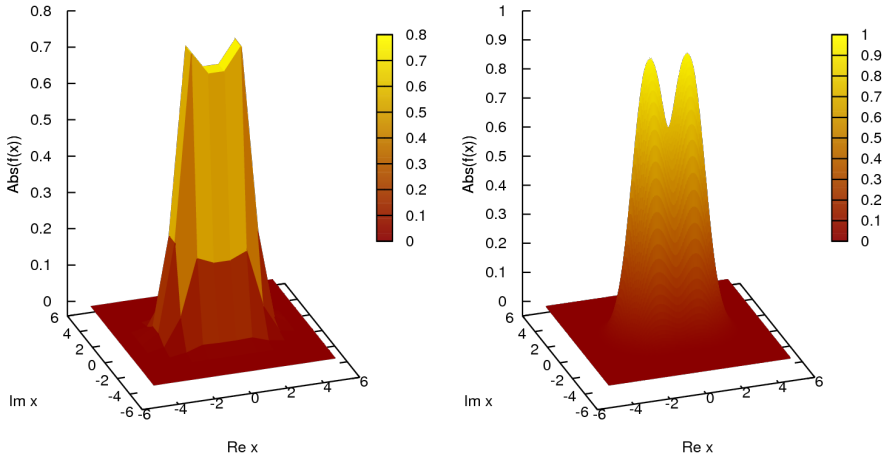

Figure J.7: Complex bi-cubic spline interpolation (see text). Left: Absolute value of the tabulated function. Right: Absolute value after complex bi-cubic spline interpolation.

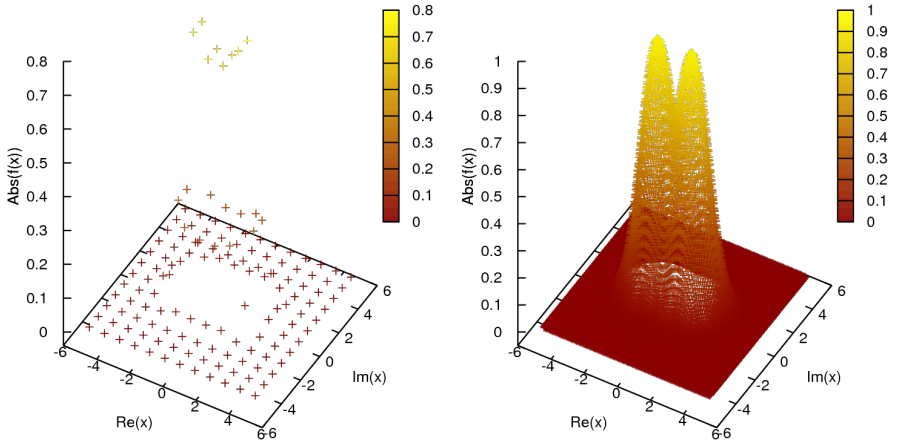

Figure J.8: Data points before (144) and after (16384) complex bi-cubic spline interpolation.

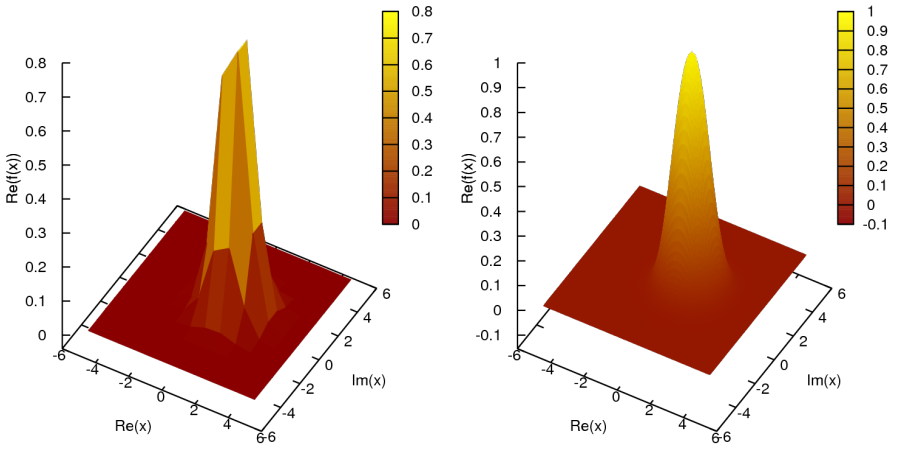

Figure J.9: Real part before and after interpolation.

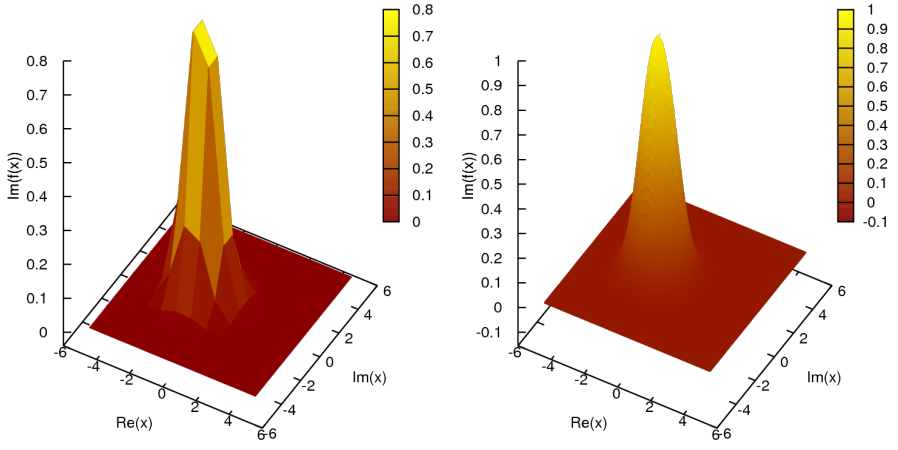

Figure J.10: Imaginary part before and after interpolation.

Appendix K

Supplementary material: Movies

These movies have been calculated using `Mathematica 8` by Wolfram Research [168]. The movies show the analytic structure in the radial integration plane of the correlator of the square of the Yang-Mills field strength tensor $\langle F^2(x)F^2(0)\rangle$ at the Born level after the angular integration (see [98],[174]). The 2-dimensional movies are dedicated to contour parametrizations for the case of i-particle propagators [100] that we used to develop the numerical procedure of massively parallel complex integration using GPUs [98]. The 3-dimensional movies show the analytic structure arising in the complex plane of the radial integration variable after the evaluation of the angular integral.

K.1 2d Movies

There are four 2-dimensional movies showing the obstructive structure in the complex plane of the radial integration variable y for the correlator (4.4).

K.1.1 The movie `2d_movie_1.mp4`

The left panel shows the branch cut (blue line) and the two poles (green dots) situated at $y = \pm\frac{i}{2}$ in the complex y-plane. The right panel shows the complex x-plane. As the movie progresses, the imaginary part of the x-variable is varied, as one can see on the right panel. The left panel shows how the branch cut changes shape, size and orientation in dependence on x. The three red points mark the positions where the branch cut hits the axis. They have been used as adaptive orientation points for a dynamically deformed contour. However, in the end it was not necessary to use these points, the simple contour deformations presented in Chapter 4 were sufficient to produce robust results.

K.1.2 The movie `2d_movie_2.mp4`

This movie shows the same setting as the first one, but now the real part of x is varied.

K.1.3 The movie `2d_movie_3.mp4`

This movie shows a dynamically deformed contour (red line) that connects the origin with the UV cut-off in the complex y-plane. The corresponding value of $x = p^2$ is shown explicitly. This contour deformation is not the one we used ultimately, but it also produces the right result. The contour is however more complicated to compute as it requires more dynamical adaptions than the ones presented in Chapter 4. The situation shown in this movie corresponds to region 4 in Figure 4.3.

K.1.4 The movie `2d_movie_4.mp4`

This movie shows a similar setting as the third movie, this time covering values of x corresponding to the regions 5, 1 and 2, see discussion in Chapter 4. The blue line blocking the contour in the last third of the movie is a numerical artifact.

K.2 3d Movies

There are three 3-dimensional movies regarding the analytic properties of $\langle F^2(x)F^2(0)\rangle$ at Born level, where Gribov-type propagators have been used as an input. The movies have been calculated by producing a 3d plot with Mathematica, changing the position of the camera by small steps. The plots show the analytic structure of the radial integration variable after the integration of the angular variable has been performed. Apart from a pair of complex conjugate poles (visualized as purple pillars in the movies) there are also two intersecting branch cuts showing up. The size, shape, orientation and position of the branch cuts has been calculated for all given parameters. However, for the purpose of visualization we furnished them with a brick-wall texture to indicate that they are obstacles for the radial integration contour connecting the origin with the UV cut-off. Several relevant parameters are shown in the movie to allow for orientation in the complex plane. This 'head up display' is depicted and explained in Figure K.1.

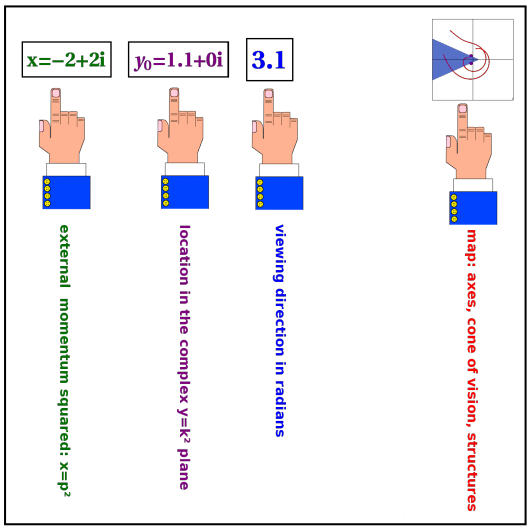

Figure K.1: The 'head up display' used in the 3d movies for orientation in the complex plane.

K.2.1 The movie `3d_movie_1.avi`

This movie shows a 360° panorama at the point $y_0 = 1$ GeV^2 for an external momentum square of $p^2 = x = -2 + 2i$ GeV^2. A compressed version of this movie (mp4) can be found in the folder '`3d-movies-compressed`'.

K.2.2 The movie `3d_movie_2.avi`

This movie shows a possible path of a radial integration contour connecting the origin with the UV cutoff. The camera moves along the contour by passing the pole in the second quadrant on the right side in order to avoid a modification through its residue. The camera moves out far enough such that the obstructive structure is left behind and heads straight for the UV cutoff, which is called ξ^2 in this case. The external momentum square is again given by $p^2 = x = -2 + 2i$ GeV^2.

K.2.3 The movie `3d_movie_3.avi`

In this movie we show how non-analyticities arise in the result of the overall expression. The camera moves up and hovers above the plane while looking down on it. Then we vary the external momentum square and identify three points where the endpoints of the cuts coincide with one or both poles, compromising the existence of unaffected contours. These points are the branch

points of the result.

Bibliography

[1] G. Aad *et al.* (ATLAS Collaboration), Phys.Lett. **B716**, 1 (2012), arXiv:1207.7214 [hep-ex].

[2] W. J. Marciano and H. Pagels, Phys. Rept. **36**, 137 (1978).

[3] K. G. Wilson, Phys.Rev. **D10**, 2445 (1974).

[4] C. Gattringer and C. B. Lang, *Quantum chromodynamics on the lattice*, Vol. 788 (2010) pp. 1–343.

[5] F. J. Dyson, Phys. Rev. **75**, 1736 (1949).

[6] J. S. Schwinger, Proc. Nat. Acad. Sci. **37**, 452 (1951).

[7] E. Salpeter and H. Bethe, Phys.Rev. **84**, 1232 (1951).

[8] L. Faddeev, Sov.Phys.JETP **12**, 1014 (1961).

[9] J. G. Taylor, Phys.Rev. **150**, 1321 (1966).

[10] U. Loring, K. Kretzschmar, B. C. Metsch, and H. R. Petry, Eur.Phys.J. **A10**, 309 (2001), arXiv:hep-ph/0103287 [hep-ph].

[11] R. Alkofer, C. S. Fischer, F. J. Llanes-Estrada, and K. Schwenzer, Annals Phys. **324**, 106 (2009), arXiv:0804.3042 [hep-ph].

[12] S. Mandelstam, Phys.Rept. **67**, 109 (1980).

[13] Y. Nambu and G. Jona-Lasinio, Phys.Rev. **122**, 345 (1961).

[14] H. Hamber and G. Parisi, Phys.Rev.Lett. **47**, 1792 (1981).

[15] K. Higashijima, Phys.Rev. **D29**, 1228 (1984).

[16] T. Nash, T. Yamanouchi, D. Nease, and J. Sculli, Phys.Rev.Lett. **32**, 858 (1974).

[17] D. Antreasyan, G. Cocconi, J. Cronin, H. J. Frisch, K. A. Olive, *et al.*, Phys.Rev.Lett. **39**, 513 (1977).

[18] M. Stevenson, Phys.Rev. **D20**, 82 (1979).

[19] F. Bergsma *et al.* (CHARM), Z.Phys. **C24**, 217 (1984).

[20] C. Hidalgo-Duque and F. J. Llanes-Estrada(2011), arXiv:1106.2462 [hep-ph].

[21] J. M. Lattimer and M. Prakash, Phys.Rept. **442**, 109 (2007), arXiv:astro-ph/0612440 [astro-ph].

[22] A. Schmitt, Lect.Notes Phys. **811**, 1 (2010), arXiv:1001.3294 [astro-ph.SR].

[23] C. S. Fischer, *Nonperturbative propagators, running coupling and dynamical mass generation in ghost - anti-ghost symmetric gauges in QCD*, Ph.D. thesis (2003), arXiv:hep-ph/0304233 [hep-ph].

[24] M. Hopfer, private communications.

[25] M. Q. Huber and L. von Smekal, JHEP **1304**, 149 (2013), arXiv:1211.6092 [hep-th].

[26] R. Williams(2014), arXiv:1404.2545 [hep-ph].

[27] C. S. Fischer, D. Nickel, and R. Williams, Eur.Phys.J. **C60**, 47 (2009), arXiv:0807.3486 [hep-ph].

[28] L. D. Faddeev and V. N. Popov, Phys. Lett. **B25**, 29 (1967).

[29] V. N. Gribov, Nucl. Phys. **B139**, 1 (1978).

[30] P. van Baal(1997), arXiv:hep-th/9711070 [hep-th].

[31] A. Maas, Phys.Rept. **524**, 203 (2013), arXiv:1106.3942 [hep-ph].

[32] N. Vandersickel and D. Zwanziger, Phys.Rept. **520**, 175 (2012), arXiv:1202.1491 [hep-th].

[33] J. C. Collins, *Renormalization. An introduction to renormalization, the renormalization group, and the operator product expansion* (1984).

[34] E. Panzer(2014), arXiv:1407.4943 [hep-th].

[35] C. Becchi, A. Rouet, and R. Stora, Annals Phys. **98**, 287 (1976).

[36] I. V. Tyutin, LEBEDEV-75-39(1975), arXiv:0812.0580 [hep-th].

[37] L. Baulieu and J. Thierry-Mieg, Nucl. Phys. **B197**, 477 (1982).

[38] J. C. Taylor, Nucl. Phys. **B33**, 436 (1971).

[39] A. Slavnov, Theor.Math.Phys. **10**, 99 (1972).

[40] N. Bogoliubov and O. Parasiuk, Acta Math. **97**, 227 (1957).

[41] K. Hepp, Commun.Math.Phys. **2**, 301 (1966).

[42] W. Zimmermann, Commun.Math.Phys. **15**, 208 (1969).

[43] J. Greensite, Prog. Part. Nucl. Phys. **51**, 1 (2003), arXiv:hep-lat/0301023 [hep-lat].

[44] R. Alkofer and J. Greensite, J. Phys. **G34**, S3 (2007), arXiv:hep-ph/0610365 [hep-ph].

[45] A. Wightman, Colloq. Int. CNRS **75**, 1 (1959).

[46] K. Osterwalder and R. Schrader, Commun. Math. Phys. **31**, 83 (1973).

[47] K. Osterwalder and R. Schrader, Commun. Math. Phys. **42**, 281 (1975).

[48] G. Kallen, Helv.Phys.Acta **25**, 417 (1952).

[49] H. Lehmann, Nuovo Cim. **11**, 342 (1954).

[50] K. Langfeld, H. Reinhardt, and J. Gattnar, Nucl.Phys. **B621**, 131 (2002), arXiv:hep-ph/0107141 [hep-ph].

[51] P. O. Bowman *et al.*, Phys. Rev. **D76**, 094505 (2007), arXiv:hep-lat/0703022 [hep-lat].

[52] R. Alkofer, W. Detmold, C. Fischer, and P. Maris, Phys.Rev. **D70**, 014014 (2004), arXiv:hep-ph/0309077 [hep-ph].

[53] C. S. Fischer, A. Maas, and J. M. Pawlowski, Annals Phys. **324**, 2408 (2009), arXiv:0810.1987 [hep-ph].

[54] S. Strauss, C. S. Fischer, and C. Kellermann(2012), arXiv:1208.6239 [hep-ph].

[55] J. S. Schwinger, Proc. Nat. Acad. Sci. **37**, 455 (1951).

[56] C. D. Roberts and A. G. Williams, Prog. Part. Nucl. Phys. **33**, 477 (1994), hep-ph/9403224.

[57] R. Alkofer and L. von Smekal, Phys. Rept. **353**, 281 (2001), arXiv:hep-ph/0007355 [hep-ph].

[58] C. S. Fischer, J. Phys. **G32**, R253 (2006), arXiv:hep-ph/0605173 [hep-ph].

[59] A. Bashir, L. Chang, I. C. Cloet, B. El-Bennich, Y.-X. Liu, *et al.*, Commun.Theor.Phys. **58**, 79 (2012), arXiv:1201.3366 [nucl-th].

[60] R. J. Rivers, *Path Integrals Methods in Quantum Field Theory* (Cambridge University Press, Cambridge, 1988).

[61] C. Itzykson and J.-B. Zuber, *Quantum Field Theory* (Dover Publications, Mineola, New York, 1980).

[62] R. Alkofer, M. Q. Huber, and K. Schwenzer, Comput. Phys. Commun. **180**, 965 (2009), arXiv:0808.2939 [hep-th].

[63] M. Q. Huber and J. Braun(2011), arXiv:1102.5307 [hep-th].

[64] M. Q. Huber and M. Mitter, Comput.Phys.Commun. **183**, 2441 (2012), arXiv:1112.5622 [hep-th].

[65] J. Berges, Phys. Rev. **D70**, 105010 (2004), arXiv:hep-ph/0401172 [hep-ph].

[66] C. Wetterich, Phys. Lett. **B301**, 90 (1993).

[67] J. Berges, N. Tetradis, and C. Wetterich, Phys. Rept. **363**, 223 (2002), arXiv:hep-ph/0005122 [hep-ph].

[68] H. Gies(2006), presented at ECT* School on Renormalization Group and Effective Field Theory Approaches to Many-Body Systems, Trento, Italy, 27 Feb - 10 Mar 2006, arXiv:hep-ph/0611146 [hep-ph].

[69] D. F. Litim, Phys. Lett. **B486**, 92 (2000), arXiv:hep-th/0005245 [hep-th].

[70] D. F. Litim, Phys. Rev. **D64**, 105007 (2001), arXiv:hep-th/0103195 [hep-th].

[71] R. L. Stratonovich, Soviet Physics Doklady **2**, 416 (Jul. 1957).

[72] J. Hubbard, Phys.Rev.Lett. **3**, 77 (1959).

[73] J. Skullerud and A. Kizilersu, JHEP **09**, 013 (2002), arXiv:hep-ph/0205318 [hep-ph].

[74] J. I. Skullerud, P. O. Bowman, A. Kizilersu, D. B. Leinweber, and A. G. Williams, JHEP **04**, 047 (2003), arXiv:hep-ph/0303176 [hep-ph].

[75] E. Rojas, J. de Melo, B. El-Bennich, O. Oliveira, and T. Frederico, JHEP **1310**, 193 (2013), arXiv:1306.3022 [hep-ph].

[76] A. Aguilar, D. Binosi, D. Ibañez, and J. Papavassiliou(2014), arXiv:1405.3506 [hep-ph].

[77] M. Hopfer, C. S. Fischer, and R. Alkofer(2014), arXiv:1405.7031 [hep-ph].

[78] M. Hopfer, C. S. Fischer, and R. Alkofer, Acta Phys.Polon.Supp. **7**, 613 (2014), arXiv:1405.7340 [hep-ph].

[79] A. Windisch, M. Hopfer, and R. Alkofer, Acta Phys.Polon.Supp. **6**, 347 (2013), arXiv:1210.8428 [hep-ph].

[80] M. Hopfer, A. Windisch, and R. Alkofer, PoS **ConfinementX**, 073 (2012), arXiv:1301.3672 [hep-ph].

[81] M. Hopfer, PhD thesis, in preparation (2014).

[82] A. Blum, M. Q. Huber, M. Mitter, and L. von Smekal, Phys.Rev. **D89**, 061703 (2014), arXiv:1401.0713 [hep-ph].

[83] G. Eichmann, R. Williams, R. Alkofer, and M. Vujinovic, Phys.Rev. **D89**, 105014 (2014), arXiv:1402.1365 [hep-ph].

[84] M. Q. Huber, A. L. Blum, M. Mitter, and L. von Smekal, PoS **QCD-TNT-III**, 018 (2013), arXiv:1401.5241 [hep-ph].

[85] M. Vujinovic, R. Alkofer, G. Eichmann, and R. Williams, Acta Phys.Polon.Supp. **7**, 607 (2014), arXiv:1404.4474 [hep-ph].

[86] R. Alkofer, G. Eichmann, C. S. Fischer, M. Hopfer, M. Vujinovic, *et al.*, PoS **QCD-TNT-III**, 003 (2013), arXiv:1405.7310 [hep-ph].

[87] M. Pelaez, M. Tissier, and N. Wschebor, Phys.Rev. **D88**, 125003 (2013), arXiv:1310.2594 [hep-th].

[88] G. Eichmann, Phys.Rev. **D84**, 014014 (2011), arXiv:1104.4505 [hep-ph].

[89] J. Vermaseren(2000), arXiv:math-ph/0010025 [math-ph].

[90] M. Abramowitz and I. A. Stegun, *Handbook of Mathematical Functions* (Dover, New York, 1965).

[91] S. Stainsby and R. Cahill, Int.J.Mod.Phys. **A7**, 7541 (1992).

[92] P. Maris, Phys.Rev. **D50**, 4189 (1994).

[93] A. Bender and R. Alkofer, Phys.Rev. **D53**, 446 (1996), arXiv:hep-ph/9411266 [hep-ph].

[94] C. Burden, Phys.Rev. **D57**, 276 (1998), arXiv:hep-ph/9702411 [hep-ph].

[95] S. Dorkin, L. Kaptari, T. Hilger, and B. Kampfer, Phys.Rev. **C89**, 034005 (2014), arXiv:1312.2721 [hep-ph].

[96] C. S. Fischer and R. Williams, Phys.Rev.Lett. **103**, 122001 (2009), arXiv:0905.2291 [hep-ph].

[97] V. Sauli(2013), arXiv:1312.2796 [hep-ph].

[98] A. Windisch, R. Alkofer, G. Haase, and M. Liebmann, Comput.Phys.Commun. **184**, 109 (2013), arXiv:1205.0752 [hep-ph].

[99] A. Windisch, M. Q. Huber, and R. Alkofer, Phys.Rev. **D87**, 065005 (2013), arXiv:1212.2175 [hep-ph].

[100] L. Baulieu, D. Dudal, M. Guimaraes, M. Huber, S. Sorella, *et al.*, Phys.Rev. **D82**, 025021 (2010), arXiv:0912.5153 [hep-th].

[101] A. Windisch, M. Q. Huber, and R. Alkofer, PoS **ConfinementX**, 060 (2012), arXiv:1301.3525 [hep-ph].

[102] V. Mathieu, N. Kochelev, and V. Vento, Int.J.Mod.Phys. **E18**, 1 (2009), arXiv:0810.4453 [hep-ph].

[103] D. Zwanziger, Phys.Rev. **D65**, 094039 (2002), arXiv:hep-th/0109224 [hep-th].

[104] M. Q. Huber, A. Maas, and L. von Smekal, JHEP **1211**, 035 (2012), arXiv:1207.0222 [hep-th].

[105] A. Maas, Phys. Rev. **D75**, 116004 (2007), arXiv:0704.0722 [hep-lat].

[106] A. Cucchieri and T. Mendes, Phys. Rev. Lett. **100**, 241601 (2008), arXiv:0712.3517 [hep-lat].

[107] R. Cutkosky, J.Math.Phys. **1**, 429 (1960).

[108] D. Dudal and M. S. Guimaraes, Phys.Rev. **D83**, 045013 (2011), arXiv:1012.1440 [hep-th].

[109] D. Dudal, J. A. Gracey, S. P. Sorella, N. Vandersickel, and H. Verschelde, Phys. Rev. **D78**, 065047 (2008), arXiv:0806.4348 [hep-th].

[110] P. Boucaud, J.-P. Leroy, A. L. Yaouanc, J. Micheli, O. Pene, and J. Rodriguez-Quintero, JHEP **0806**, 012 (2008), arXiv:0801.2721 [hep-ph].

[111] A. Aguilar, D. Binosi, and J. Papavassiliou, Phys.Rev. **D78**, 025010 (2008), arXiv:0802.1870 [hep-ph].

[112] R. Alkofer, M. Q. Huber, and K. Schwenzer, Phys. Rev. **D81**, 105010 (2010), arXiv:0801.2762 [hep-th].

[113] L. von Smekal, R. Alkofer, and A. Hauck, Phys. Rev. Lett. **79**, 3591 (1997), arXiv:hep-ph/9705242 [hep-ph].

[114] L. von Smekal, A. Hauck, and R. Alkofer, Ann. Phys. **267**, 1 (1998), arXiv:hep-ph/9707327 [hep-ph].

[115] D. Binosi and J. Papavassiliou, Phys. Rept. **479**, 1 (2009), arXiv:0909.2536 [hep-ph].

[116] P. Boucaud, J. Leroy, A. L. Yaouanc, J. Micheli, O. Pene, *et al.*, Few Body Syst. **53**, 387 (2012), arXiv:1109.1936 [hep-ph].

[117] C. Lerche and L. von Smekal, Phys. Rev. **D65**, 125006 (2002), arXiv:hep-ph/0202194 [hep-ph].

[118] V. Bornyakov, V. Mitrjushkin, and M. Müller-Preussker, Phys.Rev. **D81**, 054503 (2010), arXiv:0912.4475 [hep-lat].

[119] D. Dudal, O. Oliveira, and N. Vandersickel, Phys.Rev. **D81**, 074505 (2010), arXiv:1002.2374 [hep-lat].

[120] A. C. Aguilar and J. Papavassiliou, Eur.Phys.J. **A35**, 189 (2008), arXiv:0708.4320 [hep-ph].

[121] D. Dudal, S. Sorella, and N. Vandersickel, Phys.Rev. **D84**, 065039 (2011), arXiv:1105.3371 [hep-th].

[122] J. Gracey, Phys.Rev. **D82**, 085032 (2010), arXiv:1009.3889 [hep-th].

[123] A. Cucchieri, D. Dudal, T. Mendes, and N. Vandersickel, Phys.Rev. **D85**, 094513 (2012), arXiv:1111.2327 [hep-lat].

[124] D. Dudal, S. P. Sorella, N. Vandersickel, and H. Verschelde, JHEP **08**, 110 (2009), arXiv:0906.4257 [hep-th].

[125] M. Capri, D. Dudal, M. Guimaraes, L. Palhares, and S. Sorella, Int.J.Mod.Phys. **A28**, 1350034 (2013), arXiv:1208.5676 [hep-th].

[126] P. Maris and P. C. Tandy, Phys.Rev. **C60**, 055214 (1999), arXiv:nucl-th/9905056 [nucl-th].

[127] J. S. Ball and T.-W. Chiu, Phys. Rev. **D22**, 2542 (1980).

[128] T. P. Group, CUDA Fortran Programming Guide and Reference(2014), `http://www.pgroup.com`.

[129] U. Vogl and W. Weise, Prog.Part.Nucl.Phys. **27**, 195 (1991).

[130] S. Klevansky, Rev.Mod.Phys. **64**, 649 (1992).

[131] T. Hatsuda and T. Kunihiro, Phys.Rept. **247**, 221 (1994), arXiv:hep-ph/9401310 [hep-ph].

[132] M. Buballa, Phys.Rept. **407**, 205 (2005), arXiv:hep-ph/0402234 [hep-ph].

[133] C. S. Fischer, J. Luecker, and J. A. Mueller, Phys.Lett. **B702**, 438 (2011), arXiv:1104.1564 [hep-ph].

[134] C. S. Fischer and J. Luecker, Phys.Lett. **B718**, 1036 (2013), arXiv:1206.5191 [hep-ph].

[135] C. S. Fischer, J. Luecker, and C. A. Welzbacher(2014), arXiv:1405.4762 [hep-ph].

[136] D. Nickel, J. Wambach, and R. Alkofer, Phys. Rev. **D73**, 114028 (2006), arXiv:hep-ph/0603163 [hep-ph].

[137] D. Nickel, R. Alkofer, and J. Wambach, Phys. Rev. **D74**, 114015 (2006), arXiv:hep-ph/0609198 [hep-ph].

[138] D. Nickel, R. Alkofer, and J. Wambach, Phys. Rev. **D77**, 114010 (2008), arXiv:0802.3187 [hep-ph].

[139] H. Chen, M. Baldo, G. Burgio, and H.-J. Schulze, Phys.Rev. **D84**, 105023 (2011), arXiv:1107.2497 [nucl-th].

[140] H. Chen, M. Baldo, G. Burgio, and H.-J. Schulze, Phys.Rev. **D86**, 045006 (2012), arXiv:1203.0158 [nucl-th].

[141] D. Müller, M. Buballa, and J. Wambach, Eur.Phys.J. **A49**, 96 (2013), arXiv:1303.2693 [hep-ph].

[142] D. Bailin and A. Love, Phys.Rept. **107**, 325 (1984).

[143] K. Rajagopal and F. Wilczek(2000), arXiv:hep-ph/0011333 [hep-ph].

[144] M. Alford, eConf **C010815**, 137 (2002), arXiv:hep-ph/0110150 [hep-ph].

[145] D. H. Rischke, Prog. Part. Nucl. Phys. **52**, 197 (2004), arXiv:nucl-th/0305030 [nucl-th].

[146] M. G. Alford, A. Schmitt, K. Rajagopal, and T. Schäfer, Rev.Mod.Phys. **80**, 1455 (2008), arXiv:0709.4635 [hep-ph].

[147] M. Buballa, Prog.Part.Nucl.Phys. **61**, 66 (2008).

[148] W. V. Liu and F. Wilczek, Phys.Rev.Lett. **90**, 047002 (2003), arXiv:cond-mat/0208052 [cond-mat].

[149] M. G. Alford, J. A. Bowers, and K. Rajagopal, Phys.Rev. **D63**, 074016 (2001), arXiv:hep-ph/0008208 [hep-ph].

[150] J. Bardeen, L. Cooper, and J. Schrieffer, Phys.Rev. **108**, 1175 (1957).

[151] B. S. Chandrasekhar, Applied Physics Letters **1**, 7 (1962), `http://scitation.aip.org/content/aip/journal/apl/1/1/10.1063/1.1777362`.

[152] A. Clogston, Phys.Rev.Lett. **9**, 266 (1962).

[153] M. Buballa and S. Carignano(2014), arXiv:1406.1367 [hep-ph].

[154] A. larkin and Y. Ovchinnikov, Zh.Eksp.Teor.Fiz. **47**, 1136 (1964).

[155] P. Fulde and R. A. Ferrell, Phys.Rev. **135**, A550 (1964).

[156] R. Dodson, D. Lewis, and P. M. McCulloch(2001), arXiv:astro-ph/0111404 [astro-ph].

[157] J. Horvath, Int.J.Mod.Phys. **D13**, 1327 (2004), arXiv:astro-ph/0404324 [astro-ph].

[158] C. M. Espinoza, A. G. Lyne, B. W. Stappers, and M. Kramer, Mon.Not.Roy.Astron.Soc. **414**, 1679 (2011), arXiv:1102.1743 [astro-ph.HE].

[159] H. Muther and A. Sedrakian, Phys.Rev.Lett. **88**, 252503 (2002), arXiv:cond-mat/0202409 [cond-mat].

[160] H. Muther and A. Sedrakian, Phys.Rev. **C67**, 015802 (2003), arXiv:nucl-th/0209061 [nucl-th].

[161] H. Muther and A. Sedrakian, Phys.Rev. **D67**, 085024 (2003), arXiv:hep-ph/0212317 [hep-ph].

[162] A. Sedrakian, 209(2003), arXiv:nucl-th/0312053 [nucl-th].

[163] E. Gubankova, W. V. Liu, and F. Wilczek, Phys.Rev.Lett. **91**, 032001 (2003), arXiv:hep-ph/0304016 [hep-ph].

[164] J. Polchinski(1992), arXiv:hep-th/9210046 [hep-th].

[165] T. Schäfer and F. Wilczek, Phys.Lett. **B450**, 325 (1999), arXiv:hep-ph/9810509 [hep-ph].

[166] N. J. Evans, S. D. Hsu, and M. Schwetz, Nucl.Phys. **B551**, 275 (1999), arXiv:hep-ph/9808444 [hep-ph].

[167] P. Schuck, Y. Funaki, H. Horiuchi, G. Roepke, A. Tohsaki, *et al.*(2014), arXiv:1401.1713 [nucl-th].

[168] Wolfram Research Inc., Mathematica 8.0, Champaign, Illinois (2010).

[169] Doxygen `http://www.stack.nl/~dimitri/doxygen/index.html`.

[170] H. Takahasi and M. Mori **21**, 206 (Jun. 1973), ISSN 0029-599X (print), 0945-3245 (electronic).

[171] G. Eichmann and C. S. Fischer, Phys.Rev. **D87**, 036006 (2013), arXiv:1212.1761 [hep-ph].

[172] R. Karplus, C. M. Sommerfield, and E. H. Wichmann, Phys.Rev. **111**, 1187 (1958).

[173] L. Landau, Nucl.Phys. **13**, 181 (1959).

[174] A. Windisch, M. Q. Huber, and R. Alkofer, Acta Phys.Polon.Supp. **6**, 887 (2013), arXiv:1304.3642 [hep-ph].

[175] M. Le Bellac, *Thermal Field Theory*, Cambridge Monographs on Mathematical Physics (Cambridge University Press, 2000) ISBN 9780521654777, `http://books.google.at/books?id=00_x6GR8GXoC`.

[176] W. H. Press, S. A. Teukolsky, W. T. Vetterling, and B. P. Flannery, *Numerical Recipes in FORTRAN: The Art of Scientific Computing* (1992).